Investigating Brain Structure Using Voxel-Based Methods with Magnetic Resonance Imaging

Dissertation
zur Erlangung des akademischen Grades
Dr. rer. med.
an der Medizinischen Fakultät
der Universität Leipzig

eingereicht von:
Dipl. Inf. Daniel-Paolo Streitbürger

Geburtsdatum / Geburtsort:
17.05.1985 / Braunschweig / Deutschland

angefertigt am / in:
Max-Planck Institut für Kognitions- und Neurowissenschaften

Betreuer:
Prof. Dr. Dr. Matthias L. Schroeter
PD. Dr. Karsten Müller

Beschluss über die Verleihung des Doktorgrades vom: 21.01.2014

Table of Content

Bibliographische Beschreibung

Streitbürger, Daniel-Paolo

Investigating Brain Structure Using Voxel-Based Methods with Magnetic Resonance Imaging

Universität Leipzig, Dissertation

101 S.[1], 171 Lit.[2], 21 Abb., 9 Tab., 0 Anlagen

Referat:

This work addresses the sensitivity for the detection of structural brain changes of different voxel-based methods in combination with recent soft- and hardware improvements. It deals with possible confounds and caveats due to the increasing sensitivity of voxel-based studies. Therefore, two different voxel-based methods, voxel-based morphometry (VBM) and Tract-Based Spatial Statisics (TBSS), were compared in three different studies, in order to describe sensitivity and limits in the detection of structural brain changes. The first study describes the effect of dehydration on brain structure using VBM. Detection sensitivity showed approx. 6% difference of the ventricular volume, various effects in white matter and little impact on gray matter. Accordingly, the possible confound of dehydration as an additional bias in neurodegenerative imaging studies can not be fully neglected and should be carefully considered. Investigations of TBSS and white matter structure using white matter sensitive peripheral blood serum markers showed positive correlation of S100B and mainly the corpus callosum in healthy subjects. This might be interesting for neuropsychiatric studies and future investigations to open new perspectives in treatment of those disorders. The last study describes the interplay of increasing sensitivity and concomitant increasing false positive detection of age related brain changes. The

---

[1] Seitenanzahl insgesamt

[2] Zahl der im Literaturverzeichnis ausgewiesenen Literaturangaben

comparison of different scanning parameters revealed significant effects only related to the changing acquisition design. This work shows a beneficial effect of 32-channel coil acquisitions compared to 12-channel coil images. Furthermore, results show strong preference for whole brain analyses using images scanned with the Alzheimer's Disease Neuroimaging Initiative protocol compared to the newly presented MP2RAGE protocol.

The studies emphasize the high detection sensitivity for even subtle structural brain changes, using recent voxel-based methods and scanning hardware. Moreover, it underlines the suitability of VBM and TBSS for whole brain analysis and the need for careful selection of scanning parameters and analysis methods to achieve highest detection sensitivity and simultaneously low probability of false positive results.

1. General Introduction

The considerable increase of patients with neurodegenerative diseases over the past decade is a worldwide growing challenge. Particularly, the amount of people suffering from Alzheimer`s Disease (AD), the most common dementia syndrome, massively increased in the past centuries and will increase in the future. The Alzheimer`s Disease International (ADI) and World Health Organization (WHO) estimated that currently worldwide 36 million people suffer from dementia. Furthermore, 7.7 million new cases of dementia are predicted per year, possibly increasing up to 115 million until the year 2050. Moreover, the treatment costs in 2010 roughly amount to 604 Billion US Dollar (486 Billion Euro) worldwide for care (40%), informal care (45%) and direct medical treatment (15%). Consequently, high income countries will have an average annual societal cost of approx. 32.000 US Dollar (25.000 Euro) per dementia patient. (Alzheimer`s Disease International, 2011; World Health Organization, 2012).

Regarding Germany, 1.3 Million people suffer from dementia at present, which will increase up to 2 Million until 2030 and reach an estimated 2.6 Million in the year 2050. At the same time, the estimated German population will decrease from 81.8 Million to 77.4 Million in 2030 and 69.4 Million in 2050, mainly related to the low birth rates in Germany (Statistisches Bundesamt, 2012). The continuous population decline and the concomitant increase of life expectancy will end in a disease rate of 4 in 100 people suffering from AD in the year 2050. Consequently, the increased ratio between diseased and healthy individuals raises the financial burden for the population to provide adequate medical treatment and care also in Germany. The costs for treatment and care of demented patients in Germany added up to 9.4 Billion Euro for the year 2008 (Sütterlin et al., 2011) and is estimated to increase substantially in the coming centuries.

Although these estimations focused mainly on AD patients, a steady increase of neurodegenerative disorders worldwide can be expected for many other diseases, like e.g. Huntington`s Disease or Parkinson´s Disease. These disorders are age-related

(Butterfield et al., 2001; Butterfield and Kanski, 2001) and the estimated increase in newly diseased people is mainly related to the massive increase of life expectancy worldwide (Sütterlin et al., 2011; World Health Organization, 2012). Quite naturally, regarding the above written cost estimations for the next centuries, lowering of the treatment costs is one of the major goals for clinics, health insurances and governments. That is why neurodegenerative diseases and their financial impact for the population have found its way into many political agendas and research fields to find and define ways to control the uprising financial problem. The early detection of neurodegenerative diseases may play a key role in cost control, while simultaneously prolonging the patients` self-determined life-style (Alzheimer`s Disease International, 2011; Sütterlin et al., 2011). Early detection of newly diseased patients helps clinicians to start treatment in an early and non-severe disease stage, thereby adjusting medication as best as possible (Alzheimer`s Disease International, 2011). Moreover, investigations in early detection methods might help patients and their relatives to organize the patients future (Alzheimer`s Disease International, 2011; Sütterlin et al., 2011).

To achieve this goal it is important to develop, implement and evaluate methods for early detection of neuropsychiatric disorders to allow for the best possible treatment of these patients.

1.1. Detecting Structural Brain Changes in Neuropsychiatric Disorders Using Voxel-Based Methods

Neuropsychological tests are helpful tools to detect neuropsychiatric and neurodegenerative diseases in patients. One important drawback though, is the need for well trained personnel (Salmon and Bondi, 2009). Automatic detection methods on the other hand, can analyze patient data in a non-biased, reproducible and often less time consuming manner.

Some methods use imaging data to detect structural brain changes related to specific neuropsychiatric disorders. Many of these algorithms and analysis methods focus on structural magnetic resonance images (MRI), like T1-weighted or diffusion weighted images (diffusion tensor imaging (DTI)) (Ashburner and Friston, 2000; Fischl et al., 2002; Smith et al., 2006). MRI has several different beneficial properties, such as e.g. a high signal-to-noise ratio (SNR), a high spatial resolution and no need for radioactive tracers (Baudendistel et al., 2004; Bridge and Clare, 2006; Larsson and Stahlberg, 2005; Schmitt et al., 2004; Tanenbaum, 2006). Consequently, the analysis of structural MRI is very beneficial for detecting and evaluating neuropsychiatric disorders and other non-disease related morphological brain changes (Ashburner and Friston, 2000; Fischl et al., 2002; Smith et al., 2006).

One widely used approach to analyze patient data is the voxel-based statistics method, which has been implemented for different imaging modalities of MRI (Ashburner and Friston, 2000; Smith et al., 2006). For successful application, the acquired images have to be preprocessed. The data have to fulfill several requirements, to ensure that statistical analyses produce reliable results and potential false positives are reduced to a negligible size. In general, the preprocessing steps include registration of the images towards a standard space and segmentation of the images into the desired tissue compartments – gray matter (GM), white matter (WM) and cerebral spinal fluid (CSF) (Ashburner and Friston, 2000, 2005; Smith et al., 2006). Depending on the image modality, additional preprocessing steps need to be applied e.g. noise reduction, bias-field correction or estimation of partial volume effects (Ashburner and Friston, 2005). After successful preprocessing, statistical analyses can be performed using a General Linear Model (GLM) (Friston et al., 1994). The GLM can for example be used to identify statistical significant GM structure differences between patients and healthy controls or for the identification of regions which correlate with numerical input variables; e.g. psychological assessment results or biological parameters such as body mass index (BMI) or depression scales. In summary, this approach allows for identification of (disease related) structural brain changes, as well as neural plasticity.

1.2. Detecting Gray Matter Changes Using Voxel-Based Morphometry on T_1-weighted Images

The most popular voxel-wise method used for the analysis of whole brain T_1-weighted images, is Voxel-Based Morphometry (VBM). After it was published in 2000, it became one of the most established morphometric change detection methods of the past decade (Brenneis et al., 2003; Good et al., 2001b; Kinkingnehun et al., 2008; Pannacciulli et al., 2006; Tardif et al., 2010). At its simplest, VBM detects changes in the GM structure. In the context of VBM, this is often referred as GM density (GMD) (Ashburner and Friston, 2000). This methods has been successfully applied to a wide variety of topics, such as aging (Good et al., 2001b), AD (Frisoni et al., 2010b; Guo et al., 2010; Karas et al., 2003), Parkinson´s (Burton et al., 2004; Tessitore et al., 2012) and Huntington`s disease (Brenneis et al., 2003; Feldmann et al., 2008), as well as schizotypal disorders (Koo et al., 2006). Apart from age and disease related GMD changes, it is also possible to detect training-based plasticity changes with VBM induced by e.g. training juggling (Draganski et al., 2004), balancing (Taubert et al., 2010) or comparable skills (Abdul-Kareem et al., 2011; Draganski and May, 2008; Groussard et al., 2010). In neurodegenerative disease studies, for example, AD patients revealed widespread and massive deficits in GMD compared to healthy subjects in frontal-, tempoparietal cortex and striatal regions (Frisoni et al., 2010b; Guo et al., 2010; Karas et al., 2003; Karas et al., 2004; Kinkingnehun et al., 2008). Interestingly, similar widespread effects have been reported for healthy aging subjects compared to young control subjects (Good et al., 2001b).

Contrary to those massive and widespread effects, rather subtle changes induced by plasticity can be detected as well. Draganski et al. (2004) investigated the effect of juggling on brain structure with untrained healthy, young subjects. They found significant specific, transient, bilateral changes of the GMD in the mid-temporal areas, regions mainly responsible for processing visual-motion tasks. Furthermore, Taubert et al. (2010) detected structural brain changes in healthy subjects after a six-week balancing practice.

On the one hand, an increase of detection sensitivity is generally needed for instance by improving preprocessing results and therefore, presumably, increasing the validity of the statistical analyses. This increase of accuracy might be achieved by use of better software (Klein et al., 2010) and/or hardware (Baudendistel et al., 2004; Larsson and Stahlberg, 2005; Schmitt et al., 2004). On the other hand, new confounding factors, which exceed detection limit, might start to interfere with the statistical results and lead to systematic false positive results. It is necessary to investigate possible confounding factors to clarify their impact on future studies and ensure that they can be either be avoided or neglected.

1.3. Detecting White Matter Tract Changes Using Tract-Based Spatial Statistics on Diffusion Tensor Images

The Tract-Based Spatial Statistics (TBSS) approach is another very popular voxel-wise analysis method, which is implemented and provided by the Oxford Centre for Functional MRI of the Brain (FMRIB) (Smith et al., 2006). This approach analyzes DTI data to find anatomical connections in the white matter of the brain and to localize changes in the white matter tracts. These changes might be related to degeneration, plasticity or other sources of alteration. An often investigated image parameter to detect changes in white matter structure using TBSS is the Fractional Anisotropy (FA). FA is derived from subjects' diffusion data and quantifies the directionality of local white matter tracts. This measure is sensitive to white matter related changes and has a high sensitivity for detecting small changes, e.g. due to de-myelination (Onu et al., 2012; Yeh et al., 2009), or larger changes like e.g. disruption of the tract integrity after a (mild-) traumatic brain injury (Bazarian et al., 2007).

Furthermore, TBSS has already been successfully used to detect correlations of structural WM tracts with e.g. biomarkers. For example, Mueller et al. (2011) investigated the impact of leptin levels, a protein mainly expressed in adipocytes , on WM structures in lean and obese participants. They found an association between changes in the corpus callosum and leptin, which might be related to myelin alterations in this region. The approach of correlating numerical values such as biomarkers with WM tracts, using TBSS as statistical analysis method, has been used in a wide variety of topics (Counsell et al., 2008; Johansen-Berg et al., 2007; Liu et al., 2012; Saini et al., 2012). Detecting links between biomarkers, in particular their blood serum levels, and WM structures might be beneficial for psychiatrists and neuroscientists. Investigations related to de-myelination processes such as major depression, schizophrenia or comparable neuropsychiatric disorders might reveal new perspectives for treatment of those patients.

2. Detecting Structural Brain Changes Induced by Dehydration Using Voxel-Based Morphometry

As already mentioned, due to the higher accuracy and sensitivity originating from soft- and hardware improvements, the coincidental acquisition of physiological noise requires more attention. One possible confounding factor in T1-weighted images is the hydration status of participants (Dickson et al., 2005; Duning et al., 2005; Kempton et al., 2011; Kempton et al., 2009). These studies focused on the cerebral spinal fluid and concomitant enlargement of the ventricular system, but did not show the impact of hydration and dehydration on gray and white matter structure. A possible impact of subjects' hydration status on the preprocessing and statistics cannot be neglected and thus should be investigated.

It might be possible, that MRI scans benefit from a variety of different improvements in hard- and software. For example a better registration and segmentation accuracy using newer algorithms might improve detection accuracy and thus overemphasize the GM structure change due to subject's hydration state. Regarding the increasing amount of studies employing VBM, investigations in this topic are needed and will be discussed in the following section.

2.1. Introduction

A number of recent studies employing structural magnetic resonance imaging (MRI) have aimed to investigate gray matter (GM), white matter (WM), and the cerebrospinal fluid (CSF) system and its explanatory power for neurodegenerative disorders (Bendfeldt et al., 2009; Kinkingnehun et al., 2008; Nestor et al., 2008). Regarding

Alzheimer’s disease (AD), decreased GM and WM volumes were consistently found (Guo et al., 2010; Karas et al., 2004), which are assumed to be related to the loss of neurons and synapses. This, in turn, could also be a plausible explanation for an accompanied increase of CSF as several studies showed an enlarged size of the ventricles due to brain atrophy compared to healthy controls (Nestor et al., 2008; Schott et al., 2005; Schroeter et al., 2009b). Annual expansion of the ventricles in healthy elderly and AD patients is around 1.5-3.0% and 5-16%, respectively (Frisoni et al., 2010a). Such changes in brain tissue and fluids led to the idea of disease progression measures based on different approaches and tissue types (Bendfeldt et al., 2009). Nestor et al. (2008) proposed ventricular enlargement as a valid and sensitive short-term marker of disease progression in subjects with AD and mild cognitive impairment (MCI) for multi-center studies.

Besides investigations of CSF in dementia, several other studies showed CSF volume changes using VBM in non-neurodegenerative diseases. For example, Bendel et al. (2010) demonstrated a correlation of neuropsychological outcome after subarachnoid hemorrhages with an enlargement of CSF volume. They claimed that ventricular enlargement combined with GM loss may indicate general brain atrophy rather than hydrocephalus. Enlarged CSF and decreased GM volumes have also been found in women with schizotypal personality disorder (Koo et al., 2006). Furthermore, Hagemann et al. (2011) presented a strong correlation of progesterone and CSF volume change during the menstrual cycle. Consequently, they recommended considering such short-term hormone-dependent structural brain changes in VBM studies.

However, CSF can also be influenced intentionally by massive fluid intake (Duning et al., 2005) and nonintentionally by external factors, such as high ambient temperature or acute physical stress due to illness, infections, or fever (Schols et al., 2009). Recent studies have thus pointed to a potential confound in morphometric MRI studies due to a continuous and severe lack of hydration (Dickson et al., 2005; Duning et al., 2005; Kempton et al., 2011; Kempton et al., 2009). For example, dehydration might produce an additive effect in AD studies because increases of CSF volume, in particular in the ventricles, might be a result of long-term dehydration instead of degeneration of brain tissue. Considering intentional influence of fluid balance by water intake, Kempton et al. (2009) observed significant ventricular changes in acute dehydration with structural MRI. In particular, they found enlarged lateral ventricles but no changes in the fourth ventricle, although the whole ventricular system is predicted to be affected by variation in hydration status. Similarly, Duning et al. (2005) showed structural effects due to rehydration after dehydration, using a water intake of 1.5 l. This effect might be helpful to “normalize“ subjects’ fluid balance by changing from an often poorly controlled (and, hence, more variable) ‘normal hydration’ state to a more consistent ‘hyperhydration’ state.

Dickson et al. (2005), Duning et al. (2005), and Kempton et al. (2009) used the fully automatic method SIENA (Smith et al., 2002) as well as the manual segmentation tools MEASURE (Barta et al., 1997) and Analyze in their studies. SIENA is specifically designed to detect small morphological brain changes in longitudinal MRI studies. It gains its sensitivity by edge motion detection and maps changes onto surrounding edges. This approach is not accurate on spatial information and does not specify locations of detected volume changes. Another often-used method to detect subtle structural changes in cross-sectional studies is voxel-based morphometry (VBM) (Ashburner and Friston, 2000). It permits a longitudinal preprocessing approach that is not limited to edge detections and allows to assess structural changes for the entire brain.

In our present study, we investigate if dehydration effects can be measured in a longitudinal VBM study. Based on previous studies, we hypothesized that dehydration leads to an enlargement of the ventricular system. As currently detailed investigations of a potential influence on GM and WM are lacking, we additionally hypothesize a decrease of GM and/or WM volumes due to dehydration.

2.2. Methods

2.2.1. Subjects and Imaging Procedures

Six healthy young adults (3 female; mean 24.7±3.0 y, all right handed) participated in a long-term hydration experiment. All participants gave written consent after being informed about the possible risks and discomforts of the experimental procedure. Subjects also completed a health history questionnaire to assess their suitability for undergoing MRI scanning. Imaging was performed on a 3-T MAGNETOM Trio scanner (Siemens Medical Solutions, Erlangen, Germany) with a birdcage transmit/receive head coil. T_1-weighted images were acquired with a three-dimensional MP-RAGE sequence using the following parameters: inversion time 650 ms; repetition time, $TR = 1.3$ s; TR of the gradient-echo kernel 10 ms; echo time 3.93 ms, flip angle 10°, bandwidth 130 Hz/pixel, acquisition matrix 256×240, field of view 256×240 mm^2, slab thickness 192 mm (sagittal orientation), 128 partitions, 95% slice resolution, 2 averages. After zero filling, reconstructed images were obtained with a nominal voxel size of 1×1×1 mm^3.

2.2.2. Study Protocol

Subjects had to follow a strict hydrating/thirsting protocol, in particular, they were instructed not to participate in strenuous activity and to avoid alcohol consumption during the three days of the study. On subjects' arrival (between 8:00 and 9:00 in the morning), image data were acquired in a 'normal hydration' state. The time of this scan is subsequently referred to as $t = 0$. We note that there were no restrictions or specific requirements regarding fluid or food intake prior to this scan, which hence reflects the natural variability of water balance in subjects recruited for typical MRI studies.

Subject	V_w [ml]
1	3600
2	3950
3	3300
4	4100
5	3750
6	4200

Table 2.1: Subjects' water intake, V_w, between the scans performed at normal hydration (t = 0) and the hyperhydration (t = 10 h) on day 1.

Afterwards, all subjects were instructed to drink at least 3-4 l of water and were scanned again at $t \approx 10$ h (subsequently referred to as 'hyperhydration state'). A summary of individual water intake between the first two scans is given in Table 2.1. For comparison, the mean daily fluid intake in healthy male adults is approximately 2.1 l (Armstrong et al., 2010). For the next two days (i.e. days 2 and 3), subjects were allowed to drink 150 ml of water per day and had to avoid meals with a high fluid content. Gullans and Verbalis (1993) described a steady decline of the dehydration effect with time in a rat study. Therefore we decided to acquire three scans on day 3 to allow additional investigation of dynamic changes during dehydration. These three scans (subsequently referred to as 'dehydration scans') were acquired at times $t \approx 48$ h, 53 h, and 58 h after the 'normal hydration' scan (i.e. 38 h, 43 h, and 48 h after the 'hyperhydration' scan. Throughout the entire study, body weight, daily urine flow, and meal consumption (restricted to bread, rice, and potatoes on days 2 and 3) were monitored to ensure participants had adhered to the protocol. A summary of individual variations in urinary excretion and body weight is given in Table 2.2. On average, subjects lost approximately 2.3% of their body weight between the first and last scan. On day 3, they had an average urinary excretion of 908 ml as compared to an average value of approximately 1.3 l in healthy subjects under normal conditions (Armstrong et al., 2010).

2.2.3. Voxel-Based Morphometry

Images were processed using the longitudinal processing pipeline as offered in the VBM8 toolbox (Gaser, C., http://dbm.neuro.uni-jena.de/vbm/, last accessed 07.09.2011). Segmented GM, WM, and CSF images were smoothed with 8 mm^3 full width at half maximum and fed into a flexible factorial design with two factors (subject and hydration state). Assignments to the different levels of hydration state were: ‘0’ for normal hydration at t = 0, ‘–3’ for hyperhydration at t = 10 h, and ‘+1’ for dehydration at t = 48 h,

Subject	Day 1			Day 2			Day 3		
	_t_=0	_t_=5h	**_t_=10h**	_t_=24h	_t_=29h	_t_=34h	**_t_=48h**	**_t_=53h**	**_t_=58h**
				Urine excretion, ΔV_u [ml]					
1		1500	3500	800	0	100	300	0	150
2		1300	3000	0	230	400	700	190	370
3		1000	3250	700	130	300	330	180	280
4		1100	3100	0	0	300	900	0	250
5		1500	3000	550	100	250	550	100	150
6		1500	3500	0	0	300	850	150	0
				Body weight, M [kg]					
1	56.7	57.0	56.7	55.8	55.4	55.6	56.2	54.7	54.9
2	63.5	64.3	64.8	63.4	63.4	63.2	63.1	63.0	62.8
3	57.0	58.0	57.3	56.5	56.6	56.4	56.0	55.8	55.8
4	59.1	60.1	61.1	59.1	59.4	59.3	58.6	58.7	58.4
5	74.2	75.0	74.9	74.4	74.0	74.1	73.5	73.5	73.3
6	80.2	81.0	80.6	78.1	78.0	77.4	76.3	76.2	75.7

Table 2.2: Subjects’ cumulative urinary excretion between successive time points and body weight during the complete study.

53 h, and 58 h. Additionally, statistical computations with assignments ‘0’ for normal hydration, ‘–6’ for hyperhydration, and ‘+3, +2, and +1’ for the scans during dehydration at t = 48 h, 53 h, and 58 h, respectively, were calculated in order to investigate dynamic changes during dehydration. No potentially confounding variables were included. Smoothed GM, WM, and CSF images were thresholded excluding voxels containing a probability density below 10%. Finally, non-stationary cluster extent corrections (Hayasaka et al., 2004; Worsley et al., 1999) were applied to the VBM results.

2.2.4. SIENAr

The longitudinal voxel-wise statistical edge motion detection approach SIENAr implemented, published and provided by FSL, was applied to our data. Default parameters as described on the software website ((Smith et al., 2002), http://www.fmrib.ox.ac.uk, last accessed 08.01.2012) were chosen and comparisons of hyperhydration and the first dehydration state were statistically assessed using one-sample *t*-tests with the randomise software of FSL (Hayasaka and Nichols, 2003).

2.2.5. FreeSurfer

Both lateral ventricles as well as the third and fourth ventricle were segmented using the FreeSurfer image analysis suite (version. 4.5) (Fischl et al., 2002) with default parameters on a Debian 5.0 system. Summarized segmentation results were fed into a repeated measurements ANOVA using SPSS version 19.0 (IBM SPSS Inc., Chicago, IL, USA). Based on prior knowledge, one-tailed paired *t*-tests were computed comparing normal hydration, hyperhydration, and each of the dehydration datasets. Furthermore, cortical thickness data, a result of the FreeSurfer image processing pipeline, were

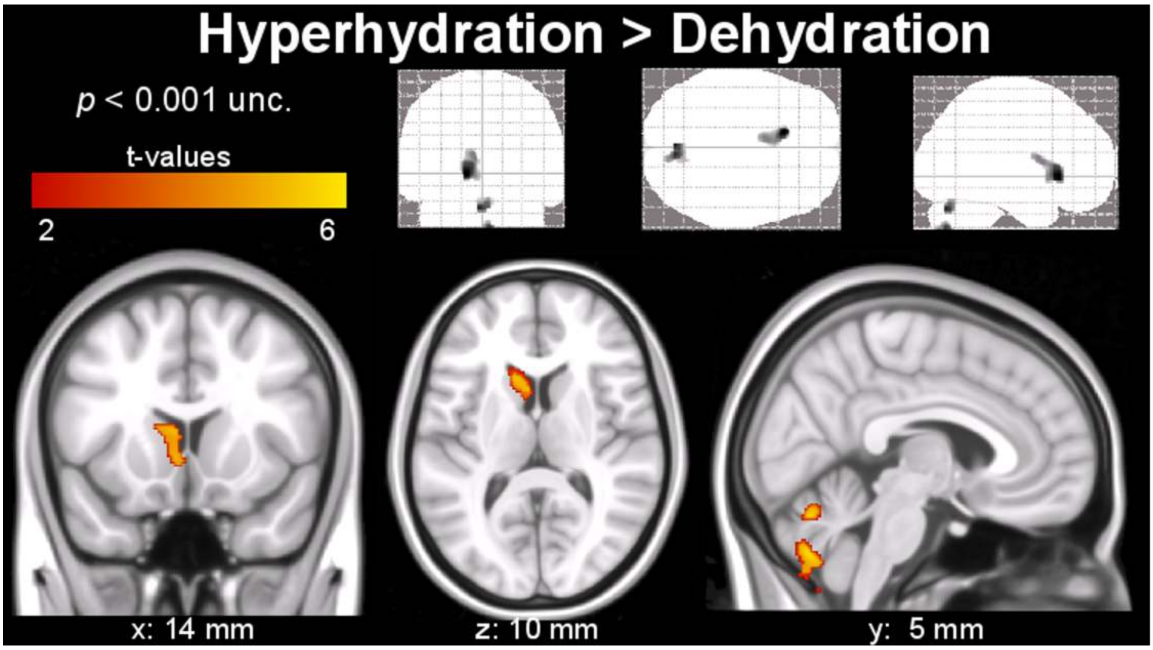

Figure 2.1: Segmented clusters of the gray matter with significant extension during hyperhydration compared to dehydration in caudate nucleus and cerebellar regions (indicated by the color code) obtained with VBM. The upper row shows the results as grayscale Maximum Intensity Projection onto the standard SPM glass brain in coronal, axial and sagittal view.

smoothed with a 20-mm Gaussian kernel and statistically assessed in a similar fashion as the VBM-processed data. In particular, a mixed-effects model using the SurfStat software (Worsley et al., 2009) was modeled assuming thinning in dehydration and thickening in hyperhydration.

2.3. Results

Gray matter analysis shows significant volume decrease due to dehydration in the left caudate nucleus and right-cerebellar posterior lobe, as presented in Figure 2.1. Figure 2.2 shows clusters with significant expansion of the WM during hyperhydration as

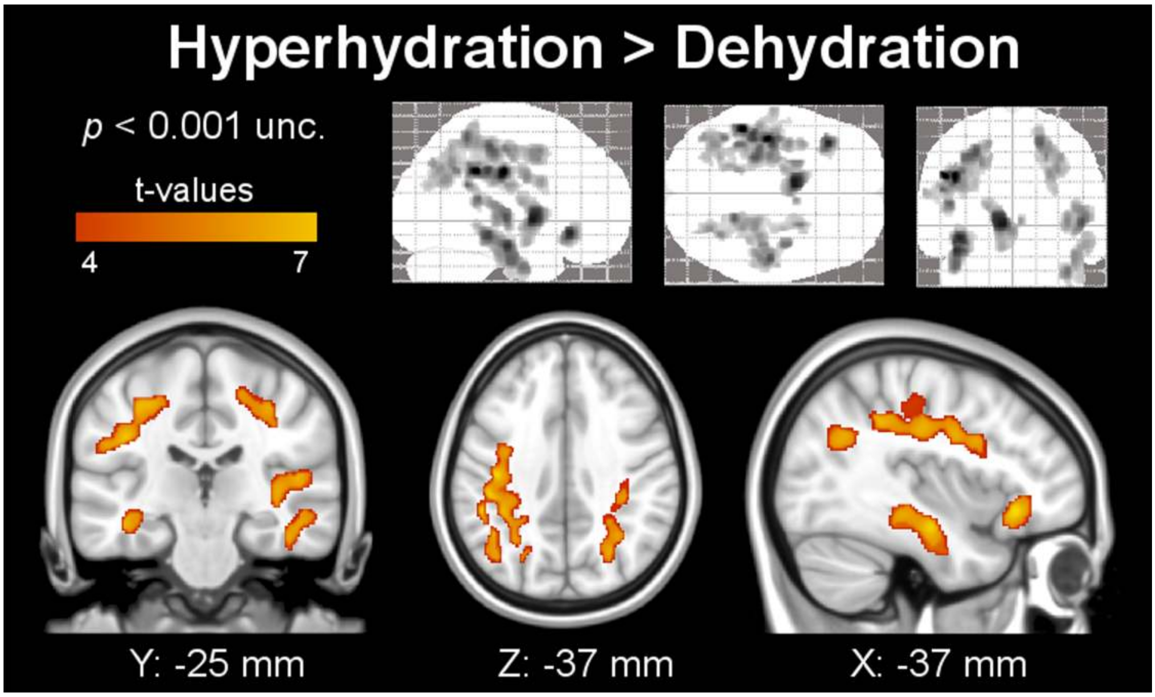

Figure 2.2: Segmented clusters of the white matter with significant extension during hyperhydration compared to dehydration in parietal and tempo-parietal regions (indicated by the color code) obtained using VBM. The upper row shows the results as grayscale Maximum Intensity Projection onto the standard SPM glass brain in coronal, axial and sagittal view.

compared to dehydration. Table 2.3 shows the cluster corrected *p*-, *t*- and *z*-values, cluster extent, and additionally the MNI coordinates of significant clusters, as shown in Figures 2.1 and 2.2. Clusters are located bilaterally in the temporal lobes and sub-gyral parietal areas, the left inferior orbito-frontal region, and the extra-nuclear region. In addition, Figure 2.3 shows the extent of both lateral, the third, and the fourth ventricle during dehydration as compared to hyperhydration on segmented images of CSF. All VBM results show clusters (color-coded in yellow), which remained significant after family-wise error correction ($p < 0.05$) and correction for non-stationarity.

Figure 2.4 and Table 2.4 shows the summed volumes of the third, fourth and both lateral ventricles segmented with FreeSurfer for all hydration states. Due to technical issues, the second measurement during dehydration had to be skipped for the fifth subject. The segmentation results were therefore analyzed in two different ways

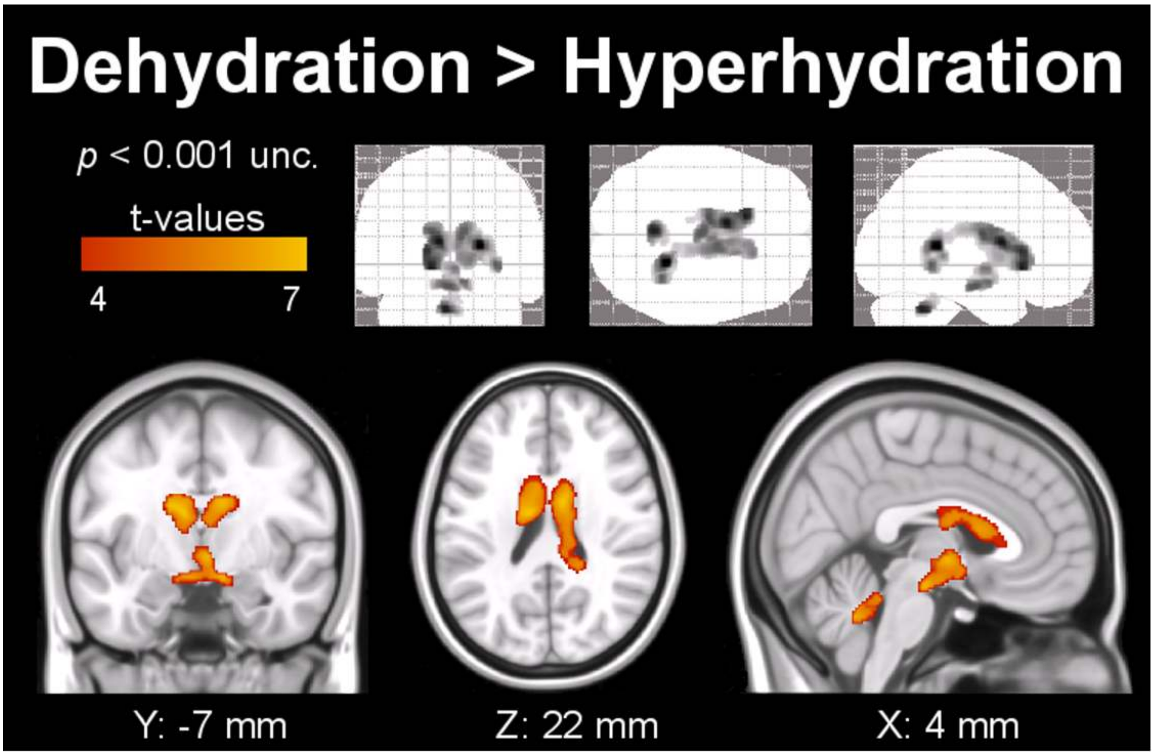

Figure 2.3: Segmented clusters of the cerebrospinal fluid system with significant extension during dehydration compared to hyperhydration in the third, fourth, and both lateral ventricles (indicated by the color code) obtained with VBM. The upper row shows the results as grayscale Maximum Intensity Projection onto the standard SPM glass brain in coronal, axial and sagittal view.

using repeated measurements ANOVA. In the first approach, statistical analysis was performed without subject 5, whereas in the second approach, the ANOVA was performed without the second measurement during dehydration. The results show a statistically significant effect with both approaches: $F(4,16) = 4.54$, $p = 0.012$ and $F(3,15) = 7.37$, $p = 0.003$, respectively. Percentage increase of the ventricular volume in comparison to the baseline scan under normal hydration is shown in Figure 2.5.

One-tailed paired *t*-tests comparing the individual measurements during dehydration against hyperhydration (set to 100%) revealed significant differences for all tests (dehydr.$_1$: average volume change, $\Delta v = 6.2 \pm 1.8\%$, $t = 8.67$, $p < 0.0002$; dehydr.$_2$: $\Delta v = 4.4 \pm 3.6\%$, $t = 2.73$, $p < 0.027$; dehydr.$_3$ $\Delta v = 5.4 \pm 2.7\%$, $t = 4.83$, $p < 0.004$). In a real-life scenario, it is highly improbable that intentional hyperhydration is followed by unintentional dehydration. Rather, the latter, unintentional, bias is the more relevant. To assess hydration effects more realistically, we accordingly compared dehydration to "normal hydration" (first scan) status. While the ventricular volume consistently increased from hyperhydration to dehydration in the first analysis, changes between normal hydration (set to 100%) and dehydration were more subtle, showing more variation between subjects.

For this comparison (i.e., when setting the baseline result to 100%), changes during dehydration did not reach significance in one-tailed paired *t*-tests (dehydr.$_1$: Δv = 2.6±4.6%, t = 1.37, p < 0.115 | dehydr.$_2$: Δv = 0.9±2.7%, t = 0.77, p < 0.243 | dehydr.$_3$: Δv = 1.7±3.1%, t=1.31, p < 0.124). The significant average volume change during hyperhydration compared to normal hydration was –3.5±3.6% (t = –2.35, p < 0.034). We note that inclusion of images with different contrast, for example T_2-weighted scans, might improve the sensitivity due to an improved contrast between CSF and surrounding tissues and, hence more accurate CSF segmentation results. Analysis of dynamic changes during dehydration to investigate the effect described by Gullans and Verbalis (1993) in rats did

p_{FWE}	k_e	*t*-value	*z*-value	MNI *x* [mm]	MNI *y* [mm]	MNI *z* [mm]
0.005	**638**	**6.21**	**4.53**	**−14**	**24**	**0**
0.018	**184**	**5.62**	**4.26**	**−2**	**−72**	**−27**
0.025	**378**	**5.53**	**4.22**	**6**	**−72**	**−27**
0.000	4823	7.06	4.89	−48	−39	34
0.001	1201	6.48	4.65	−8	2	1
0.014	479	6.27	4.56	−38	29	−9
0.000	1057	6.09	4.48	−40	−16	−17
0.001	765	5.68	4.29	50	−18	3
0.000	2630	5.50	4.20	20	−46	57
0.001	1010	5.22	4.06	39	−4	−32

Table 2.3: Significant results of the VBM gray and white matter analysis using an 8-mm^3 smoothing kernel and non-stationarity correction, as it is shown in Figures 1 and 2. Cluster-corrected *p*-, *t*- and *z*-values, cluster extent, k_e (in voxels) and MNI coordinates of significant clusters found in GM and WM in hyperhydration compared to dehydration. GM results are presented in bold.

not yield additional significant effects (not shown).

Furthermore, consideration of the subjects' individual fluid intake in the statistical analysis did not improve the results.

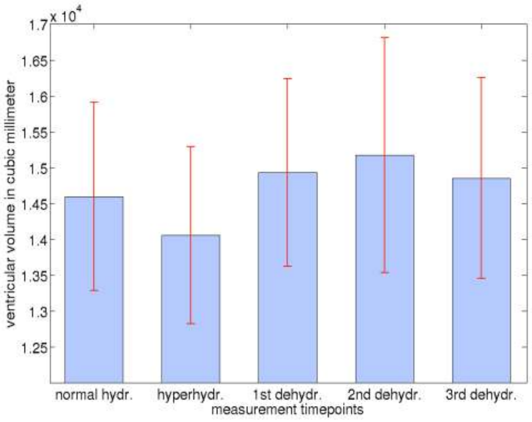

Figure 2.4: Volume of the ventricular system in mm^3 (sum = lateral + 3rd + 4th ventricle) obtained with FreeSurfer for each hydration state. Red lines indicate standard error.

SIENAr results did not show significant edge motions due to dehydration if statistics were corrected for multiple comparisons. When using an uncorrected voxel threshold (Figure 2.6), dehydration effects were observed in similar regions as described by Kempton et al. (2009). In our cohort, main effects were obtained around the 3rd and 4th ventricle and the brain stem, and minor effects were visible around the right lateral ventricle. Additional edge motions were detected in occipital areas. Statistical computation of the mixed-effects model for detecting cortical thickness changes with FreeSurfer did not yield significant results for hyperhydration (assuming thickening of the cortical surface) compared to dehydration (assuming thinning of the cortical surface).

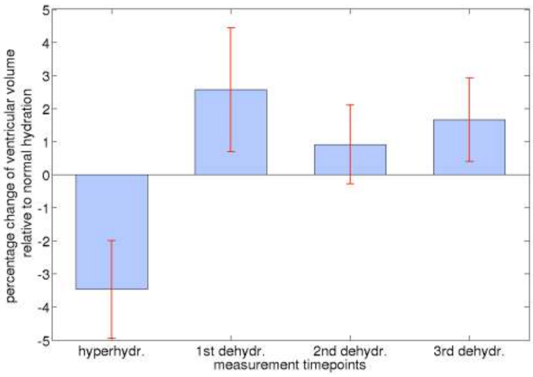

Figure 2.5: Ventricular volume change, obtained using FreeSurfer segmentation results, in percent in comparison to normal hydration (set to 100 %). Red lines indicate standard error.

2.4. Discussion

With the current study, we demonstrate structural brain changes due to dehydration separately for all major brain compartments. Consistent changes upon dehydration were revealed in GM, WM, and in the ventricular system employing VBM and its GLM approach. Additionally, we assessed the reliability of VBM in investigating CSF by using FreeSurfer as a reference method. SINEAr results agreed with previously published findings, when using an uncrorrected voxel threshold. FreeSurfer measurements of cortical thickness did not detect significant changes in hyperhydration compared to dehydration.

Gray matter volume reductions due to dehydration compared to hyperhydration were found using VBM in the left caudate nucleus and right-cerebellar posterior lobe. Although the left caudate nucleus is also one of the regions that are affected in AD (Guo et al., 2010; Karas et al., 2004), we are not aware of any study suggesting a particular usage of this region in the diagnosis of AD or assessment of disease progression.

Subject	'Normally hydrated'	Hyper-hydrated	Dehydrated		
	t=0	*t*=10h	*t*=48h	*t*=53h	*t*=58h
1	11.797	11.492	11.915	11.568	11.682
2	18.450	17.802	19.096	18.934	19.379
3	17.228	17.185	18.114	17.963	17.856
4	10.884	10.884	11.820	11.011	11.335
5	12.571	11.995	12.852	*	12.661
6	16.645	14.998	15.800	16.388	16.208
Mean ± SD	14.6 ± 3.2	14.1 ± 3.0	14.9 ± 3.2	15.2 ± 3.7	14.9 ± 3.4

Table 2.4: Volume of the ventricular system in ml obtained with FreeSurfer for each subject. SD is standard deviation. Missing volume data are indicated by an asterisk.

Cortical GM changes resulting in thinning or thickening due to, respectively, dehydration or hyperhydration were not detected using FreeSurfer. This is most probably due to the small sample size

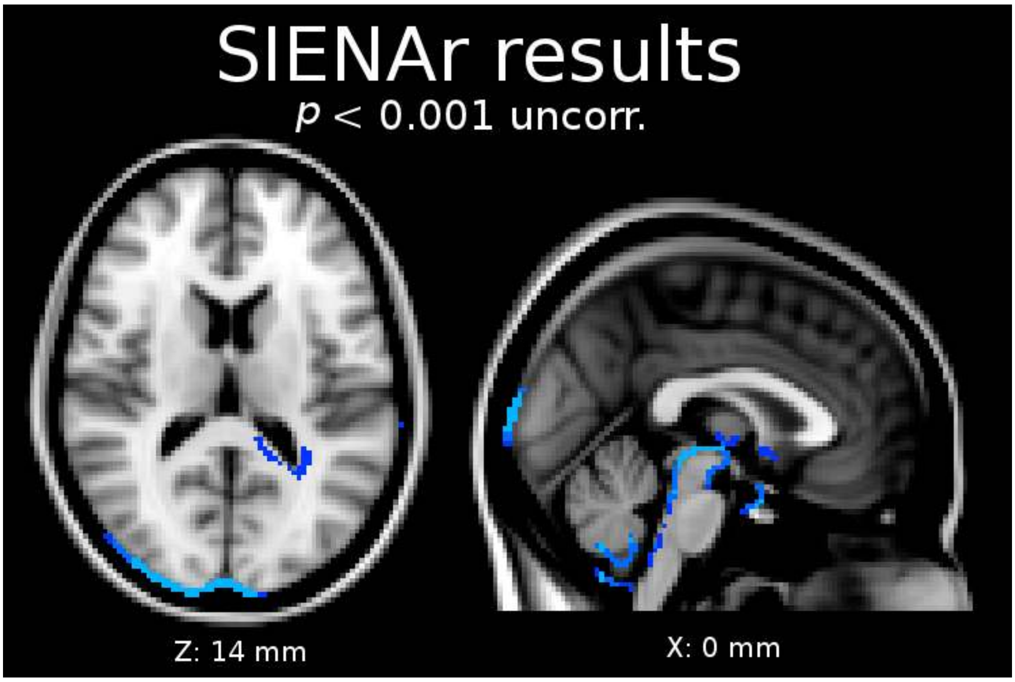

Figure 2.6: Blue color shows effects due to dehydration in regions of the third, fourth, and right lateral ventricle computed with SIENAr (voxel level, uncorrected). Additionally, effects in the region of the occipital cortex were detected.

combined with the rather weak effect of thinning and thickening in different hydration states. Reducing the voxel size and thereby reducing partial-volume effects and improving cortex segmentation might further help to detect cortical thickness changes (Tardif et al., 2010). White matter volumetric results showed larger and more widespread results compared to GM. We found a significant decrease of tissue volume during dehydration compared to hyperhydration. Moreover, affected regions largely overlap with areas of WM loss also reported in AD studies (Guo et al., 2010), such as the temporal lobe, corpus callosum, inferior longitudinal fasciculus, inferior frontal gyrus, and sub-gyral parietal lobe. Consequently, VBM studies investigating WM changes should consider controlling for the subjects' hydration state to avoid potential confounds by dehydration.

The observed shrinkage of WM volume during dehydration is consistent with the report of a decreased apparent diffusion coefficient during dehydration (Righini et al., 2005). This supports the assumption of a loss of WM tissue water, which reduces the available space for water diffusion.

The observation of substantial differences in the degree of hydration-related changes between GM and WM might be due to partial volume effects (Tardif et al., 2010). In particular, in folded cortical regions, a nominal spatial resolution of 1 mm as employed in our study is insufficient for a clear distinction of GM from WM/CSF, which decreases the statistical power due to high classification variability. In contrast, segmentation stability across subjects is better in many areas of WM.

Our CSF results obtained with VBM showing an increased volume of the lateral ventricles upon dehydration are consistent with previous studies based on different methodological approaches (Dickson et al., 2005; Duning et al., 2005; Kempton et al., 2009). Furthermore, our study extends previous results by detecting volume changes in the entire ventricular system including the fourth ventricle. This observation is consistent with the expectation that a global effect like dehydration would cause cell shrinkage and osmolality changes throughout the brain and should, hence, affect the entire ventricular system (Gullans and Verbalis, 1993).

Furthermore, our SIENAr results are in line with the literature (Kempton et al., 2009). One has to keep in mind that they were only based on an uncorrected voxel-wise threshold. In this context, the limited number of subjects is even more important due to the two time-point estimation approach of SIENAr: Statistical tests with SIENAr can assess only two time points, whereas our VBM study design benefits form the repeated measurements (n = 3) during dehydration, which increases the degrees of freedom and thereby the statistical power. This assumption is corroborated by the observation that significance was also not reached employing VBM, when the analysis was restricted to a paired t-test comparing the measurement during hyperhydration to the first measurement during dehydration.

A possible explanation of the—at first sight counterintuitive—finding of ventricular expansion in dehydration is discussed by Gullans and Verbalis (1993). Dehydration is accompanied by decreased blood volume (hypovolaemia) (Berk and Rana, 2006). This might contribute to reduced brain volume and an associated increase of the volume of the ventricular system (Dickson et al., 2005). Acute dehydration also increases serum osmolality (hypernatremia), which generates an osmotic gradient and therefore results in an increased diffusion of water from intracellular stores into extracellular space. This process causes cell shrinkage, in particular of astrocytes, which play an important role in water transport, and thereby leads to an expansion of the ventricular system (Simard and Nedergaard, 2004).

The change in ventricular volume depending on the hydration status may now be compared with observations in diseases. Dehydration would only have a negligible effect in schizophrenia and multiple sclerosis in view of reported average ventricular increases by 26% (Wright et al., 2000) or 20-26% (Brex et al., 2000; Turner et al., 2001), respectively. However, one year follow-up studies showed volume increases by 5-16% in AD patients and by 3.5% in MCI patients (Nestor et al., 2008). Such changes are of the same order as the increase of 6.2±1.8% between hyperhydration and dehydration observed in our study. Hence, dehydration might be misclassified as a consequence of AD or MCI. In a recent study with different subgroups of Parkinson's disease, ventricular enlargement ranged between 7 and 25%, depending on subgroups (Apostolova et al., 2010). Although these changes exceeded those observed in our study, an influence from different fluid balances on misclassification cannot be excluded.Finally, volume changes due to dehydration as obtained by VBM were consistent with simultaneously obtained FreeSurfer results. We may thus conclude that VBM reliably permits detection of subtle changes in the CSF system. It may thus be applied not only for GM and WM segmentation but additionally in studies of CSF.

Based on the above discussion, control of the hydration status is indicated when investigating GM and WM volume or the ventricular system. However, volume change due to hyperhydration followed by long-term dehydration is not a realistic scenario for disease studies. Involuntary dehydration starting from a normal hydration state seems more likely, as summarized in Figure 2.4. Thus, a ventricular expansion by approximately 2.6% after 40 hours of thirsting may be assumed to be a realistic amount of uncertainty in studies investigating the ventricular system without correcting for the hydration status. Similar results can be expected for GM and WM volume changes.

Comparable reductions of changes were described in animal studies (Gullans and Verbalis, 1993) demonstrating a steady decline of the dehydration effect on the ventricular system in rats. After 21 days of thirsting, differences to baseline could no longer be observed. Such a regulation might be the same for the whole human brain and therefore long-lasting dehydration might result in a smaller impact compared to the maximum increase from hyperhydration to dehydration revealed in this study. A simple possibility to correct for the acute form of the dehydration confound is to ensure a certain amount of fluid intake of every subject in advance of scanning. Instructions describing guidelines for sufficient fluid intake approximately 24 hours before scanning should diminish dehydration effects and establish improved comparability between subjects (Gullans and Verbalis, 1993).

3. Detecting Associations between Structural Brain Measures and Blood Serum Biomarkers using Voxel-Based Statistics

After investigating GMD changes using VBM, the following section describes the sensitivity of TBSS in detecting associations between blood serum proteins and related white matter changes. Recently, researchers found evidence that the human blood serum marker S100B, which is associated with oligodendrocytes and mainly located in WM, is associated with neuropsychiatric disorders such as major depression or schizophrenia (Rothermundt et al., 2003; Rothermundt et al., 2002; Rothermundt et al., 2004; Schroeter et al., 2008; Schroeter et al., 2009a; Steiner et al., 2010a; Steiner et al., 2010c). Interestingly, none of the studies showed white matter specific structural changes which were linked to the changed S100B serum level. Evaluations of the sensitivity correlating blood serum markers with white matter sensitive measures such as FA are needed. This study might offer new perspectives for future studies and can help to understand underlying mechanisms and treatment procedures for neuropsychiatric disorders. In the following chapter, the sensitivity of TBSS for the detection of associations between S100B and WM sensitive biomarkers is evaluated.

3.1. Introduction

Former studies investigated the potential of serum proteins as biomarkers for brain diseases. In particular, the glial protein S100B has been discussed in this context (Poelmans et al., 2011; Schafer and Heizmann, 1996; Schroeter and Steiner, 2009). S100 proteins influence various cellular responses along the calcium-signal-transduction pathway (Donato, 1999; Schafer and Heizmann, 1996; Zimmer et al., 1995). S100B is localized in and may be secreted by astro- and oligodendrocytes. In nanomolar concentrations it acts as growth and/or differentiation factor for neurons and glia, whereas in micromolar levels S100B may have deleterious effects and induces apoptosis due to an increased expression of proinflammatory cytokines (Rothermundt et al., 2003; Steiner et al., 2007). Recently, it has been suggested that S100B may play a crucial role in the pathogenesis and treatment of frequent psychiatric disorders such as major depression and schizophrenia (Rothermundt et al., 2003; Rothermundt et al., 2002; Schroeter et al., 2002; Schroeter et al., 2003; Schroeter et al., 2008; Schroeter et al., 2009a; Schroeter and Steiner, 2009; Steiner et al., 2010b). Antidepressive drugs lead via the serotonergic system to astrocytic S100B secretion, which in turn may induce neurogenesis required for the behavioral effects of antidepressants (Schroeter et al., 2008; Schroeter et al., 2010). Consequently, S100B-related mechanisms have been proposed as potential targets for novel antidepressive therapies.

Accordingly, one might assume that increased serum S100B might reflect an ongoing regenerative action in neuropsychiatric diseases. However, serum S100B, which might not reflect local concentrations in the brain, was rather elevated in acute stages of depression and schizophrenia and positively correlated with depressive symptoms and negative symptoms in schizophrenia. Accordingly, clinical data suggest serum S100B rather as a pathological biomarker than plasticity marker (Rothermundt et al., 2003; Schroeter et al., 2008; Schroeter et al., 2009a). In agreement with these arguments genetic studies demonstrated that S100B is a susceptibility gene for mood disorders and schizophrenia (Schroeter and Steiner, 2009), developmental dyslexia (Poelmans et al., 2011) and cognitive dysfunction (Lambert et al., 2007). In sum, serum S100B may constitute a diagnostic, prognostic and treatment biomarker for major depression, schizophrenia and neurological diseases (Steiner et al., 2011; Stroick et al., 2006). Beside S100B, neuron-specific enolase (NSE) has been suggested to be a specific serum marker for neuronal damage. Because NSE is primarily localized in the cytoplasm of neurons (de Kruijk et al., 2001; Ingebrigtsen and Romner, 2003; Kaiser et al., 1989; Marangos and Schmechel, 1987; Schmechel et al., 1978) and is not secreted, increases in cerebrospinal fluid or blood indicate structural damage to neuronal cells.

Although serum S100B and NSE offer the opportunity to easily investigate the function of or damage to glial and neuronal structures in neuropsychiatric disorders (Busnello et al., 2006; Schaf et al., 2005; Schroeter et al., 2008), the specificity of these biomarkers for cell type and brain region have not been investigated in vivo until now. Magnetic resonance imaging (MRI) is very sensitive in identifying regional structural changes in the human brain. Voxel based morphometry (VBM) (Ashburner and Friston, 2000) has enabled a wide variety of studies focusing on gray matter (GM) changes (Chen et al., 2007; Good et al., 2001a; Smith et al., 2007) in various diseases (Brenneis et al., 2003; Karas et al., 2003; Kassubek et al., 2004; Pannacciulli et al., 2006), due to training (Colcombe et al., 2006; Draganski et al., 2004; Maguire et al., 2000) or genetic effects (Meyer-Lindenberg et al., 2008; Meyer-Lindenberg et al., 2007; Pezawas et al., 2004) using T_1-weighted images. With another MRI-based approach, diffusion tensor imaging (DTI) (Basser et al., 1994), one may specifically analyze white matter (WM) changes, for instance with the software package tract-based spatial statistics (TBSS) developed by the Oxford Centre for Functional MRI of the Brain (FMRIB) (Smith et al., 2006). In addition to the most important DTI parameter fractional anisotropy (FA) (Basser and Pierpaoli, 1996) indicating global WM integrity (Kochunov et al., 2007), axial and radial diffusivity are markers for axonal and myelin degeneration (Song et al., 2003).

Our study aimed to isolate the regional neural correlates of glial (S100B) and neuronal (NSE) serum markers with two MRI parameters sensitive to changes in the GM and WM of the human brain. We hypothesized that S100B as an astro- and oligodendrocytic marker is associated with GM and WM parameters. For the WM, we expected the strongest effect in the corpus callosum, because this structure has an abundance of oligodendrocytes according to histological studies (Steiner et al., 2007) and shows the highest signal-to-noise ratio due to parallel orientation of numerous fibers

(Mueller et al., 2011). Additionally, we hypothesized that NSE as a neuronal marker is associated with GM parameters.

To avoid any influences of diseases on the association between regional MRI markers and serum S100B and NSE, we involved only healthy subjects. It is well known that S100B is age (Nygaard et al., 1997; Portela et al., 2002; Schroeter et al., 2011), sex (Gazzolo et al., 2003; Nygaard et al., 1997) and weight dependent (Holtkamp et al., 2008; Steiner et al., 2010a; Steiner et al., 2010c), while influences of age or sex on NSE are controversially discussed (Casmiro et al., 2005; Nygaard et al., 1998; van Engelen et al., 1992). Moreover, recent studies combining serum markers and WM parameters found different results for female and male subjects (Mueller et al., 2011). To control for these influences, we analyzed data separately in female and male subjects, included a wide age range, and controlled for influences of age, body mass index (BMI) and total intracranial volume (TIV). Finally, we validated our results by additionally investigating gene expression in the whole human brain genome wide atlas of the Allen Institute for Brain Sciences and by histological co-localization studies in human post mortem brain and in cell culture.

3.2. Methods

3.2.1. Subjects

Forty-one healthy Caucasian adults participated in the study (20 male/21 female; mean age 50.35±21.61/46.38±24.44 years; range 21–74/20–79). All participants gave written informed consent. They completed a health history questionnaire. The research protocol was approved by the Ethics Committee of the University of Leipzig, and was in accordance with the latest version of the Declaration of Helsinki.

3.2.2. T_1-weighted Magnetic Resonance Imaging

Scanning was performed on a 3T TIM Trio device (Siemens Medical Solutions, Erlangen, Germany). T_1-weighted images were acquired with a three-dimensional magnetization prepared rapid gradient echo (MP-RAGE) sequence using the following parameters: inversion time 650 ms, repetition time *(TR)*=1.3 s, *TR* of the gradient-echo kernel 10 ms, echo time 3.46 ms, flip angle 10°, bandwidth 130 Hz/pixel, acquisition matrix 256×240, field of view 256×240 mm^2, slab thickness 192 mm (sagittal orientation), 128 partitions, 95% slice resolution. Reconstructed images were obtained with a nominal voxel size of 1×1×1 mm^3.

3.2.3. Diffusion Tensor Imaging

Diffusion-weighted images were acquired with twice-refocused spin echo echo-planar-imaging sequence [46], TE = 100 ms, TR = 12 s, 128x128 image matrix, FOV = 220x220 mm^2: 88 axial slices (no gap); voxel size: 1.72x1.72x1.7 mm^3. Additionally, fat saturation was employed together with 6/8 partial Fourier imaging and generalized auto-calibrating partially parallel acquisitions (GRAPPA (Griswold et al., 2002), acceleration factor=2). Diffusion weighting was isotropically distributed along 60 diffusion-encoding gradient directions with a b-value of 1000 s/mm^2.

3.2.4. Measurement of Serum Markers

Blood samples were obtained by venipuncture from subjects. Analysis was performed as previously described in detail (Schroeter et al., 2008; Schroeter et al., 2009a). S100B and NSE were measured by monoclonal 2-site immunoluminometric assays performed on the fully mechanized system LIAISON (Diasorin, Dietzenbach, Germany). The detection limit for the assays was 0.02 µg/l and 0.04 µg/l.

3.2.5. Voxel Based Morphometry

T1-weighted images were processed using VBM8, implemented by Gaser *et al.* (http://dbm.neuro.uni-jena.de/vbm/) for the Statistical Parametrical Mapping software (SPM, ver. 8.xx). GM segments were non-linearly registered, modulated (Good et al., 2001b) and smoothed using a 5mm^3 smoothing-kernel. Resulting images were fed into a multiple regression model using S100B (or NSE) as regressor of interest and NSE (or S100B), BMI, TIV and age as confounding covariates. GM images were threshold to exclude voxels with a GM probability below 10% prior to the statistical analyses. Significant resulting brain structures were identified by the TD-ICBM Human Atlas (Maldjian et al., 2003) and a volume of interest (VOI) analysis over both groups of subjects was created based on this masks. Averaged voxel values were correlated with the obtained biomarker levels using partial correlation in MATLAB (version 7.11.0/R2010b, Natick, Massachusetts: The MathWorks Inc., 2012) controlling for the same parameters as described above. To proof the significance of the difference of the correlation coefficients we used a formula which has been described in (Brandner, 1933).

3.2.6. Tract-Based Spatial Statistics

Secondly, we analyzed DTI datasets using TBSS from the FMRIB Software Library (FSL) (Smith et al., 2006). We followed the recommended preprocessing steps with default parameters described on their homepage (http://www.fmrib.ox.ac.uk/fsl/tbss/index.html). After preprocessing, we fed the images into a multiple regression analysis using FSLs ‘randomise’ program, with the same statistical design as it is described above and computed a randomize statistics with 100.000 permutations. Results were thresholded by the threshold-free cluster enhancement (TFCE) approach (p< 0.05 corrected). TFCE is a technique which aims to enhance cluster-like structures and simultaneously ignores noisy regions in statistical images without explicitly defining a hard-threshold-based clustering (Smith and Nichols, 2009). Furthermore, we followed the same VOI statistical procedure for significant identified brain structures as above. Due to the different analyzed tissue we used the anatomical atlas from TD-ICBM Human Atlas to the Johns Hopkins University ICBM white-matter-labels (Wakana et al., 2007). All statistics, TBSS as well as VOI analysis, were applied on the skeletonized FA, radial ($\lambda_{\perp}$) and axial diffusivity data ($\lambda_{\parallel}$).

3.2.7. Histological Analyses – Post Mortem and Cell Culture

The brain of a 32 year old Caucasian woman (who died from acute myocarditis associated with lupus without brain involvement), which is not included in our imaging study, was removed from the cranium within 20 hrs after death. A tissue sample from the corpus callosum was fixed in 4% buffered paraformaldehyde (pH 7.4), cryoprotected, and rapidly frozen at -20°C using 2-methylbutane. Serial sagittal 20 µm thick sections were cut on a cryostat (Jung Frigocut 2800 E, Leica, Bensheim, Germany). Oligodendroglial OLN-93 cells were obtained from the Richter-Landsberg lab

(Oldenburg, Germany) and cultured as previously described (Steiner et al., 2010b). Free-floating sections or OLN-93 cultures were washed and incubated with the corresponding antibodies: (i) polyclonal rabbit anti-recombinant-S100B 1:50; (ii) monoclonal mouse anti-myelin basic protein 1:100, (iii) monoclonal mouse anti-p75 neurotrophin receptor 1:100 with 0.3% Triton X-100 and 1% normal goat serum overnight at 4°C. This step was followed by incubation for 3 h with the respective secondary antibodies at a 1:500 dilution: Alexa Fluor 546 (goat anti-rabbit-IgG; red fluorescence) and Alexa 488 (goat antimouse-IgG; green fluorescence). Specimens were examined using a fluorescence microscope (Axiophot; Zeiss, Jena, Germany) equipped with phasecontrast, fluorescein and rhodamine optics. The specificity of the immunoreactions was controlled by the application of buffer instead of the primary antiserum.

3.2.8. Whole Brain Genome Expression Analysis

The Allen Human Brain Atlas is a publicly available online resource of gene expression (www.human.brain-map.org; (Jones et al., 2009)). It characterizes gene expression in human brain tissue with genome-wide microarray-based gene expression profiles including over 62,000 gene probes for 500 samples from each hemisphere covering the whole brain. Tissue samples collected for microarray analysis were processed for RNA isolation, quantification, and normalization. Microarray analysis data, normalized across each brain, are included in the Allen Human Brain Atlas dataset and illustrated in heat map format as z scores. Z scores represent individual regional gene expression normalized to whole brain expression of that gene. When there are multiple samples for a given structure and subject, values in the heat map are average values. Quality control was performed several times. To date, three subjects without a history of neuropsychiatric or neurological conditions are contained in the database (H0351.1009, H0351.2001, H0351.2002; age 57, 24, 39 years; all male; ethnicity white/Caucasian

[.1009], and black/African American [.2001/.2002]). Note that these subjects were not included in our imaging study. Detailed information for subjects included and analysis methods is available at www.human.brain-map.org. To calculate mean values of normalized expression in brain regions of interest we extracted normalized z scores from the database for each individual and region of interest. Thereafter, expression values were compared with two-tailed Student’s t tests.

3.3. Results

3.3.1. Serum Markers

Because serum S100B might be influenced by sex, age and body mass index, we controlled for these factors. In accordance with literature data (Gazzolo et al., 2003) mean serum S100B levels were higher in female (65.7±26.6 ng/l) compared to male subjects (54.0±16.4 ng/l; ‘trend’ *p*=0.1), whereas there were no sex related differences for serum NSE (females 9.68±1.75 µg/l; males 10.27±1.96 µg/l; *p*=0.31; two-sample Student’s t-test; generally, *p* values for two tailed tests). Serum S100B and NSE values did not correlate within the group of female subjects (*p*=0.22), but correlated positively within the group of male subjects (*p*<0.05; Pearson’s correlation). Age and body mass index were not correlated with S100B or NSE if calculated in female and male subjects alone or in the whole group. Accordingly, we analyzed correlations between serum markers as regressors of interest and imaging parameters in both sex groups separately and, in general, controlled for the respective second serum marker beside age and body mass index (and total intracranial volume) as confounding covariates in the following analyses.

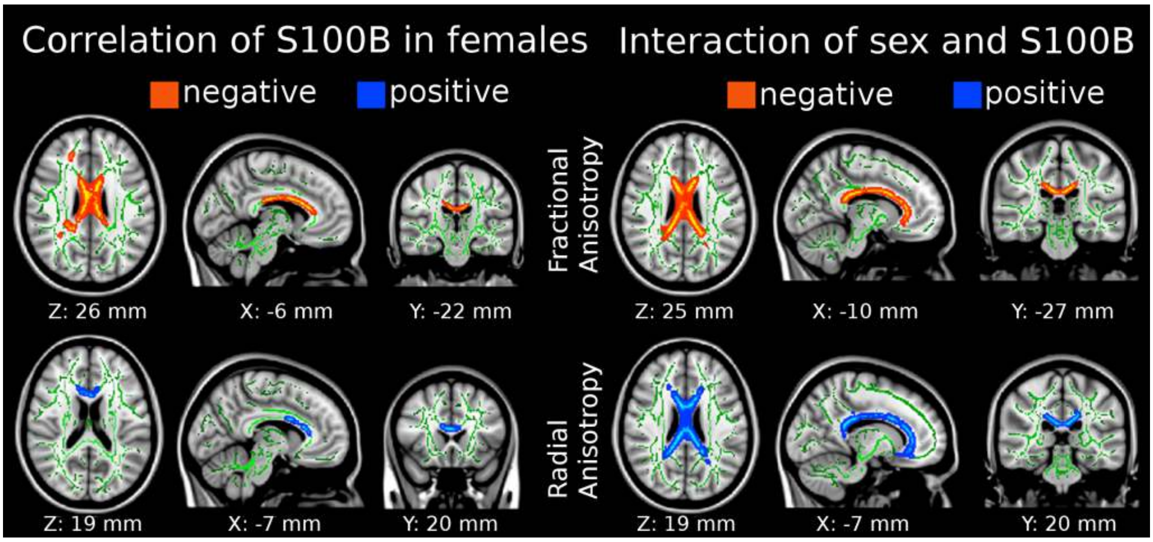

Figure 3.1: Diffusion tensor imaging parameters correlate with serum S100B mainly in the corpus callosum, anterior forceps, and the right superior longitudinal fasciculus of the female brain (left) in comparison with male brains (right). Clusters are corrected for multiple comparisons ($p < 0.05$, threshold-free cluster enhancement), positions are reported in MNI-coordinates. There was no significant correlation of S100B in male brains alone using multiple comparison correction and very little using uncorrected thresholds (not shown). Radiological convention (left side of the brain is presented on the right).

3.3.2. Combining Serum Markers and Diffusion Tensor Imaging

Both S100B and NSE serum markers were analyzed for their explanatory power for the DTI data, separately for FA, radial and axial diffusivity. For NSE, we did not obtain any significant results with the chosen statistical threshold. In contrast, serum levels of S100B were correlated with regional DTI parameters in female subjects, which was not the case for male.

TBSS results are presented in Figure 3.1. We show a significant negative correlation between S100B and FA across the anterior portion (rostrum, genu) and body of the corpus callosum, particularly the right anterior forceps, and the right superior longitudinal fasciculus (left upper row of Figure 3.1). No significant effects were detected for the posterior portions of the corpus callosum (splenium, tapetum). Additionally, we were able to show a significant positive correlation of S100B with radial diffusivity but not with axial diffusivity for the genu and anterior body of the corpus callosum, and for the anterior forceps (left lower row of Figure 3.1). In male subjects no such an association was detected – applying both corrected and uncorrected thresholds.

We aimed to confirm this result and compare female and male groups in a regional analysis focusing on the most consistent brain region, the corpus callosum. As illustrated in Table 3.1, VOI analyses revealed significant correlations in the female corpus callosum and therefore confirmed the previously described TBSS results. Interestingly, FA values were negatively correlated with S100B, whereas regional radial diffusivity was positively correlated with serum S100B. In men, we did not find any significant correlation with S100B and FA, radial or axial diffusivity measures using this regional approach. Furthermore, a permutation test with 100,000 permutations regarding S100B serum levels and FA/radial diffusivity revealed significant gender differences in women compared to men (Table 3.1).

sex	*p*-value	correlation coefficient	significance of difference between correlation coefficients
		Fractional Anisotropy	
female	**0.01**	**-0.59**	*p*-value
male	0.26	0.3	**0.004**
		Axial diffusivity ($\lambda_{\parallel}$).	
female	0.91	-0.03	*p*-value
male	0.7	0.11	0.68
		Radial diffusivity ($\lambda_{\perp}$)	
female	**0.01**	**0.61**	*p*-value
male	0.22	-0.31	**0.002**

Table 3.1: Correlation values and permutation results for S100B, fractional anisotropy, radial and axial diffusivity in the corpus callosum. Note: Significant effects are written in bold.

The same result, which was obtained by computing the interaction effect of females and males regarding S100B levels, can be seen on the right side of Figure 3.1. Here, we show a significant lower FA (upper row, right) in the anterior parts (rostrum, genu) and body of the corpus callosum, parts of the superior longitudinal fasciculus and anterior and posterior forceps, and a significantly higher radial diffusivity (lower row, right) in the genu, rostrum and body of the corpus callosum and the anterior forceps in females compared with males. In addition to the FA results, we show significant results analyzing radial diffusivity in regions of the left external capsula and left uncinate fasciculus.

3.3.3. Combining Serum Markers and T_1-weighted Magnetic Resonance Imaging

Both S100B and NSE as glial/neuronal serum markers were analyzed for their explanatory power for T1-weighted MRI data, namely GM intensity. For S100B, we did not obtain any significant results with the chosen statistical threshold. In contrast, serum

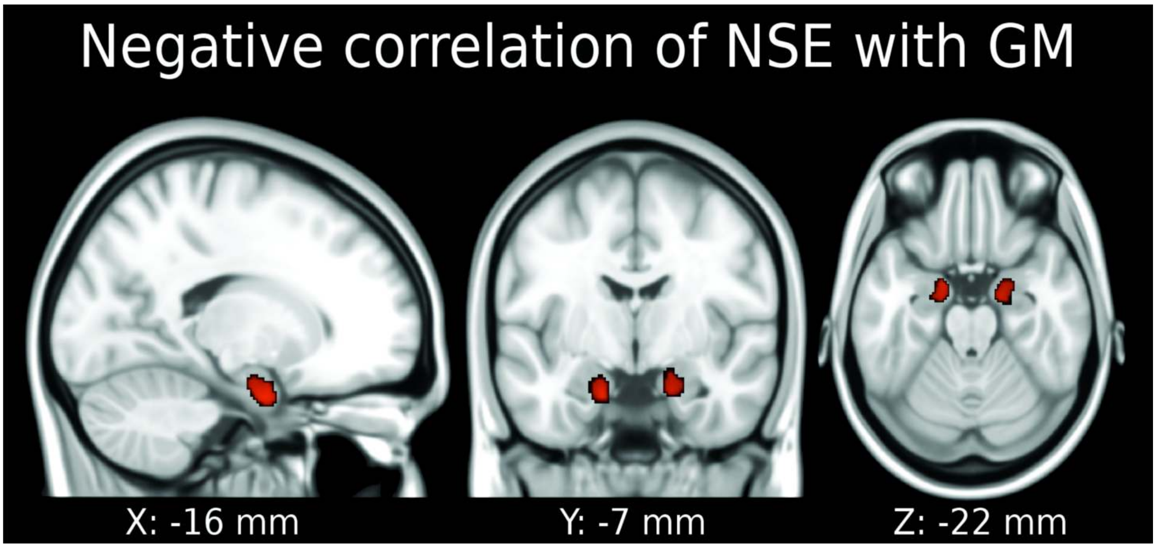

Figure 3.2: Gray matter density (GM) in both amygdalae and both most anterior hippocampi is correlated with serum neuron-specific enolase (NSE) in the female brain. No significant results were obtained for male subjects. *p*<0.05 family wise error was applied, reported coordinates are MNI coordinates. Neurological convention (left side of the brain is presented on the left).

levels of NSE were correlated with regional GM density particularly in female subjects. Results of the VBM analysis are illustrated in Figure 3.2. We report data using a voxel-wise threshold of *p*<0.001 and show clusters which remained significant after correction using a cluster-wise threshold of *p*<0.05 family wise error (FWE). In female subjects, serum NSE was negatively correlated with GM density in the amygdalae and most anterior hippocampi bilaterally. No significant effects were obtained for male subjects with the chosen statistical threshold.

sex	*p*-value	correlation coefficient	significance of difference between correlation coefficients
female	**0.0040**	**-0.66**	*p*-value
male	**0.0097**	**-0.62**	0.5

Table 3.2: Correlation values and permutation results for serum neuron-specific enolase and averaged smoothed gray matter density in the amygdalae. Note: Significant effects are written in bold.

In a second step, we aimed to confirm this result and compare female and male groups in a regional analysis focusing onto the amygdalae. We computed a VOI analysis using the TD-ICBM Human Atlas in SPM and bilaterally selected the amygdaloid structures. These structures were used as masks for both, female and male groups, and smoothed GM values were extracted. Correlation of NSE and smoothed mean GM values, again corrected for covariates, were computed for both groups separately and can be seen in Table 3.2. Interestingly, both groups showed a significant negative correlation of GM density with NSE in the amygdaloid region in this VOI analysis – in contrast to the first whole-brain VBM analysis, where only females showed this association. Nonetheless, we failed to find significant gender differences using a permutation test with 100,000 permutations. We did not find any other significant correlation, difference or interaction of NSE and GM in any other group or combination of groups.

3.3.4. Histological and Whole Brain Gene Expression Analyses

In the histological study we examined co-localization between S100B and oligodendrocyte specific antigens in the human corpus callosum and cell culture by double immunofluorescence labeling. Figure 3.3 shows a close co-localization between S100B and oligodendrocyte specific myelin basic protein-positive myelinated fibres in the human corpus callosum, and between S100B and the oligodendrocyte/Schwann cell marker p75NTR in most oligodendroglial OLN-93 cells. Note that not all S100B positive cells are labelled as oligodendrocytes in Figure 3.3B as oligodendroglial markers are not expressed during all stages of oligodendrocyte development/maturation.

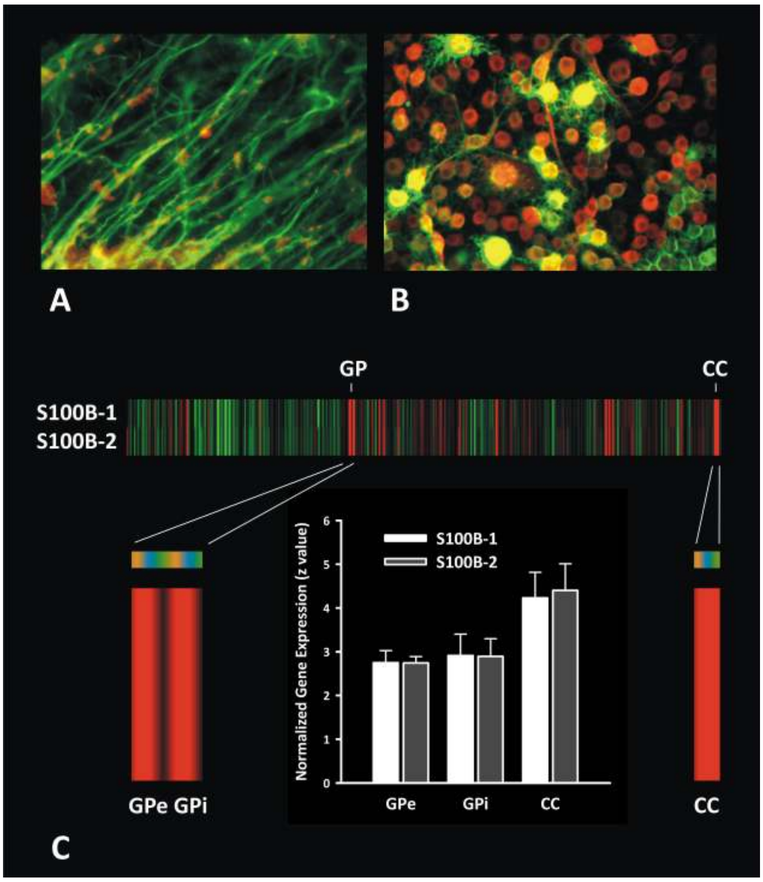

Figure 3.3: Expression & localization of S100B in the brain. (A) Co-localization (yellow) of S100B (red) and myelin basic protein (MBP)-positive (green) myelinated fibres in the human corpus callosum. Data originate from the subject previously published [6]. (B) Co-localization (yellow) between S100B (red) and the oligodendroglial marker p75 neurotrophin receptor (green) in the oligodendrocyte cell line OLN-93. (C) Individual normalized gene expression of S100B in heat map in z scores normalized to whole human brain expression, where green indicates relatively low and red relatively high expression. Subjects are coded in orange, blue and green (H351.2001, .2002 and .1009). Highest expression was detected in the corpus callosum (CC), followed by globus pallidus (GP). Bar chart shows quantitative values in CC and external/internal (e/i) GP (mean±standard deviation). Gene expression of S100B was analyzed in two probes: Probe 1 A_23_P143526;Sequence: AGCTTGATTTGCTTTGTGATTGAAAAATTGAAAACCTCTTTCCAAAGGCTGTTTTAACGG; Probe 2 CUST_17042_PI416261804; Sequence: AAGCTGAAGAAATCCGAACTGAAGGAGCTCATCAACAATGAGCTTT CCCATTTCTTAGAG.

If we analyzed S100B gene expression in the whole human brain, S100B was most abundantly expressed in the corpus callosum, followed by the globus pallidus (Figure 3.3). The bar chart illustrates normalized z scores for these brain regions. All respective regions showed elevated S100B expression (Probe 1/2 corpus callosum $p=0.006$, external globus pallidus $p<0.05$, internal globus pallidus $p=0.08/0.06$; 2-tailed Student's t test against 0), whereas there were no differences between probe 1 and 2 for each region warranting a high reliability ($p>0.74$; unpaired 2-tailed Student's t test). Gene expression of S100B was, for both probes 1 and 2, higher in the corpus callosum than the external (*p*=0.048/0.036) and internal globus pallidus (*p*=0.08/0.057) without significant differences between both segments of the globus pallidus (*p*>0.6).

3.4. Discussion

Our study aimed to validate the impact of serum markers on imaging data covering the GM and WM of the human brain. We focused on S100B because it is a glial protein that might act as a neuro- and gliotrophin inducing plasticity effects in the human brain (Haglid et al., 1997; Kligman and Marshak, 1985; Winninghammajor et al., 1989).

As already stated in the introduction section we investigated the relationship between cell type specific serum markers and imaging parameters in a healthy cohort to exclude any impact of disease, because increased serum S100B may indicate glial alterations due to brain damage (Abdul-Khaliq et al., 2000) in addition to functional secretion of S100B by astrocytes and/or oligodendrocytes (Schroeter et al., 2010). Mathematical models suggest that serum S100B levels exceeding approximately 350 ng/l indicate brain damage (Marchi et al., 2004). Mathematical equations have been developed using values derived from literature and linearly fitting those values into a function in this study. Regarding neurological diseases with obvious brain damage, e.g. Creutzfeld-disease, mean expression levels are significantly increased to 395 ng/l (Otto et al., 1998), or in traumatic brain injuries with bad prognosis above 500 ng/l (Rainey et al., 2009). Accordingly, literature data supports the mathematically derived threshold. Lower levels below 300 ng/l have been detected in neuropsychiatric disorders, such as depression or schizophrenia and might describe a regenerative action through S100B, and due to their low concentration less likely a neurodegenerative process (Schroeter et al., 2008; Schroeter et al., 2009a). Mean serum S100B was in the normal range of healthy subjects and far below this threshold in our subjects (Portela et al., 2002).

Likewise, normal NSE values exclude neuronal damage in our cohort (Casmiro et al., 2005; Schroeter et al., 2008).

Our study shows that S100B is specifically related to WM structures in the healthy human brain as it correlated negatively with FA. We observed this effect in female subjects only, which might be related to higher serum levels of S100B, higher variance and a wider range of values of this glial protein in the female study group compared to male subjects. Furthermore, to the authors' knowledge, there is no evidence to expect different expression pattern across sexes although our study shows significant correlations only within the female group. The results of the Allen Brain Atlas underpin the hypothesis of equal expression patterns across sexes, because all investigated subjects in this brain atlas are males, which show high S100B gene expression in the corpus callosum. Therefore, we conclude that due to the lower range of S100B values in our male cohort, we failed to show a significant correlation.

Our second more specific analysis revealed that correlations of serum S100B with FA in women had to be attributed to a positive correlation with radial diffusivity in the same regions without significant effects for axial diffusivity. For the GM we did not obtain any significant correlations with S100B. Remarkably, in these analyses, we corrected for potential influences of neuronal influences on DTI or VBM parameters by including the neuronal marker protein NSE as a covariate. For NSE, we did generally not detect any significant correlations with DTI parameters.

The close positive correlation of serum S100B with radial diffusivity fits well with our post mortem histological double immunofluorescence data demonstrating a high concentration of S100B in oligodendrocytes in the healthy human brain, particularly in the corpus callosum, the dorsolateral prefrontal, parietal and temporal WM (see results and Steiner et al. (2007) (Steiner et al., 2007)). Most interestingly, the Allen Brain Atlas, which provides gene expression data across the whole human brain, indicates highest expression of S100B in the corpus callosum in agreement with our results and in the globus pallidus in agreement with the literature (Cammermeyer, 1960).

In sum and to our knowledge, our study is the first one validating the specificity of the glial protein S100B for brain changes in vivo. Our results support the assumption that radial diffusivity represents a myelin marker, whereas axial diffusivity represents an axonal marker, as already shown in (Song et al., 2003), although this topic is controversially discussed (Schmierer et al., 2008). Although, all subjects were healthy we detected negative correlations with FA, which can be interpreted as a loss of directedness, and positive correlations with radial diffusivity which might be coupled with a loss in myelinisation. One should note that the obtained serum markers are whole brain measures and for the first time correlated with imaging data. Our study suggests that in healthy subjects S100B is expressed in region wise patterns, which corresponds with high S100B expression in corpus callosum and globus pallidus. High S100B is associated with a reduction of FA and increased $\lambda_\perp$ but does by no means support the idea of unhealthy or abnormal expression of S100B and/or diffusion parameters.

Beside DTI as WM parameter, both serum markers were analyzed in their explanatory power for T1-weighted MRI data by correlating them with GM density. Serum NSE was negatively correlated with regional GM density mainly in the amygdalae of both sexes, most pronounced in female subjects. One has to keep in mind that we controlled for serum S100B as a covariate in this analysis. We did not obtain any significant results for S100B in this analysis, although it is well known that human astrocytes contain and express S100B (Steiner et al., 2007). This might be related to a lower signal-to-noise ratio in the GM as it is composed of several other cell types beside astrocytes. In contrast, the close association between S100B and WM DTI parameters was observed mainly in the corpus callosum, where numerous fibers are oriented in the same direction yielding a very high signal-to-noise ratio (Mueller et al., 2011). Additionally, histological investigations showed highest concentration of oligodendrocytes in white matter in the corpus callosum, which might be an explanation for our sensitivity and the observed TBSS results (Steiner et al., 2007). This leads to the conclusion that S100B as an oligodendrocytic marker is closely related with radial diffusivity. An alternative view postulating a close relationship between S100B and astrocytes in the corpus callosum is very improbable, because 93% of S100B positive cells in the corpus callosum represent oligodendrocytes (Steiner et al., 2007). The same holds true for other structures in the white matter.

One might conclude that our study indeed investigated the ‘normal’ relationship between cell type specific serum markers and imaging parameters. Our results open a new perspective for future studies investigating major neuropsychiatric disorders – in particular major depression and schizophrenia, which have been discussed to be characterized by glial pathology (Bernstein et al., 2009; Schroeter et al., 2008; Schroeter et al., 2011) and affecting brain regions identified in our study (Sacher et al., 2011; Whitford et al., 2011).

4. Detecting Age Related Structural Brain Differences Using Different Magnetic Resonance Imaging Parameters and Voxel-Based Morphometry

The following section deals with the sensitivity of scanning parameters and their impact on VBM results. Regarding the sensitivity of voxel-wise detection methods in detecting subtle effects, such as dehydration or correlations of WM parameters with blood serum biomarker levels, consequently raises the question of the best suitable scanning parameter set to increase detection sensitivity using voxel-wise statistical measures. Several improvements, like field-strength, head array technique or sequence optimization, might be beneficial for voxel-wise methods but has not been investigated yet. Systematical investigation of sensitivity variations due to changing scanning parameters will consequently help to identify the best suitable parameters for the detection of minimal morphological changes in the brain with an acceptable accuracy. Very little is known about the impact of the SNR or scanning sequences on VBM results, but investigations might help to understand the underlying mechanisms which increase detection sensitivity. Increasing sensitivity would be very beneficial for the diagnosis of neuropsychiatric diseases such as e.g. AD, Huntington`s Disease, Parkinson`s Disease and additionally improves the accuracy to detect plasticity changes induced via a study design e.g. Draganski et al. (2004) in juggling.

4.1. Introduction

Over the past decade, an increasing number of studies have used voxel-based morphometry (VBM) for assessing structural brain changes (Draganski et al., 2011; Ferreira et al., 2011; Good et al., 2001b; Hutton et al., 2009). VBM is a whole-brain technique to investigate so-called local tissue-density changes, typically employing three-dimensional (3D) T_1-weighted magnetic resonance imaging (MRI) data sets. Recent developments led to an increased accuracy of segmentation (Ashburner and Friston, 2005) and registration (Ashburner, 2007; Ashburner and Friston, 2005; Klein et al., 2010) and, thereby, to improved statistical assessment. Besides sophisticated image processing, the quality of the input images is also important in VBM; for example, a sufficient signal-to-noise ratio (SNR) and contrast-to-noise ratio (CNR), and minimal image artifacts are of critical importance. However, only some studies have systematically investigated the impact of image acquisition parameters, including the employed pulse sequence, on VBM and whole-brain measures (Acosta-Cabronero et al., 2008; Helms et al., 2009; Klauschen et al., 2009; Krueger et al., 2012; Pereira et al., 2008; Shuter et al., 2008; Stonnington et al., 2008; Tardif et al., 2009, 2010).

To study the influence of resolution, Pereira et al. (2008) used different interpolated voxel sizes comparing patients with Alzheimer`s disease and patients with semantic dementia to healthy controls. They showed that interpolation effects are highly dependent on the acquired image volume itself and have to be treated carefully. In two studies, Tardif *et al.* (2009; 2010) investigated the impact of different acquisition protocols on VBM results. In particular, three MRI sequences—the ‘fast low-angle shot’ technique, FLASH, (Frahm et al., 1986); ‘magnetization-prepared rapid gradient echo’ imaging, MP-RAGE, (Mugler and Brookeman, 1990; Mugler et al., 1992) and the ‘modified driven equilibrium Fourier transform’ approach, MDEFT, (Lee et al., 1995)—were compared at 3 T and 1.5 T. Each protocol yielded a distinct regional sensitivity pattern to morphometric gray-matter density (GMD) changes. Results from power analyses showed that MP-RAGE required more subjects than FLASH to detect GMD changes but offered higher CNR and improved tissue classification. The MDEFT protocol, which is currently used only in research settings, yielded the highest CNR and the smallest GMD variability. A limitation of both studies was the small number of subjects (≤ 9). Similarly, Helms et al. (2009) suggested by means of VBM that the segmentation of deep gray-matter (GM) structures is improved when using acquisition protocols that allow the computation of magnetization-transfer maps compared to optimized T_1-weighted MRI protocols. While in those former studies paired *t*-tests showed the effect of mixing two different imaging parameters into one VBM analysis, this analysis does not provide direct information on altered detectability of structural brain changes due to the variation of the parameters. In principle, such changes can be assessed by statistical interaction analysis of two experimental factors, where one of the factors is a well-established structural process. Note, however, that the VBM analysis is only an indirect assessment of brain structure as it interprets GMD measures, which are estimated using *a-priori* template and model information.

To expand the scope of previous findings, the objective of the current work was to evaluate the impact of acquisition parameters in detecting age-related structural brain changes causing atrophy and reduction in the GMD. Previous research showed GMD changes across the whole cortex (Good et al., 2001b), which provides excellent conditions to study distinct sensitivity profiles of different imaging parameters employing interaction analyses. Besides interaction tests, paired *t*-tests were utilized to detect artificially introduced (i.e., false positive) GMD changes due to variation of acquisition parameters.

Following similar motivation as discussed by Tardif *et al.* (2009, 2010), the MP-RAGE technique was employed as one of the most popular anatomical sequences in morphometric studies. Due to a ubiquitous availability, high GM/white matter (WM) contrast, and relatively short scan times, the MP-RAGE sequence has been frequently used in investigations of neurodegenerative diseases (Camicioli et al., 2009; Feldmann et al., 2008) including multicenter trials of the Alzheimer's Disease Neuroimaging Initiative (ADNI) (Jack et al., 2008; Mueller et al., 2005). Briefly, MP-RAGE consists of an initial preparation of the magnetization by an adiabatic inversion pulse, followed by a relaxation delay (inversion time, TI) and a segmented acquisition period employing a snapshot FLASH sequence (Haase, 1990). Typically, the FLASH readout steps through the entire partition-encoding loop during each segment (i.e., during each repetition time, TR, of the inversion pulse), and the phase-encoding gradient is incremented from segment to segment (i.e., with every TR) (Deichmann et al., 2000; Mugler and Brookeman, 1990; Mugler et al., 1992).

Additional imaging with the recently published ‘magnetization-prepared 2 rapid gradient echoes’ sequence, MP2RAGE, (Marques et al., 2010) was included for a comparison of acquisition techniques. It is a variation of the MP-RAGE sequence, in which two FLASH readouts are quasi-simultaneously acquired at different TI after each inversion. The images can be combined by computing the product of the (complex) signal intensities divided by the sum of the squared intensities to obtain so-called 'uniform images‘ with T_1 contrast, which are largely free of both the radiofrequency (RF) reception bias field and RF transmit-field inhomogeneity. Although the SNR might be reduced on the ‘uniform images’ due to noise propagation, contrast is improved as unwanted proton-density contrast and residual T_2* contrast is removed by the image combination as well. We thus hypothesize that MP2RAGE offers potential advantages of *(i)* an intrinsic bias-field correction based on a well-defined physical concept of signal generation rather than *a-priori* assumptions on spatial modulation and smoothness of image intensities as currently employed in VBM (Ashburner and Friston, 2005) and *(ii)* improved contrast between GM, WM, and cerebro-spinal fluid (CSF) that might lead to better tissue classification and segmentation results.

For further comparisons, acquisitions were performed with both a 12-channel and a 32-channel coil to study the influence of imaging hardware, and with two different voxel dimensions to study the effect of image resolution and/or interpolation.

4.2. Subjects and Methods

4.2.1. Subjects

Thirty-six healthy Caucasian adults grouped into 12 young (6 female, mean age plus/minus one standard deviation: 22.3 ± 1.1 years), 12 middle-aged (6 female, 46.6 ± 1.4 years), and 12 elderly subjects (6 female, 71.8 ± 1.9 years) participated in the study, each lasting approximately 60 min. All participants gave written consent after being informed about the possible risks and discomforts of the experimental procedure. Subjects also completed a health history questionnaire to assess their suitability for undergoing MRI scanning. Exclusion criteria comprised known contraindications to MRI, a history of neuropsychiatric diseases, and abnormalities on T_1-weighted and on 'fluid-attenuated inversion recovery' (FLAIR) (Hajnal et al., 1992) head scans (both acquired in preceding scanning session). Acquisition protocols (Table 4.1) were pseudo-randomized across subjects to avoid any systematic confound.

4.2.2. Imaging Protocol

All acquisitions were performed at 3 T on a single MAGNETOM Verio scanner (Siemens, Erlangen, Germany). The body coil was used for transmission, and two commercial head coil arrays, a 12-channel matrix coil and a 32-channel array were used for signal reception. The inner diameter of the 32-channel coil is approximately 3–5 cm smaller than that of the 12-channel coil and fits the subject's head as a helmet. A total of six different T_1-weighted 3D data sets were acquired from each subject per session. In particular, data with nominal voxel size of $1\times1\times1$ mm³ were acquired with both RF coils and with both MP-RAGE and MP2RAGE (Table 4.1; protocols 1, 2, 4, and 5). Additionally, data sets with nominal voxel size of $0.8\times0.8\times0.8$ mm³ were acquired with the 32-channel array and with MP-RAGE and MP2RAGE (Table 4.1; protocols 3 and 6).

Prot.	Rx coil	n_x	n_y	n_z	FOV [mm²]	Δz [mm]	TR [s]	TI [s]	TE [ms]	α [°]	BW [Hz/pixel]	AF	TA [min:s]
MP-RAGE (sagittal orientation, anterior/posterior phase-encoding direction)													
1	12ch	256	240	176	256×240	1.0	2.3	0.9	3	9	240	1	9:14
2	32ch	256	240	176	256×240	1.0	2.3	0.9	3	9	240	1	9:14
3	32ch	320	280[a]	220	256×224	0.8	2.3	0.9	3	9	240	1	9:25
MP2RAGE (sagittal orientation, anterior/posterior phase-encoding direction)													
4	12ch	256	256	176	256×256	1.0	5.0	0.7 2.5		4/5	240	3	9:12
5	32ch	256	256	176	256×256	1.0	5.0	0.7 2.5		4/5	240	3	9:12
6	32ch	320	320	220[b]	256×256	0.8	5.0	0.7 2.5		4/5	240	3	9:32

Table 4.1: Acquisition parameters used to investigate the impact of the imaging protocol on VBM results.

Abbreviations and symbols: 12ch = 12-channel matrix coil; 32ch = 32-channel array coil; AF = GRAPPA acceleration factor; BW = receiver bandwidth; FOV = field of view; n_x, n_y, n_z = k-space matrix size along read-, phase-, and slice-direction; Rx = receiver; TA = acquisition time; TI = inversion time; TR = repetition time for the inversion pulse; α = RF pulse flip angle of the FLASH readout; Δz = slice thickness. [a] Acquired with 7/8 partial-Fourier encoding. [b] Acquired with 79% slice resolution.

Except for the image resolution, acquisition parameters used with MP-RAGE and MP2RAGE were consistent with those employed in the ADNI study (Jack et al., 2008) and by Marques et al. (2010), respectively. The 3D data sets stored from each MP2RAGE experiment included two series of inversion-contrast image volumes acquired at the two inversion times, TI_1 and TI_2, and the computed ‘uniform images’.

4.2.3. Pre-Processing

Initial pre-processing of MP2RAGE data included a masking step to eliminate the background noise on the computed 'uniform images' to ensure optimal performance of the VBM algorithms. In both inversion-contrast image volumes, voxel values less than 10% of the maximum signal were set to zero. Both image volumes were then combined using a logic OR-operator and binarized to obtain a brain mask. Subsequently, hole filling was applied to the binarized mask using a morphological filter as it is offered in Matlab 7.11.0 (R2010b, MathWorks, Natick, MA). Finally, the T_1-weighted 'uniform image' data were multiplied with the binary mask. Both MP-RAGE and pre-processed MP2RAGE image volumes were then segmented with the native segmentation algorithm implemented in SPM8 ("segment" function) using default parameters (Wellcome Trust Centre for Neuroimaging, UCL, London, UK). Additionally, MP2RAGE volumes were also segmented using four Gaussians to model the signal intensity distribution for the CSF tissue class instead of the default value of two Gaussians (note that all of the following results were obtained with default settings unless specifically indicated otherwise). The implemented bias-field correction was only applied to the MP-RAGE data, whereas the MP2RAGE data (as they were based on the 'uniform images' that are largely free of spatial intensity inhomogeneities) were segmented without further bias-field correction. To assess the influence of different image resolutions, all 3D data were up-sampled to an isotropic nominal voxel size of 0.8 mm. Segments were normalized towards a group-specific GMD template employing the 'diffeomorphic anatomical registration using exponentiated Lie algebra' (DARTEL) algorithm with SPM8 (Ashburner, 2007). Subsequently, GM segments were modulated and isotropically smoothed using a Gaussian kernel of 8-mm full width at half maximum.

Whole-brain signal-intensity histograms for were computed from the bias-field-corrected MP-RAGE images and the MP2RAGE 'uniform images' (Shimazaki and Shinomoto, 2007). Signal intensities of MP2RAGE images were normalized to 4095.

Intensities of MP-RAGE images were normalized using five times the standard deviation of the signal values to exclude outliers.

4.2.4. Statistical Analysis

All statistical assessments were performed with thresholded GM images excluding voxels with a GM probability density less than 10%. Statistical assessments included two-sample *t*-tests of the main effect of aging between young, middle-aged, and elderly subjects with a flexible factorial design using total intracranial volume (TIV) as a covariate to control for different brain sizes between subjects. Paired *t*-tests comparing different acquisition strategies, for example 1×1×1 mm^3 MP-RAGE image volumes acquired with either the 12-channel coil or the 32-channel coil, were performed using a flexible factorial design to investigate the effect of mixing different acquisition parameters into a VBM analysis. These assessments did not include TIV as covariate. For additional investigation of the impact of a specific acquisition parameter in revealing aging effects, interactions of “age/coil”, “age/sequence”, and “age/resolution” were computed using the same flexible factorial design as above. Overall, interaction tests were computed from 72 datasets—two factors for each level “coil”, “sequence”, and “resolution” times three groups (“young”, “middle-aged”, “elderly”) times 12 subjects per group (i.e., 33 degrees of freedom resulting from 36 subjects plus factors “group” and “acquisition parameter”). Non-stationary cluster-extent corrections were applied to all VBM results (Hayasaka et al., 2004; Worsley et al., 1999).

All subsequently presented statistical results refer to data, which were processed using an interpolated isotropic voxel size of 0.8 mm. The figures show color-coded clusters with *t*-values within the range of −15 to +15, which remained significant after voxel-wise thresholding at $p < 0.001$ and after family-wise error (FWE) correction on cluster-level with a threshold of $p < 0.05$.

4.2.5. SNR Analysis

To obtain SNR estimates, the individual GM, WM, and CSF segments were thresholded at 50% and served as masks to extract image intensities. Anatomical regions of interest were extracted using three different atlases for the specific tissue types, provided by the FMRIB Software Library (FSL) (Mazziotta et al., 2001; Wakana et al., 2007) and the Harvard-Oxford cortical and subcortical structural atlas. For an estimate of the noise, a cube of 10×10×10 voxels was selected in an artifact-free background region. Signal-to-noise ratios of the MP-RAGE image volumes were computed from the mean signal value of a brain structure divided by the standard deviation of the noise. Approximate SNR of MP2RAGE image volumes were estimated with Equation 1 from Marques et al. (2010) and error propagation. In particular, signal values were obtained from the 'uniform images' whereas estimates of the noise were obtained from the inversion-contrast images recorded at TI_1 and TI_2. A constant factor of 1/0.655 (Henkelman, 1985) was considered to account for the Rician noise distribution of the inversion-contrast images (magnitude images) as the error propagation was based on the assumption of Gaussian-distributed white noise.

4.3. Results

Exemplary axial sections of T_1-weighted images acquired with the six different protocols (cf. Table 4.1) are presented in Figure 4.1. Qualitatively, the MP-RAGE images provided less homogeneous signal intensities within a tissue type. The intracranial volume appeared better separated from *dura mater* in the MP2RAGE images. With this modality, the deep GM structures were observed with improved contrast from the surrounding WM and ventricular CSF.

Typical examples of normalized signal-intensity histograms are shown in Figure 4.2. The peak positions obtained with the 12-channel coil did not significantly vary from those obtained with the 32-channel coil. However, there was a consistent trend of sharper peaks for the 32-channel coil, which is likely a result from an improved SNR. Remarkably, the distributions of signal attributed to CSF were distinct between histograms obtained with different pulse sequences with maxima at 0.17 and 0.11 for MP-RAGE and 0.04 and 0.02 for MP2RAGE in the young and elderly subject,

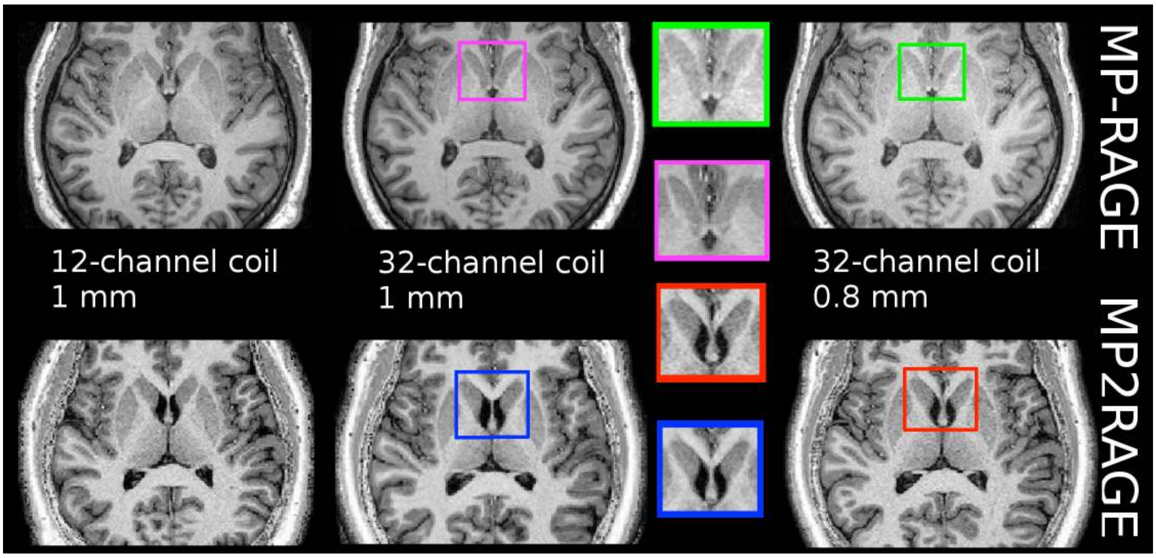

Figure 4.1: Examples of T_1-weighted axial brain sections through the striatum from the different 3D image acquisition procedures (cf. Table 4.1; top row: protocols 1-3, bottom row: protocols 4-6).

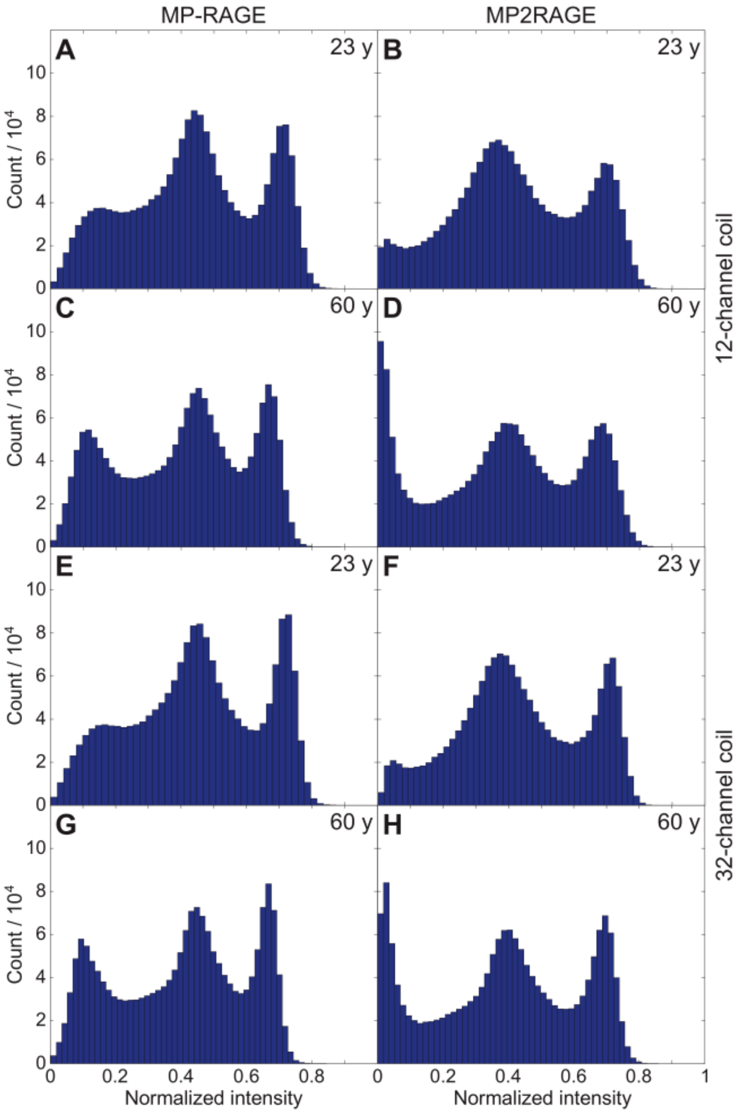

Figure 4.2: Normalized signal-intensity histograms recorded in a young **(A,B,E,F)** and an elderly **(C,D,G,H)** male subject (23 and 60 years) with the 12-channel **(A–D)** and the 32-channel coil **(E–H)** using the MP-RAGE **(A,C,E,G)** and the MP2RAGE sequence **(B,D,F,H)**. Histograms recorded in middle-aged subjects were similar to those from young subjects (data not shown). Peaks at approximately 0–0.2, 0.4, and 0.7 are assigned to voxels in CSF, GM, and WM, respectively.

respectively. The CSF peak had a positive skew, especially in the elderly subject, for MP2RAGE scans but not for MP-RAGE scans. The shift of the maxima towards minimal normalized signal values for MP2RAGE is explained by including one image volume recorded approximately at the CSF nulling time (TI_2 = 2.5 s) in the calculation of the 'uniform image' (Marques et al., 2010). With MP2RAGE, both the distance between the CSF and GM peak (0.33 and 0.37 in young and elderly, respectively) and the distance between the GM and WM peak (0.34 and 0.30 in young and elderly, respectively) were larger than in the MP-RAGE histograms (0.28 and 0.34 for CSF/GM and 0.28 and 0.21 for GM/WM in young and elderly, respectively).

Compared to the young subject, the distance between the peaks from CSF and GM increased concomitantly with a marked increase of the relative CSF peak area in the elderly subject with both pulse sequences, which is consistent with the assumption of enlarged CSF spaces due to brain atrophy and, hence, reduced partial volume-effects in the sulci.

Table 4.2 shows mean SNR values obtained with the different acquisition procedures in various brain regions. Remarkably, the SNR obtained with MP2RAGE was approximately 15% lower than with MP-RAGE in cortical areas, regardless of the coil or resolution. This is also underpinned by Figure 4.1 demonstrating an increased noise level in MP2RAGE images acquired with the 12-channel coil. In subcortical areas, both sequences yielded very similar results, whereas in WM, a higher SNR was found with MP2RAGE. Finally, all SNR values increased for the 32-channel coil in comparison to the 12-channel data.

	Cortical GM				Subcortical GM		WM	CSF
	Fro.	Tem.	Par.	Occ.	Put.	Tha.	Corpus callosum	Ventricle
					MP-RAGE			
12ch, 1 mm	35 ±5	48 ±7	38 ±6	45 ±7	61 ±9	56 ±10	65 ±11	19 ± 5
32ch, 1 mm	55 ±16	78 ±23	61±17	72 ±22	94 ±28	85 ±28	100 ±31	30 ± 11
32ch, 0.8 mm	49 ±13	67 ±18	53 ±14	62 ±17	80 ±21	73 ±21	82 ±22	31±10
					MP2RAGE			
12ch, 1 mm	27 ±4	44 ±6	33 ±5	40 ±9	65 ±9	56 ±11	74 ±12	18 ±6
32ch, 1 mm	44 ±9	70 ±19	52 ±19	64±13	96 ±18	82 ±20	112 ±25	24 ±6
32ch, 0.8 mm	33 ±6	53 ±9	39 ±7	48 ±8	72 ±12	63 ±14	84 ±16	23 ±5

Table 4.2: Signal-to-noise ratios (mean plus/minus standard deviation; averages over all subjects) for each imaging modality in different anatomical stuctures.
Abbreviations: 12ch = 12-channel matrix coil; 32ch = 32-channel array coil; CSF = cerebro-spinal fluid; Fro. = frontal, GM = gray matter; MP = MP-RAGE; MP2 = MP2RAGE; Occ. occipital; Par. = parietal; Put. = putamen; Tha. = thalamus; Tem. = temporal; WM = white matter.

Figure 4.3 presents comparisons of VBM segmentation results obtained with MP-RAGE and MP2RAGE (same subjects as in Fig. 4.2). Segmentation differences were most prominent in acquisitions with the 12-channel coil, whereas more consistent segmentations were obtained with the 32-channel coil. In particular, the area of GMD values above threshold was markedly expanded towards the GM/WM border on MP-RAGE-based segments (indicated by blue colors) and slightly expanded towards the pial surface on MP2RAGE images (indicated by red colors). In addition, an enlarged region of GMD values above threshold was found in deep GM structures with MP2RAGE in all subjects and with both RF coils.

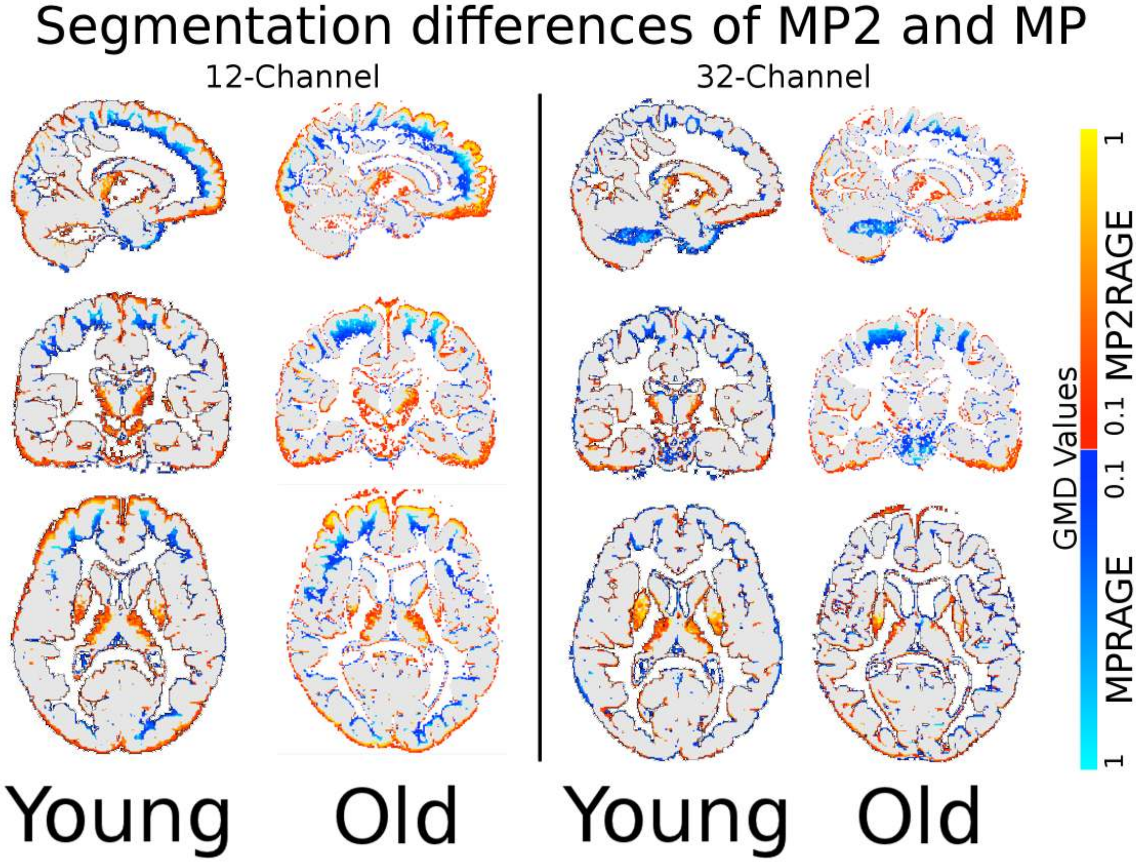

Figure 4.3: Examples of GM segmentations thresholded at GMD = 0.1 from a young **(A,C)** and an elderly **(B,D)** male subject (same as in Fig. 4.2) in experiments performed with the 12-channel **(A,B)** and the 32-channel coil **(C,D)**. Blue colors indicate voxels where GMD > 0.1 was obtained only with MP-RAGE whereas red colors indicate voxels where GMD > 0.1 was obtained only with MP2RAGE. Gray indicates overlap, that is voxels where GMD > 0.1 was simultaneously obtained with both sequences. Results from middle-aged subjects were similar to those from young subjects (data not shown).

The main effect of aging between young and elderly subjects demonstrated widespread GMD changes in cortical and subcortical areas for all acquisition parameters. This result is in line with the literature (Good et al., 2001b). Comparisons of young and middle-aged subjects or middle-aged and elderly subjects were also computed and yielded consistent, however more subtle, effects (images not shown). Figure 4.4 shows the aging effect for acquisitions with the MP-RAGE sequence using the 12- or 32-channel coil. Figure 4.5 presents complementary results for the MP2RAGE sequence, which are less pronounced. The same analysis was repeated with a slightly modified

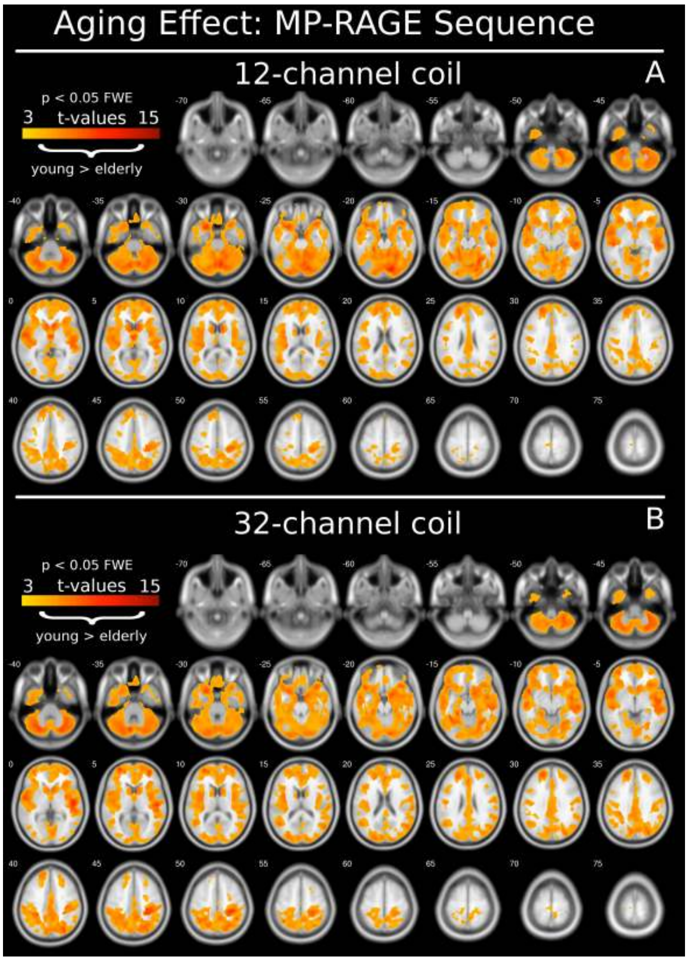

Figure 4.4: Two sample *t*-test results ($p < 0.05$ FWE) showing the main effect of aging in acquisitions with the MP-RAGE sequence (1×1×1 mm³) and **(A)** the 12-channel coil, **(B)** the 32-channel coil. Red color scales indicate higher GMD in young compared to elderly subjects.

segmentation (i.e., using 4 Gaussians for the CSF tissue class instead of default settings) to investigate if the pronounced positive skew of the CSF signal intensity distribution obtained with MP2RAGE might impact the VBM results. With the 12-channel coil, the detection of aging effects widely increased in cortical areas (Fig. 6A) yielding more consistency with the result obtained with MP-RAGE and default settings (Fig. 4A). A subtle tendency of a more pronounced aging effect was also found in MP2RAGE acquisitions with the 32-channel coil, however, the results from both segmentations (4 Gaussians vs. default settings) were very similar in this case (images not shown).

Figure 4.7 presents paired *t*-test results for the comparison of images acquired in the same subject with different RF coils. MP-RAGE and MP2RAGE data were evaluated separately. Table 4.3 shows the averaged differences of GMD estimates and the percentage of affected voxels in relation to the whole brain. Significant effects indicating different GMD estimates from acquisitions with different RF coils were obtained with MP-RAGE in widespread cortical and subcortical regions, for example in the frontal lobe, cingulate cortex, lingual gyrus, hippocampus, and cerebellum. MP-RAGE-based GMD values estimated from acquisitions with the 32-channel coil exceeded those obtained with the 12-channel coil, whereas the opposite effect was observed for the right temporal superior gyrus, occipital lobe, and putamen (Fig. 4.7A). Reverse results appeared in acquisitions with MP2RAGE (Fig. 4.7B) yielding higher GMD in the right putamen and pons for the 32-channel coil and higher GMD in widespread cortical areas, for example frontal, temporal, and occipital regions for the 12-channel coil (Table 4.3).

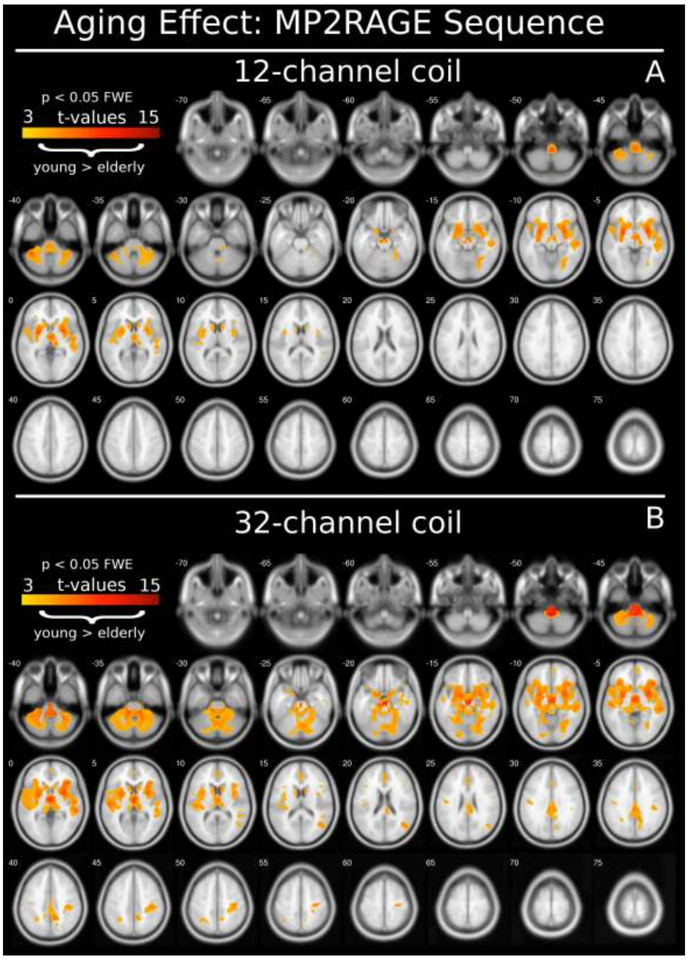

Figure 4.5: Two sample *t*-test results ($p < 0.05$ FWE) showing the main effect of aging in acquisitions with the MP2RAGE sequence (1×1×1 mm^3) and **(A)** the 12-channel coil, **(B)** the 32-channel coil. Red color scales indicate higher GMD in young compared to elderly subjects.

Paired *t*-test results for the comparison of images acquired in the same subject with different pulse sequences are presented in Figure 4.8 and Table 4.3. The two RF coils were evaluated separately. MP2RAGE yielded higher GMD estimates in widespread cortical and subcortical regions with a tendency towards the ventral direction (e.g., orbitofrontal cortex, lingual cortex, temporal inferior gyrus, putamen, caudate nucleus, thalamus, and cerebellum) with the 12-channel coil (Fig. 4.8A), whereas the MP-RAGE sequence yielded higher GMD estimates in the post- and

Parameter	Difference in GMD estimate	Affected brain volume	Difference in GMD estimate	Affected brain volume
‘coil’	MP-RAGE		MP2RAGE	
‘12ch’ > ‘32ch’	2.9%	2.4%	2.8%	25.1%
‘12ch’ < ‘32ch’	4.3%	59.5%	2.4%	1.6%
‘sequence’	12-channel coil		32-channel coil	
‘MP2’ > ‘MP’	7.7%	64.9%	7.5%	23.4%
‘MP2’ < ‘MP’	7.3%	3.4%	5.4%	17.4%
‘resolution’	MP-RAGE		MP2RAGE	
‘1mm’ > ‘0.8mm’	3.3%	16.8%	2.6%	13.1%
‘1mm’ < ‘0.8mm’	2.7%	16.4%	1.5%	0.5%

Table 4.3: Gray-matter-density estimates extracted from significant regions and extensions of the significant regions (in percent of total brain volume) derived from the paired *t*-test with parameters ‘coil’, ‘sequence’, and ‘resolution’ as shown in Figures 4.6–4.8.

precentral gyrus. Figure 4.8B shows the same comparison for the 32-channel coil. The results are comparable but less pronounced for the MP2RAGE and enhanced for the MP-RAGE sequence.

Figure 4.9 finally summarizes results of the paired *t*-test between data acquired in the same subject with different voxel sizes. MP-RAGE and MP2RAGE images (all acquired with 32-channel coil) were evaluated separately. Figure 4.9A presents results for the MP-RAGE sequence with higher GMD estimates in the lingual cortex, right fusiform gyrus, hippocampus, putamen, caudate nucleus, and thalamus on images acquired at 1-mm nominal resolution. Images acquired at 0.8-mm nominal resolution yielded higher GMD estimates in parietal cortex and parts of the cerebellum in the MP-RAGE. Both resolutions yielded similar numbers of affected voxels, but GMD differences were more pronounced for the 1-mm nominal resolution (Table 4.3). Figure 9B presents

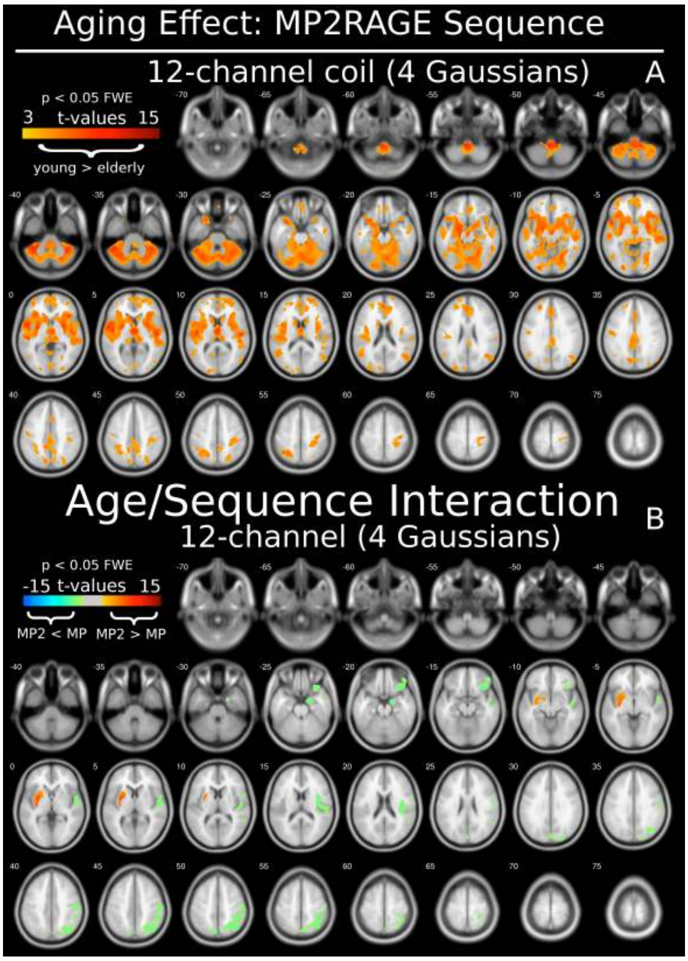

Figure 4.6: **(A)** Two-sample *t*-test results ($p < 0.05$ FWE) showing the main effect of aging in acquisitions with the MP2RAGE sequence (1×1×1 mm³) and the 12-channel coil when segmention was performed with four Gaussians for the CSF tissue class. Red color scales indicate higher GMD in young compared to elderly subjects. **(B)** Interaction effect of age and imaging sequence (MP-RAGE vs. MP2RAGE; 1×1×1 mm³; $p < 0.05$ FWE) in acquisitions with the 12-channel coil. MP2RAGE images were segmented using four Gaussians for the CSF tissue class. Blue and red color scales indicate higher sensitivity for detecting aging effects with MP-RAGE and with the MP2RAGE, respectively. Note that MP-RAGE is abbreviated as 'MP' and MP2RAGE is abbreviated as 'MP2'.

results for the MP2RAGE sequence with higher GMD estimates in the orbitofrontal cortex, fusiform gyrus, amygdala, putamen, caudate nucleus, and thalamus on images acquired with 1-mm nominal resolution, whereas only minor areas were found with significantly higher GMD estimates on MP2RAGE images acquired with 0.8-mm voxels compared to 1-mm voxels (Table 4.3).

Rather subtle interaction effects of age and RF coil are shown for MP-RAGE and for MP2RAGE in Figure 4.10A and 4.10B, respectively. With MP-RAGE, increased sensitivity in detecting aging effects was found in the right hippocampus with the 32-channel coil. With MP2RAGE, more widespread sensitivity increases in detecting aging effects were found with the 32-channel coil including areas of the insula, putamen, thalamus, midbrain, and brainstem.

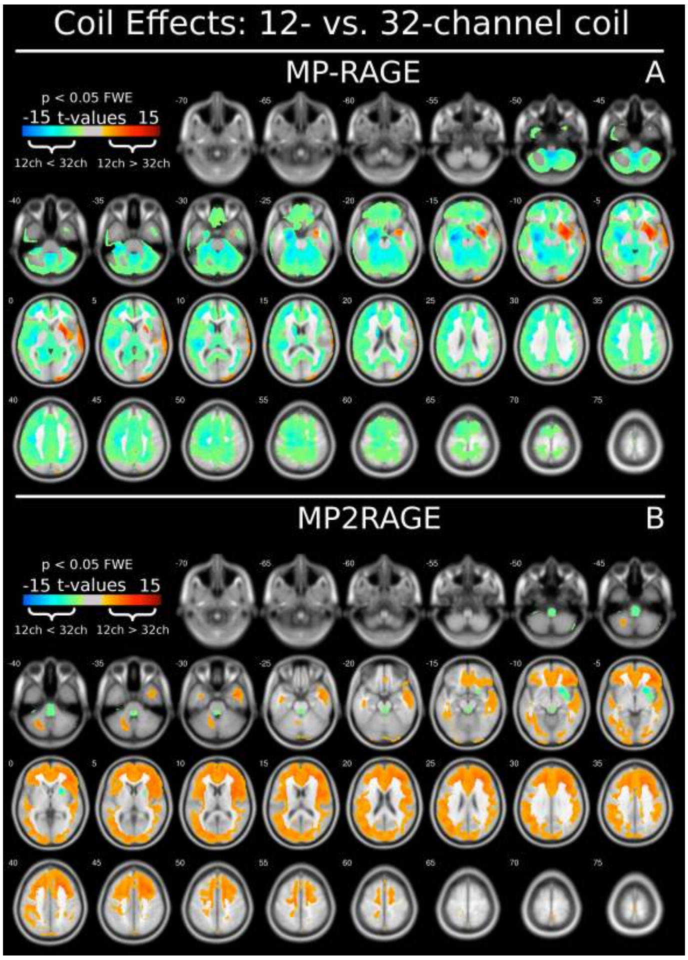

Figure 4.7: Paired *t*-test results ($p < 0.05$ FWE) showing the influence of the RF coil (12-channel coil vs. 32-channel coil; 1×1×1 mm³) in acquisitions with **(A)** MP-RAGE and **(B)** MP2RAGE. Blue and red color scales indicate higher GMD obtained with the 32-channel and with the 12-channel coil, respectively.

Figure 4.10 presents the interaction between age and MRI sequence. Areas with more pronounced aging effects obtained with MP-RAGE included lingual, hippocampal, parahippocampal, caudate, and cerebellar regions in data acquired with the 12-channel coil (Fig. 4.11A). Differences in the interaction between age and MRI sequence were reduced in scans with the 32-channel coil to the left postcentral gyrus (Fig. 4.11B). More pronounced aging effects were obtained with MP2RAGE and the 12-channel coil in the left putamen. Additional interaction tests were also performed with modified segmentation (4 Gaussians for the CSF tissue class) of MP2RAGE images. Differences between MP-RAGE and MP2RAGE were considerably diminished in the 12-channel coil acquisitions (Fig. 4.6B), whereas results for the 32-channel coil acquisitions were largely consistent with those obtained with default settings (images not shown).

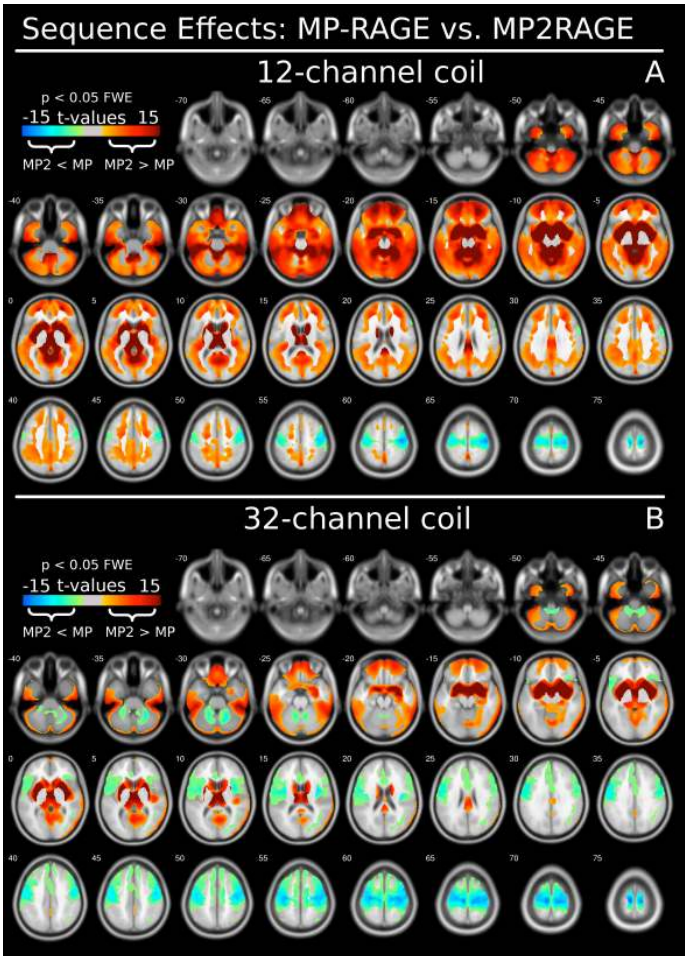

Figure 4.8: Paired *t*-test results ($p < 0.05$ FWE) showing the influence of the imaging sequence (MP-RAGE vs. MP2RAGE; 1×1×1 mm³) in acquisitions with **(A)** the 12-channel coil and **(B)** the 32-channel coil. Blue and red color scales indicate lower and higher GMD estimates obtained with MP-RAGE and with MP2RAGE, respectively. Note that MP-RAGE is abbreviated as 'MP' and MP2RAGE is abbreviated as 'MP2'.

The interaction effect of age and resolution is presented in Figure 4.12. It shows very subtle sensitivity increases for detecting aging effects with 1-mm nominal resolution in the left putamen for MP-RAGE and in the brainstem for MP2RAGE.

,

4.4. Discussion

In the current study, aging effects served as a paradigm to investigate the impact of the MRI acquisition protocol on GMD estimates obtained with VBM (SPM8/DARTEL and default parameters). In particular influences from different RF coils, imaging sequences, and image resolutions were statistically assessed by two-sample *t*-tests of the main effect of aging, paired *t*-tests of different acquisition parameters, and interaction tests of age and acquisition parameters.

The paired *t*-tests comparing two data sets acquired from the same subject provide information on the rate of artificial (i.e., false positive) GMD differences, as the

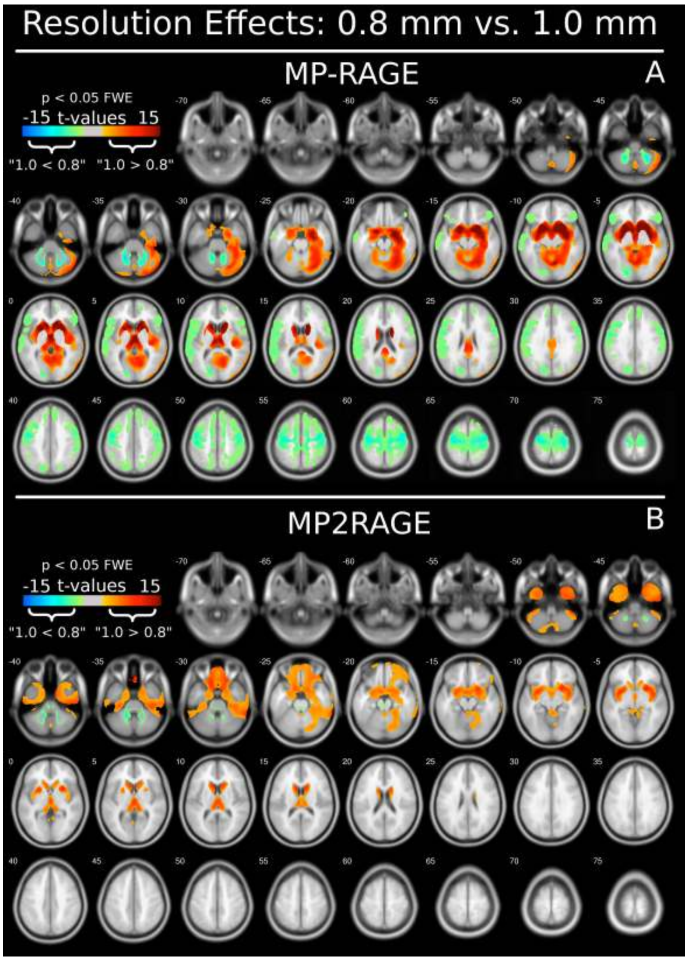

Figure 4.9: Paired *t*-test results ($p < 0.05$ FWE) showing the influence of image resolution (nominal isotropic voxel size of 1 mm vs. 0.8 mm; 32-channel coil) in acquisitions with **(A)** MP-RAGE and **(B)** MP2RAGE. Blue and red color scales indicate higher GMD estimates obtained with nominal isotropic voxel sizes of 0.8 and 1 mm, respectively.

brain tissue properties affecting the MRI signal can be assumed to be invariant during a single scanning session. That is, these tests reveal information on the systematic bias induced by including images with inconsistent acquisitions in VBM analyses. Overall, substantial effects were observed for all combinations of parameters (Figs. 4.7–4-9). Hence, careful definition and standardization of the imaging procedure is strongly advocated. If some variation in image acquisition cannot be avoided, for example in multi-centric studies, different groups (e.g., patients and control subjects) should be studied in a balanced fashion to avoid systematical bias in the statistical analysis, consistent with previous recommendation (Krueger et al., 2012; Pell et al., 2006; Ridgway et al., 2008). In such cases, MP2RAGE seems slightly less prone to false positive results from combining data acquired with inconsistent hardware.

Figure 4.4 demonstrates the general suitability of the MP-RAGE sequence to study aging effects, in particular in cortical areas. In comparison to these results, *t*-

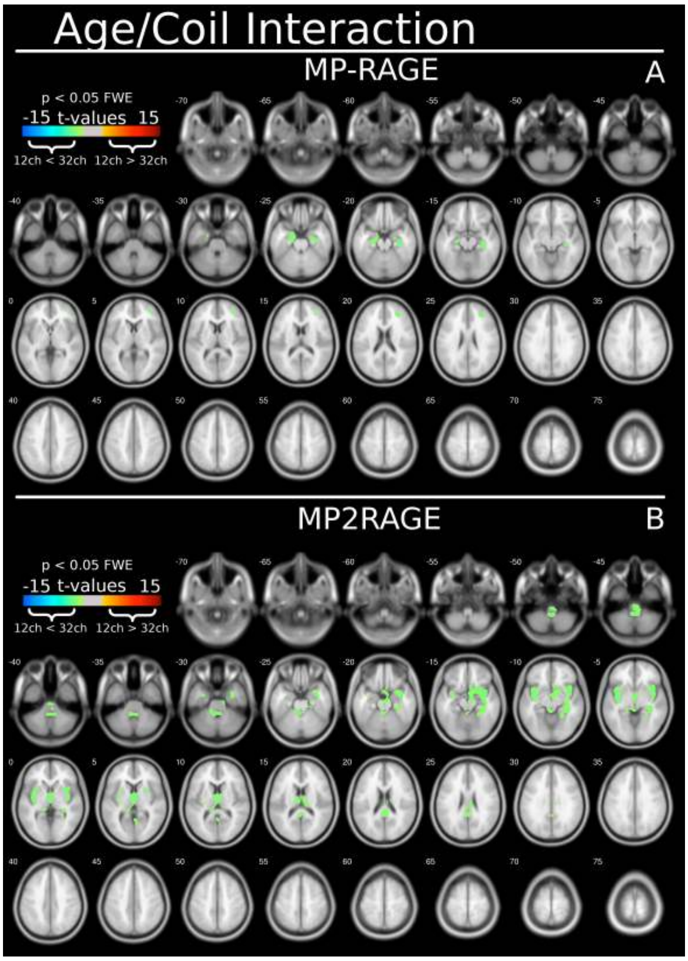

Figure 4.10: Interaction effect of age and RF coil (12-channel coil vs. 32-channel coil; 1×1×1 mm³; $p < 0.05$ FWE) in acquisitions with **(A)** MP-RAGE and **(B)** MP2RAGE. Blue and red color scales indicate higher sensitivity for detecting aging effects with the 32-channel and with the 12-channel coil, respectively.

values were reduced for MP2RAGE in acquisitions with the 12-channel coil and, albeit at lesser extent, with the 32-channel coil (Fig. 4.5). This is in line with Table 4.2 yielding higher SNR for MP-RAGE in cortical areas (but not in subcortical areas). It must be noted, however, that SNR estimates based on two separate ROIs as used here are prone to error in multichannel acquisitions. In particular, SNR values obtained by this method can be significantly overestimated (Dietrich et al., 2007), especially when employing parallel imaging, such as GRAPPA, which was used in the MP2RAGE scans. Thus, the data summarized in Table 4.2 should be regarded as rather rough estimates, and a comparison of both pulse sequences is limited because the confounding factors are inconsistent. Nevertheless, an SNR penalty is expected for MP2RAGE due to noise amplification upon calculating the ‘uniform images’ and from the requirement to use GRAPPA acceleration, in line with the results in Table 4.2.

The interaction results for the 12-channel coil (Fig. 4.11A) yielded significantly increased *t*-values in widespread cortical areas for the MP-RAGE sequence compared

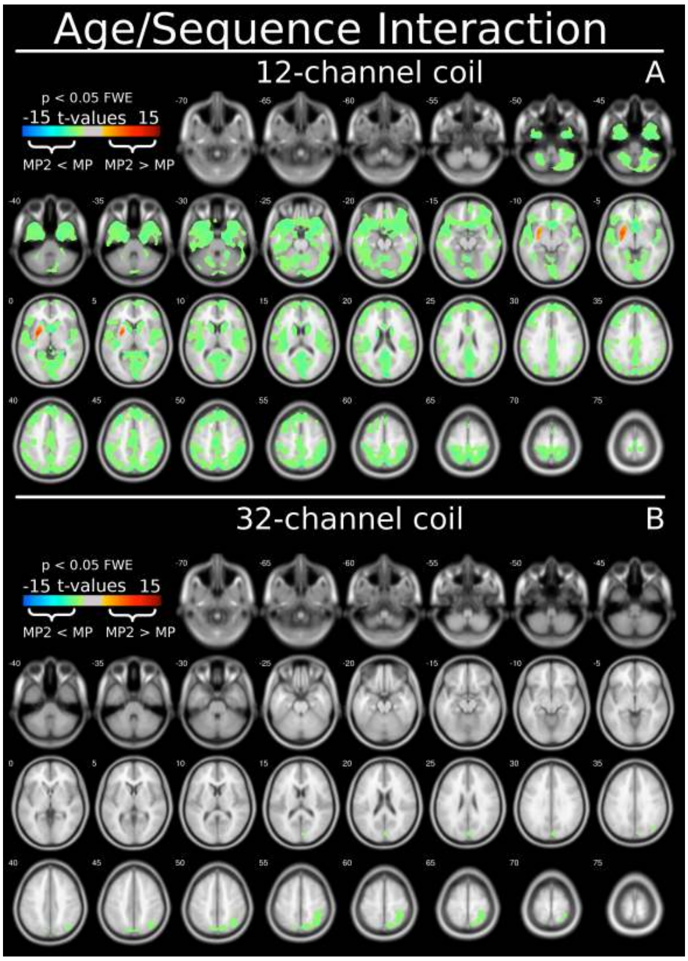

Figure 4.11. Interaction effect of age and imaging sequence (MP-RAGE vs. MP2RAGE; 1×1×1 mm³; p < 0.05 FWE) in acquisitions with (A) the 12-channel coil and (B) the 32-channel coil. Blue and red color scales indicate higher sensitivity for detecting aging effects with MP-RAGE and with the MP2RAGE, respectively. Note that MP-RAGE is abbreviated as 'MP' and MP2RAGE is abbreviated as 'MP2'.

to the MP2RAGE sequence (while the opposite effect was observed in deep GM, consistent with the SNR results). Such significant interaction might indicate improved performance of MP-RAGE over MP2RAGE in detecting GMD changes. However, it is also possible that this observation is confounded by false positive assignments. In particular, confounds can result from imperfect tissue classification if the rate of classification errors varies among groups. For example, segmenting the GM/CSF boundary is challenging (Hyde et al., 2012; Streitbürger et al., 2012), and tissue misclassification due to partial volume effects might be more prevalent in young subjects with sulci widths in the order or less than the voxel dimensions, whereas sulcal spaces are enlarged in elderly subjects. Thereby, estimated GMD differences might be artificially enhanced or diminished.

The comparison of segmentation results (Figs. 4.3A,B) demonstrates distinct differences between both sequence types, most notably for the 12-channel coil.

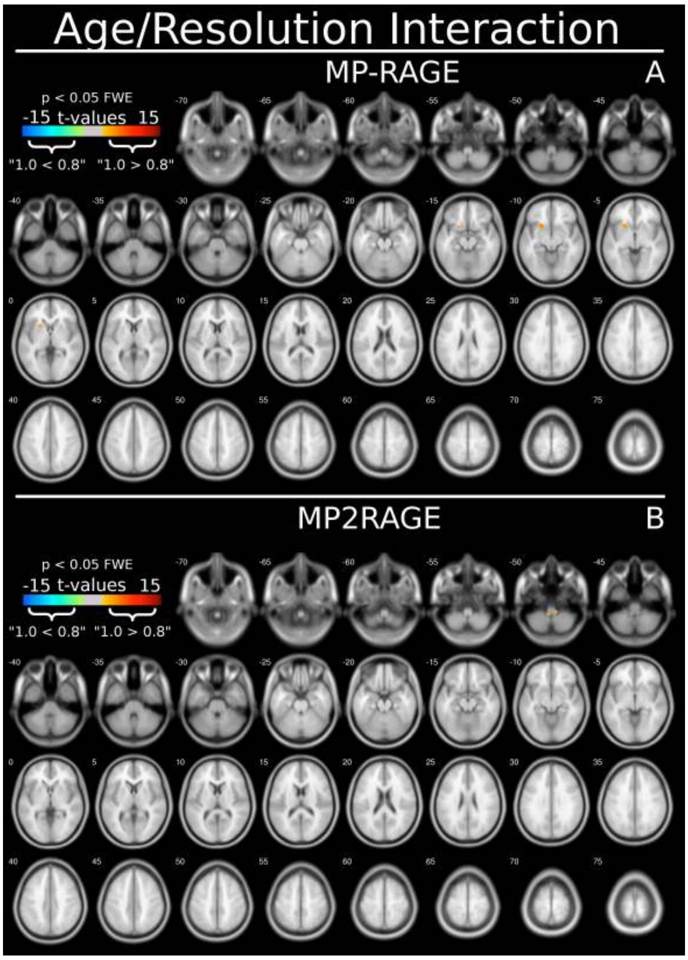

Figure 4.12: Interaction effect of age and image resolution (nominal isotropic voxel size of 1 mm vs. 0.8 mm; 32-channel coil; $p < 0.05$ FWE) in acquisitions with (A) MP-RAGE and (B) MP2RAGE. Blue and red color scales indicate higher sensitivity for detecting aging effects with nominal isotropic voxel sizes of 0.8 and 1 mm, respectively.

Especially the expanded area with GMD > 0.1 at the GM/WM border obtained with MP-RAGE is questionable due to anatomical considerations as it does not reproduce the cortical folding pattern. The signal-intensity histograms (Fig. 4.2) support the assumption of superior tissue classification achieved with MP2RAGE because the peak assigned to GM is better separated from both the CSF peak and the WM peak. This more efficient use of the dynamic range of signal intensities achieved with MP2RAGE results from combining two image volumes recorded at different inversion times, which permits to optimize the inversion-recovery contrast for GM/WM and for GM/CSF discrimination at the same time (Marques et al., 2010). However, the intrinsic segmentation advantages for MP2RAGE are partly offset by a reduced SNR, especially in acquisitions with the 12-channel coil (Table 4.2). With MP-RAGE, imperfections of the bias-field correction will additionally contribute to misclassification, which is largely avoided in the computation of ‘uniform images’ from MP2RAGE data. Support for the assumption of a bias in the GM segmentation and overestimation of the GM compartment on MP-RAGE images is finally obtained from recent work demonstrating significantly reduced cortical thickness estimates on high-resolution, presumably more accurate, 7T data in comparison to data acquired at 3 T with an 8-channel coil and parameters consistent with our protocol 1 (Lüsebrink et al., 2013).

Finally, our study used default settings in SPM8 to mimic typical applications of VBM. As these software settings were optimized for MP-RAGE data, it is possible that the use of modified tissue distribution functions might enhance the sensitivity of VBM analyses of MP2RAGE data. This assumption is supported by the results obtained with segmentations that considered a higher number of Gaussians (n = 4) to better account for the observed skew in the CSF signal intensity distribution in MP2RAGE images. With the modified segmentation, more widespread aging effects were detected in cortical areas (Fig. 6A) and age/sequence interaction effects were diminished (Fig. 6B). Hence, consistency between results obtained with the two MRI sequences increased upon modifying the segmentation settings for MP2RAGE.

Most of the age/sequence interaction effects evident in Fig. 4.11A became insignificant for acquisitions with the 32-channel coil (Fig. 4.11B). This is also consistent with better agreement of segmentation results among both pulse sequences for the 32-channel coil (Figs. 4.3C,D). In line with this observation is the only marginal effect achieved with the modified segmentation of the MP2RAGE data sets. Further information on the influence of the RF coil is obtained from the age/coil interaction (Fig. 4.10) indicating an advantage of the 32-channel coil to detect GMD changes with both sequences. It is consistent with the higher SNR offered by this coil (Table 4.2), which holds true even for the center of the brain (Wiggins et al., 2006). Better SNR should improve tissue classification and segmentation in the VBM processing pipeline. As the age/coil interaction was very subtle for MP-RAGE (Fig. 4.10A), we conclude that the potential advantage from using the narrower 32-channel coil (i.e., imposing more space restrictions) is less relevant for this sequence. The interaction effect was more pronounced for MP2RAGE (Fig. 4.10B). Use of the 32-channel coil increased the sensitivity, most notably for cortical structures, which is line with the literature on functional MRI (Kaza et al., 2011). To fully exploit the potential benefit from improved contrast and intrinsic bias-field correction offered by MP2RAGE thus requires that sufficient SNR is achieved. The different degree of age/coil interaction between MP-RAGE and MP2RAGE further indicates that a threshold exists in VBM analyses beyond which further SNR improvement becomes less relevant.

Figure 4.1 indicates that the higher nominal resolution leads to some benefit in separating anatomical structures. For example, the border separating the lateral ventricle and the caudate nucleus (color-framed zoomed images in Fig. 4.1) shows a distinct staircase pattern on images acquired with 1-mm nominal voxel size. This pattern is less pronounced on images acquired with 0.8-mm voxel size. However, images acquired with smaller voxels are also noisier (e.g., in the insula) consistent with the reduction of the voxel volume by 49%. Further assessment of these counteracting effects is obtained from the age/resolution interaction (Fig. 4.12) demonstrating a very subtle sensitivity advantage in isolated deep GM structures for the 1-mm isotropic voxel size. In our study, a predefined acquisition time of approximately 9:20 minutes was used in all scans. To benefit from improved segmentation accuracy due to decreasing the voxel size beyond 1×1×1 mm^3 at 3 T might thus require that the concomitant loss in SNR is at least partly addressed by prolonged scanning. We note that improved SNR at higher resolutions can also be obtained in acquisitions at higher field strength. Acquisitions at 7 T (or above) might thus show advantages for techniques that are penalized by suboptimal SNR at 3 T, such as scans at higher resolution or use of imaging strategies such as MP2RAGE.

4.5. Conclusion

While VBM permits non-invasive investigation of structural changes of the human brain *in vivo*, there is currently no gold standard available for verification of the obtained results. However, from consideration of our combined results we may speculate that the assessment of age-related GMD changes on MP-RAGE images can be biased towards false positive results while MP2RAGE might underestimate the degree of age-related GMD changes if SNR is relatively low and SPM8 default parameters are used in the processing pipeline. Both confounds are relaxed in acquisitions with the 32-channel coil. The improved SNR thus provides more flexibility in selecting a specific pulse sequence or acquisition parameters (e.g., image resolution). Although this work was limited to the assessment of aging effects, we expect that the results are also applicable to other investigations, for example, VBM studies of plasticity or neurodegenerative disorders.

5. General Discussion and Outlook

This work has shown that voxel-based methods and in particular VBM and TBSS, are sensitive methods for the detection of subtle structural brain changes. Another advantage is their applicability for different imaging modalities and scanning parameters. In the previous chapters, results of the VBM and TBSS analyses within the context of dehydration, blood serum biomarkers and aging have been discussed. The main purpose of those studies was to investigate the sensitivity of voxel-based methods to identify subtle structural brain changes and the identification of factors influencing the detection sensitivity. The investigations focused on GM and CSF in the T_1-weighted images, and on WM in the diffusion weighted images. In general, using recently available hard- and software in standard setups, the detection sensitivity of voxel-based methods is very high, but it can gain significantly by the use of optimal hard- and software parameters. This increase in detection sensitivity might lead to a concomitant increase of additional physiological noise in the image data. This confound interferes with the latter preprocessing and thus influence the statistical computations. Although, the present work addressed some of these issues, further investigations are necessary to achieve optimal scanning and preprocessing standards for voxel-based methods.

5.1. Sensitivity of Voxel-Based Methods

The sensitivity of voxel-based measures, and particularly the sensitivity of VBM for the detection of subtle morphological changes, has been addressed in the second and fourth chapter of this work. The first study has investigated and discussed the sensitivity of VBM in the context of dehydration and the accompanied enlargement of the ventricular system. It is important to note that VBM was not specifically designed to detect changes in cerebro-spinal fluid, but nonetheless has been successfully evaluated as a reliable measure by the study described above. In this study a ventricular enlargement of approximately 6% has been measured. This result underlines the high sensitivity of VBM for subtle brain changes as small as ~6%. In particular, hydration status should be considered as a confounding effect for, e.g. in longitudinal sport and medicine research, investigating brain plasticity changes in the vicinity of the ventricles. In those cases, it is highly recommended to consider subjects' hydration status, to avoid potential impurity of the results. Additionally, dehydration-related structural changes in the cortical layers might be detectable with VBM in a larger sample size.

In the fourth chapter a study investigating age-related structural brain changes with VBM is described. The interference of hardware and software parameters on VBM results has been examined with varying scanning parameters, within one hour of continuous scanning, on the same study subjects. The results underline the importance of consistent scanning parameters for each participant in VBM studies. It might be especially relevant for upcoming multicentric imaging studies where the best possible comparability between study centers is a major concern. Moreover, these results also emphasize the importance of image acquisition with high element coils whenever possible, to achieve optimal sensitivity and thereby reliable statistical results. The study also provides clear evidence for the relevance of well-chosen scanning sequences in respect to the sensitivity of standard VBM studies on whole brain GMD changes. The exemplary comparison of two different acquisition sequences in the aging paradigm showed a possible advantage of the MPRAGE sequence over the MP2RAGE sequence in default parameterized VBM studies. Therefore, this sequence can be recommended for future studies investigating whole brain GMD changes with default VBM parameters.

The third chapter described the sensitivity of TBSS and VBM in detecting associations between brain structure and peripheral blood serum markers. Recent literature already proposed the combination of biomarkers and MRI data in diseased subjects. In this project, healthy subjects' blood serum biomarkers and their correlations with WM and GM structures were investigated. Significant correlations with S100B were detected in the corpus callosum, as well as with NSE in the amygdala. This result underlines the applicability of TBSS and VBM for the correlation of peripheral blood serum proteins with imaging data. Furthermore, it represents its sensitivity to detect even normal non-pathological variations in healthy subjects. In particular, these results might be helpful for future studies, which investigate subjects suffering from e.g. major depression or schizophrenia, to integrate their results in the context of normal and healthy subjects and might help to understand mechanisms of changes in serum markers in the blood and their association in the brain.

5.2. Confounding Factors in Voxel-Based Methods

The increasing accuracy and sensitivity of soft- and hardware to detect brain changes might lead to false classification in segmentation or other preprocessing steps, originating from physiological or physical noise in the images. For example, the minor and subtle structural GM changes due to dehydration, which are described in chapter two of this work, give good evidence that dehydration probably has little impact on the analysis of neurodegenerative diseases. However, when VBM is employed in investigations focusing on brain tissue compartments, like WM or CSF, the subjects' hydration state can have quite an impact and it should therefore be considered as a possible confounding factor. Consequently, dehydration can be neglected in studies analyzing structural GM changes, whereas this does not hold true for studies investigating the ventricular system or white matter tracts. This study investigated the effect of hydration and dehydration on structural brain images. It can not be neglected that similar confounding factors, such as e.g. fat or blood vessels, might interfere with the acquired data, and consequently the statistical results. Additional possible physiological confounding factors and their impact on the analysis methods like VBM should be identified and evaluated in future studies.

The fourth chapter described several possible confounds and caveats in VBM analyses mixing different scanning parameters in a study. It was demonstrated that strict adherence to the study protocol is vital to ensure best comparability between participants. Interactions of structural brain changes with scanning parameters have been shown, which underlines the above advice to strictly follow one protocol for an entire study, to ensure high accuracy and reliability of the VBM results. In the present study, subjects were scanned in a longitudinal study design. Within one hour of continuous scanning different protocols were applied on each subject, this included changes in coil, resolution and sequence. In the following steps, MRI scans were analyzed with VBM to detect artificially induced plasticity changes due to the changed imaging parameters. With the assumption that the human brain structure stays almost constant within one hour, any significant difference between two consecutive scans can be considered as a false positive result originating from the changed scanning parameters. If not considered carefully, effects of different scanning parameters can easily be misinterpreted as massive GMD changes, which might indicate neurodegenerative diseases such as AD. In particular in multi-center studies, which often pool imaging data acquired with varying scanning hardware, careful selection of scanning parameters is necessary. Those studies might need to combine different scanning protocols to increase the sample size e.g. investigations of subjects with a rare type of neurodegenerative diseases. This combination of different scanning protocols is likely to simultaneously introduce systematic errors into the study design. It might lead to false-positively detected brain regions, misinterpreted as e.g. neurodegenerative brain atrophy. In summary, a careful selection of scanning parameters, screening of volunteers and acquired imaging data is indispensable for ensuring the best detection sensitivity and accuracy of voxel-based methods.

Zusammenfassung der Arbeit

Dissertation zur Erlangung des akademischen Grades Dr. rer. med.

Investigating Brain Structure Using Voxel-Based Methods with Magnetic Resonance Imaging

eingereicht von: Daniel-Paolo Streitbürger

angefertigt am: Max-Planck-Institut für Kognitions- und Neurowissenschaften, Leipzig

betreut von:

Prof. Dr. Dr. Matthias L. Schroeter

PD. Dr. Karsten Müller

April 2013

The number of people suffering from neurodegenerative diseases, such as Alzheimer`s disease, increased dramatically over the past centuries and is expected to increase even further within the next years. Based on predictions of the World Health Organization and Alzheimer`s Disease International, 115 million people will suffer from dementia by the year 2050. An additionally increase in other age related neurodegenerative diseases is also forecasted. Quite naturally, neurodegenerative diseases became a focus of attention of governments and health insurances, trying to control the uprising financial burden. Early detection and treatment of neurodegenerative

diseases could be an important component in containing this problem. In particular, researchers focused on automatic methods to analyze patients' imaging data. One way to detect structural changes in magnetic resonance images (MRI) is the voxel-based method approach. It was specifically implemented for various imaging modalities, e.g. T_1-weighted images or diffusion tensor imaging (DTI). Voxel-based morphometry (VBM), a method specifically designed to analyze T_1-weighted images, has become very popular over the last decade. Investigations using VBM revealed numerous structural brain changes related to, e.g. neurodegeneration, learning induced structural changes or aging. Although voxel-based methods are designed to be robust and reliable structural change detection methods, it is known that they can be influenced by physical and physiological factors. Dehydration, for example, can affect the volume of brain structures and possibly induce a confound in morphometric studies. Therefore, three-dimensional T_1-weighted images were acquired of six young and healthy subjects during different states of hydration. Measurements during normal hydration, hyperhydration, and dehydration made it possible to assess consequential volume changes in gray matter (GM), white matter (WM), and cerebrospinal fluid (CSF). The datasets were analyzed using VBM, FreeSurfer and SIENA. A significant decrease of GM and WM volume, associated with dehydration, was found in various brain regions. The most prominent effects were found in temporal and parietal areas, in the left inferior orbito-frontal region, and in the extra-nuclear region. Moreover, we found consistent increases in CSF, an expansion around 6% of the ventricular system affecting both lateral ventricles, i.e. the third and fourth ventricle. Similar degrees of shrinkage in WM volume and increase of the ventricular system have been reported in studies of Alzheimer's disease during disease progression and in its prestage mild cognitive impairment. Based on these findings, a potential confound in GM and WM or CSF studies due to the subjects' hydration state cannot be excluded and should be appropriately addressed. These results underline the sensitivity of VBM and might also concern other voxel-based methods, such as Tract-Based Spatial Statistics (TBSS). TBSS was specifically designed for WM analyses and its sensitivity might be helpful for revealing the spatial relation of structural WM changes and related blood serum biomarkers. Two common brain related biomarkers are the glial protein S100B, a plasticity inducing neuro- and gliotrophin, and neuron-specific enolase (NSE), a marker for neuronal damage. However, the spatial specificity of these biomarkers for brain region has not been investigated in vivo until now. Therefore, we acquired two MRI parameters – T_1-weighted and DTI - sensitive to changes in GM and WM, and obtained serum S100B and NSE levels of 41 healthy subjects. Additionally, the gene expression of S100B on the whole brain level in a male cohort of three subjects from the Allen Brain Database was analyzed. Furthermore, a female post mortal brain was investigated using double immunofluorescence labeling with oligodendrocyte markers. It could be shown that S100B is specifically related to white matter structures, namely the corpus callosum, anterior forceps and superior longitudinal fasciculus in female subjects. This effect was observed in fractional anisotropy and radial diffusivity – the latest an indicator of myelin changes. Histological data confirmed a co-localization of S100B with oligodendrocyte markers in the human corpus callosum. S100B was most abundantly expressed in the corpus callosum according to the whole genome Allen Human Brain Atlas. In addition, NSE was related to gray matter structures, namely the amygdala. This effect was detected across sexes. The data demonstrates a very high S100B expression in white matter tracts, in particular in human corpus callosum. This was the first in vivo study validating the specificity of the glial marker S100B for the human brain, and supporting the assumption that radial diffusivity represents a myelin marker. The results open a new perspective for future studies investigating major neuropsychiatric disorders. All above mentioned studies are mainly dependent on the sensitivity and accuracy of soft- and hardware parameters. In particular, technical developments have improved acquisition accuracy in the field of MRI. Interestingly, very little is known about the confounding effects of variations due to hardware parameters and their possible impact on reliability and sensitivity of VBM. Recent studies have shown that different acquisition parameters may influence VBM results. Therefore age-related GM changes were investigated with VBM in 36 healthy volunteers grouped into 12 young, 12 middle-aged and 12 elderly subject. Six T_1-weighted datasets were acquired per subject with a 12-channel matrix coil, as well as a 32-channel array, MP-RAGE and MP2RAGE, and with isotropic resolutions of 0.8 and 1 mm. DARTEL-VBM was applied on all images and GM, WM and CSF segments were statistically analyzed.. Paired *t*-tests and statistical interaction tests revealed significant effects of acquisition parameters on the estimated gray-matter-density (GMD) in various cortical and subcortical brain regions. MP2RAGE seemed slightly less prone to false positive results when comparing data acquired with different RF coils and yielded superior segmentation of deep GM structures. With the 12-channel coil, MP-RAGE was superior in detecting age-related changes, especially in cortical structures. Most differences between both sequences became insignificant with the 32-channel coil, indicating that the MP2RAGE images benefited more from the improved signal-to-noise ratio and improved parallel-imaging reconstruction). A possible explanation might be an overestimation of the GM compartment on the MP-RAGE images. In view of substantial effects obtained for all parameters, careful standardization of the acquisition protocol is advocated. While the current investigation focused on aging effects, similar results are expected for other VBM studies, like on plasticity or neurodegenerative diseases.

This work has shown that voxel-based methods are sensitive to subtle structural brain changes, independent of imaging modality and scanning parameters. In particular, the studies investigated and discussed the analysis of T_1- and diffusion weighted images with VBM and TBSS in the context of dehydration, blood serum sensitive biomarkers and aging were discussed. The major goal of these studies was the investigation of the sensitivity of voxel-based methods. In conclusion, sensitivity and accuracy of voxel-based methods is already high, but it can be increased significantly, using optimal hard- and software parameters. It is of note, though, that these optimizations and the concomitant increase of detection sensitivity could also introduce additional confounding factors in the imaging data and interfere with the latter preprocessing and statistical computations. To avoid an interference e.g. originating from physiological parameters, a very careful selection and monitoring of biological parameters of each volunteer throughout the whole study is recommended. A potential impact of scanning parameters can be minimized by strict adherence to the imaging protocol for each study subject within a study. A general increase in detection sensitivity due to optimized parameters selection in hard- and/or can not be concluded by the above mentioned studies. Although the present work addressed some of those issues, the topic of optimal selection of parameters for morphometric studies is still very complex and controversial and has to be individually decided. Further investigations are needed to define more general scanning and preprocessing standards to increase detection sensitivity without the concomitant amplification of confounding factors.

References

Abdul-Kareem, I.A., Stancak, A., Parkes, L.M., Sluming, V., 2011. Increased gray matter volume of left pars opercularis in male orchestral musicians correlate positively with years of musical performance. J Magn Reson Imaging 33, 24-32.
Abdul-Khaliq, H., Schubert, S., Stoltenburg-Didinger, G., Troitzsch, D., Bottcher, W., Hubler, M., Meissler, M., Grosse-Siestrop, C., Alexi-Meskishvili, V., Hetzer, R., Lange, P.E., 2000. Protein S-100beta in brain and serum after deep hypothermic circulatory arrest in rabbits: relationship to perivascular astrocytic swelling. Clin Chem Lab Med 38, 1169-1172.
Acosta-Cabronero, J., Williams, G.B., Pereira, J.M., Pengas, G., Nestor, P.J., 2008. The impact of skull-stripping and radio-frequency bias correction on grey-matter segmentation for voxel-based morphometry. Neuroimage 39, 1654-1665.
Alzheimer`s Disease International, 2011. Alzheimer's Disease International World Alzheimer Report 2011 The benefits of early diagnosis and intervention. In: Prince, M., Bryce, R., Ferri, C. (Eds.).
Apostolova, L.G., Beyer, M., Green, A.E., Hwang, K.S., Morra, J.H., Chou, Y.Y., Avedissian, C., Aarsland, D., Janvin, C.C., Larsen, J.P., Cummings, J.L., Thompson, P.M., 2010. Hippocampal, caudate, and ventricular changes in Parkinson's disease with and without dementia. Mov Disord 25, 687-695.
Armstrong, L.E., Pumerantz, A.C., Fiala, K.A., Roti, M.W., Kavouras, S.A., Casa, D.J., Maresh, C.M., 2010. Human hydration indices: acute and longitudinal reference values. Int J Sport Nutr Exerc Metab 20, 145-153.
Ashburner, J., 2007. A fast diffeomorphic image registration algorithm. Neuroimage 38, 95-113.
Ashburner, J., Friston, K.J., 2000. Voxel-based morphometry--the methods. Neuroimage 11, 805-821.
Ashburner, J., Friston, K.J., 2005. Unified segmentation. Neuroimage 26, 839-851.
Barta, P.E., Dhingra, L., Royall, R., Schwartz, E., 1997. Improving stereological estimates for the volume of structures identified in three-dimensional arrays of spatial data. J Neurosci Methods 75, 111-118.
Basser, P.J., Mattiello, J., LeBihan, D., 1994. MR diffusion tensor spectroscopy and imaging. Biophys J 66, 259-267.
Basser, P.J., Pierpaoli, C., 1996. Microstructural and physiological features of tissues elucidated by quantitative-diffusion-tensor MRI. J Magn Reson B 111, 209-219.
Baudendistel, K.T., Heverhagen, J.T., Knopp, M.V., 2004. [Clinical MR at 3 Tesla: current status]. Radiologe 44, 11-18.
Bazarian, J.J., Zhong, J., Blyth, B., Zhu, T., Kavcic, V., Peterson, D., 2007. Diffusion tensor imaging detects clinically important axonal damage after mild traumatic brain injury: a pilot study. J Neurotrauma 24, 1447-1459.
Bendel, P., Koivisto, T., Aikia, M., Niskanen, E., Kononen, M., Hanninen, T., Vanninen, R., 2010. Atrophic enlargement of CSF volume after subarachnoid hemorrhage: correlation with neuropsychological outcome. AJNR Am J Neuroradiol 31, 370-376.

Bendfeldt, K., Kuster, P., Traud, S., Egger, H., Winklhofer, S., Mueller-Lenke, N., Naegelin, Y., Gass, A., Kappos, L., Matthews, P.M., Nichols, T.E., Radue, E.W., Borgwardt, S.J., 2009. Association of regional gray matter volume loss and progression of white matter lesions in multiple sclerosis - A longitudinal voxel-based morphometry study. Neuroimage 45, 60-67.

Berk, L., Rana, S., 2006. Hypovolemia and dehydration in the oncology patient. J Support Oncol 4, 447-454; discussion 455-447.

Bernstein, H.G., Steiner, J., Bogerts, B., 2009. Glial cells in schizophrenia: pathophysiological significance and possible consequences for therapy. Expert Rev Neurother 9, 1059-1071.

Brandner, F.A., 1933. A Test of the Significance of the Difference of the Correlation Coefficiencts in Normal Bivariate Samples. Biometrika 25, 102-109.

Brenneis, C., Seppi, K., Schocke, M.F., Muller, J., Luginger, E., Bosch, S., Loscher, W.N., Buchel, C., Poewe, W., Wenning, G.K., 2003. Voxel-based morphometry detects cortical atrophy in the Parkinson variant of multiple system atrophy. Mov Disord 18, 1132-1138.

Brex, P.A., Jenkins, R., Fox, N.C., Crum, W.R., O'Riordan, J.I., Plant, G.T., Miller, D.H., 2000. Detection of ventricular enlargement in patients at the earliest clinical stage of MS. Neurology 54, 1689-1691.

Bridge, H., Clare, S., 2006. High-resolution MRI: in vivo histology? Philos Trans R Soc Lond B Biol Sci 361, 137-146.

Burton, E.J., McKeith, I.G., Burn, D.J., Williams, E.D., O'Brien, J.T., 2004. Cerebral atrophy in Parkinson's disease with and without dementia: a comparison with Alzheimer's disease, dementia with Lewy bodies and controls. Brain 127, 791-800.

Busnello, J.V., Leke, R., Oses, J.P., Feier, G., Bruch, R., Quevedo, J., Kapczinski, F., Souza, D.O., Cruz Portela, L.V., 2006. Acute and chronic electroconvulsive shock in rats: effects on peripheral markers of neuronal injury and glial activity. Life Sci 78, 3013-3017.

Butterfield, D.A., Howard, B.J., LaFontaine, M.A., 2001. Brain oxidative stress in animal models of accelerated aging and the age-related neurodegenerative disorders, Alzheimer's disease and Huntington's disease. Curr Med Chem 8, 815-828.

Butterfield, D.A., Kanski, J., 2001. Brain protein oxidation in age-related neurodegenerative disorders that are associated with aggregated proteins. Mech Ageing Dev 122, 945-962.

Camicioli, R., Gee, M., Bouchard, T.P., Fisher, N.J., Hanstock, C.C., Emery, D.J., Martin, W.R., 2009. Voxel-based morphometry reveals extra-nigral atrophy patterns associated with dopamine refractory cognitive and motor impairment in parkinsonism. Parkinsonism Relat Disord 15, 187-195.

Cammermeyer, J., 1960. The Distribution of Oligodendrocytes in Cerebral Gray and White Matter of Several Mammals. American Journal of Anatomy 107, 107-114.

Casmiro, M., Maitan, S., De Pasquale, F., Cova, V., Scarpa, E., Vignatelli, L., Group, N.S.E.S., 2005. Cerebrospinal fluid and serum neuron-specific enolase concentrations in a normal population. Eur J Neurol 12, 369-374.

Chen, X.H., Sachdev, P.S., Wen, W., Anstey, K.J., 2007. Sex differences in regional gray matter in healthy individuals aged 44-48 years: A voxel-based morphometric study. Neuroimage 36, 691-699.

Colcombe, S.J., Erickson, K.I., Scalf, P.E., Kim, J.S., Prakash, R., McAuley, E., Elavsky, S., Marquez, D.X., Hu, L., Kramer, A.F., 2006. Aerobic exercise training increases brain volume in aging humans. J Gerontol A Biol Sci Med Sci 61, 1166-1170.

Counsell, S.J., Edwards, A.D., Chew, A.T., Anjari, M., Dyet, L.E., Srinivasan, L., Boardman, J.P., Allsop, J.M., Hajnal, J.V., Rutherford, M.A., Cowan, F.M., 2008. Specific relations between neurodevelopmental abilities and white matter microstructure in children born preterm. Brain 131, 3201-3208.

de Kruijk, J.R., Leffers, P., Menheere, P.P.C.A., Meerhoff, S., Twijnstra, A., 2001. S-100B and neuron-specific enolase in serum of mild traumatic brain injury patients - A comparison with healthy controls. Acta Neurologica Scandinavica 103, 175-179.

Deichmann, R., Good, C.D., Josephs, O., Ashburner, J., Turner, R., 2000. Optimization of 3-D MP-RAGE sequences for structural brain imaging. Neuroimage 12, 112-127.

Dickson, J.M., Weavers, H.M., Mitchell, N., Winter, E.M., Wilkinson, I.D., Van Beek, E.J., Wild, J.M., Griffiths, P.D., 2005. The effects of dehydration on brain volume -- preliminary results. Int J Sports Med 26, 481-485.

Dietrich, O., Raya, J.G., Reeder, S.B., Reiser, M.F., Schoenberg, S.O., 2007. Measurement of signal-to-noise ratios in MR images: influence of multichannel coils, parallel imaging, and reconstruction filters. J Magn Reson Imaging 26, 375-385.

Donato, R., 1999. Functional roles of S100 proteins, calcium-binding proteins of the EF-hand type. Biochim Biophys Acta 1450, 191-231.

Draganski, B., Ashburner, J., Hutton, C., Kherif, F., Frackowiak, R.S., Helms, G., Weiskopf, N., 2011. Regional specificity of MRI contrast parameter changes in normal ageing revealed by voxel-based quantification (VBQ). Neuroimage 55, 1423-1434.

Draganski, B., Gaser, C., Busch, V., Schuierer, G., Bogdahn, U., May, A., 2004. Neuroplasticity: changes in grey matter induced by training. Nature 427, 311-312.

Draganski, B., May, A., 2008. Training-induced structural changes in the adult human brain. Behav Brain Res 192, 137-142.

Duning, T., Kloska, S., Steinstrater, O., Kugel, H., Heindel, W., Knecht, S., 2005. Dehydration confounds the assessment of brain atrophy. Neurology 64, 548-550.

Feldmann, A., Illes, Z., Kosztolanyi, P., Illes, E., Mike, A., Kover, F., Balas, I., Kovacs, N., Nagy, F., 2008. Morphometric changes of gray matter in Parkinson's disease with depression: a voxel-based morphometry study. Mov Disord 23, 42-46.

Ferreira, L.K., Diniz, B.S., Forlenza, O.V., Busatto, G.F., Zanetti, M.V., 2011. Neurostructural predictors of Alzheimer's disease: a meta-analysis of VBM studies. Neurobiology of Aging 32, 1733-1741.

Fischl, B., Salat, D.H., Busa, E., Albert, M., Dieterich, M., Haselgrove, C., van der Kouwe, A., Killiany, R., Kennedy, D., Klaveness, S., Montillo, A., Makris, N., Rosen, B., Dale, A.M., 2002. Whole brain segmentation: automated labeling of neuroanatomical structures in the human brain. Neuron 33, 341-355.

Frahm, J., Haase, A., Matthaei, D., 1986. Rapid three-dimensional MR imaging using the FLASH technique. J Comput Assist Tomogr 10, 363-368.

Frisoni, G.B., Fox, N.C., Jack, C.R., Scheltens, P., Thompson, P.M., 2010a. The clinical use of structural MRI in Alzheimer disease. Nature Reviews Neurology 6, 67 - 77.

Frisoni, G.B., Fox, N.C., Jack, C.R., Scheltens, P., Thompson, P.M., 2010b. The clinical use of structural MRI in Alzheimer disease. Nature Reviews Neurology 6, 67-77.

Friston, K.J., Holmes, A.P., Worsley, K.J., Poline, J.-P., Frith, C.D., Frackowiak, R.S.J., 1994. Statistical parametric maps in functional imaging: A general linear approach. Hum. Brain Mapp 2, 189–210.

Gazzolo, D., Michetti, F., Bruschettini, M., Marchese, N., Lituania, M., Mangraviti, S., Pedrazzi, E., Bruschettini, P., 2003. Pediatric concentrations of S100B protein in blood: age- and sex-related changes. Clin Chem 49, 967-970.

Good, C.D., Johnsrude, I., Ashburner, J., Henson, R.N., Friston, K.J., Frackowiak, R.S., 2001a. Cerebral asymmetry and the effects of sex and handedness on brain structure: a voxel-based morphometric analysis of 465 normal adult human brains. Neuroimage 14, 685-700.

Good, C.D., Johnsrude, I.S., Ashburner, J., Henson, R.N., Friston, K.J., Frackowiak, R.S., 2001b. A voxel-based morphometric study of ageing in 465 normal adult human brains. Neuroimage 14, 21-36.

Griswold, M.A., Jakob, P.M., Heidemann, R.M., Nittka, M., Jellus, V., Wang, J., Kiefer, B., Haase, A., 2002. Generalized autocalibrating partially parallel acquisitions (GRAPPA). Magn Reson Med 47, 1202-1210.

Groussard, M., La Joie, R., Rauchs, G., Landeau, B., Chetelat, G., Viader, F., Desgranges, B., Eustache, F., Platel, H., 2010. When music and long-term memory interact: effects of musical expertise on functional and structural plasticity in the hippocampus. PLoS One 5.

Gullans, S.R., Verbalis, J.G., 1993. Control of brain volume during hyperosmolar and hypoosmolar conditions. Annu Rev Med 44, 289-301.

Guo, X., Wang, Z., Li, K., Li, Z., Qi, Z., Jin, Z., Yao, L., Chen, K., 2010. Voxel-based assessment of gray and white matter volumes in Alzheimer's disease. Neuroscience Letters 468, 146-150.

Haase, A., 1990. Snapshot FLASH MRI. Applications to T1, T2, and chemical-shift imaging. Magn Reson Med 13, 77-89.

Hagemann, G., Ugur, T., Schleussner, E., Mentzel, H.J., Fitzek, C., Witte, O.W., Gaser, C., 2011. Changes in brain size during the menstrual cycle. PLoS One 6, e14655.

Haglid, K.G., Yang, Q., Hamberger, A., Bergman, S., Widerberg, A., Danielsen, N., 1997. S-100beta stimulates neurite outgrowth in the rat sciatic nerve grafted with acellular muscle transplants. Brain Res 753, 196-201.

Hajnal, J.V., De Coene, B., Lewis, P.D., Baudouin, C.J., Cowan, F.M., Pennock, J.M., Young, I.R., Bydder, G.M., 1992. High signal regions in normal white matter shown by heavily T2-weighted CSF nulled IR sequences. J Comput Assist Tomogr 16, 506-513.

Hayasaka, S., Nichols, T.E., 2003. Validating cluster size inference: random field and permutation methods. Neuroimage 20, 2343-2356.

Hayasaka, S., Phan, K.L., Liberzon, I., Worsley, K.J., Nichols, T.E., 2004. Nonstationary cluster-size inference with random field and permutation methods. Neuroimage 22, 676-687.

Helms, G., Draganski, B., Frackowiak, R., Ashburner, J., Weiskopf, N., 2009. Improved segmentation of deep brain grey matter structures using magnetization transfer (MT) parameter maps. Neuroimage 47, 194-198.
Henkelman, R.M., 1985. Measurement of signal intensities in the presence of noise in MR images. Med Phys 12, 232-233.
Holtkamp, K., Buhren, K., Ponath, G., von Eiff, C., Herpertz-Dahlmann, B., Hebebrand, J., Rothermundt, M., 2008. Serum levels of S100B are decreased in chronic starvation and normalize with weight gain. J Neural Transm 115, 937-940.
Hutton, C., Draganski, B., Ashburner, J., Weiskopf, N., 2009. A comparison between voxel-based cortical thickness and voxel-based morphometry in normal aging. Neuroimage 48, 371-380.
Hyde, D.E., Duffy, F.H., Warfield, S.K., 2012. Anisotropic partial volume CSF modeling for EEG source localization. Neuroimage 62, 2161-2170.
Ingebrigtsen, T., Romner, B., 2003. Biochemical serum markers for brain damage: a short review with emphasis on clinical utility in mild head injury. Restor Neurol Neurosci 21, 171-176.
Jack, C.R., Jr., Bernstein, M.A., Fox, N.C., Thompson, P., Alexander, G., Harvey, D., Borowski, B., Britson, P.J., J, L.W., Ward, C., Dale, A.M., Felmlee, J.P., Gunter, J.L., Hill, D.L., Killiany, R., Schuff, N., Fox-Bosetti, S., Lin, C., Studholme, C., DeCarli, C.S., Krueger, G., Ward, H.A., Metzger, G.J., Scott, K.T., Mallozzi, R., Blezek, D., Levy, J., Debbins, J.P., Fleisher, A.S., Albert, M., Green, R., Bartzokis, G., Glover, G., Mugler, J., Weiner, M.W., 2008. The Alzheimer's Disease Neuroimaging Initiative (ADNI): MRI methods. J Magn Reson Imaging 27, 685-691.
Johansen-Berg, H., Della-Maggiore, V., Behrens, T.E., Smith, S.M., Paus, T., 2007. Integrity of white matter in the corpus callosum correlates with bimanual co-ordination skills. Neuroimage 36 Suppl 2, T16-21.
Jones, A.R., Overly, C.C., Sunkin, S.M., 2009. The Allen Brain Atlas: 5 years and beyond. Nat Rev Neurosci 10, 821-828.
Kaiser, E., Kuzmits, R., Pregant, P., Burghuber, O., Worofka, W., 1989. Clinical biochemistry of neuron specific enolase. Clin Chim Acta 183, 13-31.
Karas, G.B., Burton, E.J., Rombouts, S.A.R.B., van Schijndel, R.A., O'Brien, J.T., Scheltens, P., McKeith, I.G., Williams, D., Ballard, C., Barkhof, F., 2003. A comprehensive study of gray matter loss in patients with Alzheimer's disease using optimized voxel-based morphometry. Neuroimage 18, 895-907.
Karas, G.B., Scheltens, P., Rombouts, S.A., Visser, P.J., van Schijndel, R.A., Fox, N.C., Barkhof, F., 2004. Global and local gray matter loss in mild cognitive impairment and Alzheimer's disease. Neuroimage 23, 708-716.
Kassubek, J., Juengling, F.D., Kioschies, T., Henkel, K., Karitzky, J., Kramer, B., Ecker, D., Andrich, J., Saft, C., Kraus, P., Aschoff, A.J., Ludolph, A.C., Landwehrmeyer, G.B., 2004. Topography of cerebral atrophy in early Huntington's disease: a voxel based morphometric MRI study. J Neurol Neurosurg Psychiatry 75, 213-220.
Kaza, E., Klose, U., Lotze, M., 2011. Comparison of a 32-channel with a 12-channel head coil: are there relevant improvements for functional imaging? J Magn Reson Imaging 34, 173-183.

Kempton, M.J., Ettinger, U., Foster, R., Williams, S.C., Calvert, G.A., Hampshire, A., Zelaya, F.O., O'Gorman, R.L., McMorris, T., Owen, A.M., Smith, M.S., 2011. Dehydration affects brain structure and function in healthy adolescents. Human Brain Mapping 32, 71-79.

Kempton, M.J., Ettinger, U., Schmechtig, A., Winter, E.M., Smith, L., McMorris, T., Wilkinson, I.D., Williams, S.C., Smith, M.S., 2009. Effects of acute dehydration on brain morphology in healthy humans. Human Brain Mapping 30, 291-298.

Kinkingnehun, S., Sarazin, M., Lehericy, S., Guichart-Gomez, E., Hergueta, T., Dubois, B., 2008. VBM anticipates the rate of progression of Alzheimer disease: a 3-year longitudinal study. Neurology 70, 2201-2211.

Klauschen, F., Goldman, A., Barra, V., Meyer-Lindenberg, A., Lundervold, A., 2009. Evaluation of automated brain MR image segmentation and volumetry methods. Human Brain Mapping 30, 1310-1327.

Klein, A., Ghosh, S.S., Avants, B., Yeo, B.T., Fischl, B., Ardekani, B., Gee, J.C., Mann, J.J., Parsey, R.V., 2010. Evaluation of volume-based and surface-based brain image registration methods. Neuroimage 51, 214-220.

Kligman, D., Marshak, D.R., 1985. Purification and characterization of a neurite extension factor from bovine brain. Proc Natl Acad Sci U S A 82, 7136-7139.

Kochunov, P., Thompson, P.M., Lancaster, J.L., Bartzokis, G., Smith, S., Coyle, T., Royall, D.R., Laird, A., Fox, P.T., 2007. Relationship between white matter fractional anisotropy and other indices of cerebral health in normal aging: Tract-based spatial statistics study of aging. Neuroimage 35, 478-487.

Koo, M.S., Dickey, C.C., Park, H.J., Kubicki, M., Ji, N.Y., Bouix, S., Pohl, K.M., Levitt, J.J., Nakamura, M., Shenton, M.E., McCarley, R.W., 2006. Smaller neocortical gray matter and larger sulcal cerebrospinal fluid volumes in neuroleptic-naive women with schizotypal personality disorder. Arch Gen Psychiatry 63, 1090-1100.

Krueger, G., Granziera, C., Jack, C.R., Jr., Gunter, J.L., Littmann, A., Mortamet, B., Kannengiesser, S., Sorensen, A.G., Ward, C.P., Reyes, D.A., Britson, P.J., Fischer, H., Bernstein, M.A., 2012. Effects of MRI scan acceleration on brain volume measurement consistency. J Magn Reson Imaging.

Lambert, J.C., Ferreira, S., Gussekloo, J., Christiansen, L., Brysbaert, G., Slagboom, E., Cottel, D., Petit, T., Hauw, J.J., DeKosky, S.T., Richard, F., Berr, C., Lendon, C., Kamboh, M.I., Mann, D., Christensen, K., Westendorp, R., Amouyel, P., 2007. Evidence for the association of the S100beta gene with low cognitive performance and dementia in the elderly. Mol Psychiatry 12, 870-880.

Larsson, E.M., Stahlberg, F., 2005. [3 Tesla magnetic resonance imaging of the brain. Better morphological and functional images with higher magnetic field strength]. Lakartidningen 102, 460-463.

Lee, J.H., Garwood, M., Menon, R., Adriany, G., Andersen, P., Truwit, C.L., Ugurbil, K., 1995. High contrast and fast three-dimensional magnetic resonance imaging at high fields. Magn Reson Med 34, 308-312.

Liu, Y., Duan, Y., He, Y., Yu, C., Wang, J., Huang, J., Ye, J., Parizel, P.M., Li, K., Shu, N., 2012. Whole brain white matter changes revealed by multiple diffusion metrics in multiple sclerosis: A TBSS study. Eur J Radiol 81, 2826-2832.

Lüsebrink, F., Wollrab, A., Speck, O., 2013. Cortical thickness determination of the human brain using high resolution 3T and 7T MRI data. Neuroimage 70, 122-131.
Maguire, E.A., Gadian, D.G., Johnsrude, I.S., Good, C.D., Ashburner, J., Frackowiak, R.S., Frith, C.D., 2000. Navigation-related structural change in the hippocampi of taxi drivers. Proc Natl Acad Sci U S A 97, 4398-4403.
Maldjian, J.A., Laurienti, P.J., Kraft, R.A., Burdette, J.H., 2003. An automated method for neuroanatomic and cytoarchitectonic atlas-based interrogation of fMRI data sets. Neuroimage 19, 1233-1239.
Marangos, P.J., Schmechel, D.E., 1987. Neuron specific enolase, a clinically userful marker for neurons and neuroendocrine cells. Annu Rev Neurosci 10, 269-295.
Marchi, N., Cavaglia, M., Fazio, V., Bhudia, S., Hallene, K., Janigro, D., 2004. Peripheral markers of blood-brain barrier damage. Clin Chim Acta 342, 1-12.
Marques, J.P., Kober, T., Krueger, G., van der Zwaag, W., Van de Moortele, P.F., Gruetter, R., 2010. MP2RAGE, a self bias-field corrected sequence for improved segmentation and T1-mapping at high field. Neuroimage 49, 1271-1281.
Mazziotta, J., Toga, A., Evans, A., Fox, P., Lancaster, J., Zilles, K., Woods, R., Paus, T., Simpson, G., Pike, B., Holmes, C., Collins, L., Thompson, P., MacDonald, D., Iacoboni, M., Schormann, T., Amunts, K., Palomero-Gallagher, N., Geyer, S., Parsons, L., Narr, K., Kabani, N., Le Goualher, G., Boomsma, D., Cannon, T., Kawashima, R., Mazoyer, B., 2001. A probabilistic atlas and reference system for the human brain: International Consortium for Brain Mapping (ICBM). Philos Trans R Soc Lond B Biol Sci 356, 1293-1322.
Meyer-Lindenberg, A., Nicodemus, K.K., Egan, M.F., Callicott, J.H., Mattay, V., Weinberger, D.R., 2008. False positives in imaging genetics. Neuroimage 40, 655-661.
Meyer-Lindenberg, A., Straub, R.E., Lipska, B.K., Verchinski, B.A., Goldberg, T., Callicott, J.H., Egan, M.F., Huffaker, S.S., Mattay, V.S., Kolachana, B., Kleinman, J.E., Weinberger, D.R., 2007. Genetic evidence implicating DARPP-32 in human frontostriatal structure, function, and cognition. J Clin Invest 117, 672-682.
Mueller, K., Anwander, A., Moller, H.E., Horstmann, A., Lepsien, J., Busse, F., Mohammadi, S., Schroeter, M.L., Stumvoll, M., Villringer, A., Pleger, B., 2011. Sex-dependent influences of obesity on cerebral white matter investigated by diffusion-tensor imaging. PLoS One 6, e18544.
Mueller, S.G., Weiner, M.W., Thal, L.J., Petersen, R.C., Jack, C., Jagust, W., Trojanowski, J.Q., Toga, A.W., Beckett, L., 2005. The Alzheimer's disease neuroimaging initiative. Neuroimaging Clin N Am 15, 869-877, xi-xii.
Mugler, J.P., 3rd, Brookeman, J.R., 1990. Three-dimensional magnetization-prepared rapid gradient-echo imaging (3D MP RAGE). Magn Reson Med 15, 152-157.
Mugler, J.P., 3rd, Epstein, F.H., Brookeman, J.R., 1992. Shaping the signal response during the approach to steady state in three-dimensional magnetization-prepared rapid gradient-echo imaging using variable flip angles. Magn Reson Med 28, 165-185.
Nestor, S.M., Rupsingh, R., Borrie, M., Smith, M., Accomazzi, V., Wells, J.L., Fogarty, J., Bartha, R., Alzheimer's Disease Neuroimaging, I., 2008. Ventricular enlargement as a possible measure of Alzheimer's disease progression validated using the Alzheimer's disease neuroimaging initiative database. Brain 131, 2443-2454.

Nygaard, O., Langbakk, B., Romner, B., 1997. Age- and sex-related changes of S-100 protein concentrations in cerebrospinal fluid and serum in patients with no previous history of neurological disorder. Clin Chem 43, 541-543.
Nygaard, O., Langbakk, B., Romner, B., 1998. Neuron-specific enolase concentrations in serum and cerebrospinal fluid in patients with no previous history of neurological disorder. Scand J Clin Lab Invest 58, 183-186.
Onu, M., Roceanu, A., Sboto-Frankenstein, U., Bendic, R., Tarta, E., Preoteasa, F., Bajenaru, O., 2012. Diffusion abnormality maps in demyelinating disease: correlations with clinical scores. Eur J Radiol 81, e386-391.
Otto, M., Wiltfang, J., Schutz, E., Zerr, I., Otto, A., Pfahlberg, A., Gefeller, O., Uhr, M., Giese, A., Weber, T., Kretzschmar, H.A., Poser, S., 1998. Diagnosis of Creutzfeldt-Jakob disease by measurement of S100 protein in serum: prospective case-control study. BMJ 316, 577-582.
Pannacciulli, N., Del Parigi, A., Chen, K., Le, D.S., Reiman, E.M., Tataranni, P.A., 2006. Brain abnormalities in human obesity: a voxel-based morphometric study. Neuroimage 31, 1419-1425.
Pell, G.S., Briellmann, R.S., Pardoe, H., Abbott, D.F., Jackson, G.D., 2006. Investigation of sources of variance in the analysis of structural data with VBM: the potential for pooling images from different acquisition schemes and different scanners. Proc. ISMRM 14th Annual Meeting, Seattle, 1018.
Pereira, J.M., Nestor, P.J., Williams, G.B., 2008. Impact of inconsistent resolution on VBM studies. Neuroimage 40, 1711-1717.
Pezawas, L., Verchinski, B.A., Mattay, V.S., Callicott, J.H., Kolachana, B.S., Straub, R.E., Egan, M.F., Meyer-Lindenberg, A., Weinberger, D.R., 2004. The brain-derived neurotrophic factor val66met polymorphism and variation in human cortical morphology. J Neurosci 24, 10099-10102.
Poelmans, G., Buitelaar, J.K., Pauls, D.L., Franke, B., 2011. A theoretical molecular network for dyslexia: integrating available genetic findings. Mol Psychiatry 16, 365-382.
Portela, L.V.C., Tort, A.B.L., Schaf, D.V., Ribeiro, L., Nora, D.B., Walz, R., Rotta, L.N., Silva, C.T., Busnello, J.V., Kapczinski, F., Goncalves, C.A., Souza, D.O., 2002. The serum S100B concentration is age dependent. Clin Chem 48, 950-952.
Rainey, T., Lesko, M., Sacho, R., Lecky, F., Childs, C., 2009. Predicting outcome after severe traumatic brain injury using the serum S100B biomarker: results using a single (24h) time-point. Resuscitation 80, 341-345.
Ridgway, G.R., Henley, S.M., Rohrer, J.D., Scahill, R.I., Warren, J.D., Fox, N.C., 2008. Ten simple rules for reporting voxel-based morphometry studies. Neuroimage 40, 1429-1435.
Righini, N.C., Narring, F., Navarro, C., Perret-Catipovic, M., Ladame, F., Jeannin, A., Berchtold, A., Michaud, P.A., 2005. Antecedents, psychiatric characteristics and follow-up of adolescents hospitalized for suicide attempt of overwhelming suicidal ideation. Swiss Med Wkly 135, 440-447.
Rothermundt, M., Peters, M., Prehn, J.H., Arolt, V., 2003. S100B in brain damage and neurodegeneration. Microsc Res Tech 60, 614-632.

Rothermundt, M., Peters, M., Wiesmann, M., Hettich, M., Abel, S., Rudolf, S., Kirchner, H., Arolt, V., 2002. The neuroplasticity marker S100B in schizophrenia: Increased serum levels are associated with negative symptomatology. Schizophr Res 53, 152-153.
Rothermundt, M., Ponath, G., Arolt, V., 2004. S100B in schizophrenic psychosis. Int Rev Neurobiol 59, 445-470.
Sacher, J., Neumann, J., Funfstuck, T., Soliman, A., Villringer, A., Schroeter, M.L., 2011. Mapping the depressed brain: A meta-analysis of structural and functional alterations in major depressive disorder. J Affect Disord.
Saini, J., Bagepally, B.S., Sandhya, M., Pasha, S.A., Yadav, R., Pal, P.K., 2012. In vivo evaluation of white matter pathology in patients of progressive supranuclear palsy using TBSS. Neuroradiology 54, 771-780.
Salmon, D.P., Bondi, M.W., 2009. Neuropsychological assessment of dementia. Annu Rev Psychol 60, 257-282.
Schaf, D.V., Tort, A.B., Fricke, D., Schestatsky, P., Portela, L.V., Souza, D.O., Rieder, C.R., 2005. S100B and NSE serum levels in patients with Parkinson's disease. Parkinsonism Relat Disord 11, 39-43.
Schafer, B.W., Heizmann, C.W., 1996. The S100 family of EF-hand calcium-binding proteins: functions and pathology. Trends Biochem Sci 21, 134-140.
Schmechel, D., Marangos, P.J., Brightman, M., 1978. Neurone-specific enolase is a molecular marker for peripheral and central neuroendocrine cells. Nature 276, 834 - 836.
Schmierer, K., Wheeler-Kingshott, C.A., Tozer, D.J., Boulby, P.A., Parkes, H.G., Yousry, T.A., Scaravilli, F., Barker, G.J., Tofts, P.S., Miller, D.H., 2008. Quantitative magnetic resonance of postmortem multiple sclerosis brain before and after fixation. Magn Reson Med 59, 268-277.
Schmitt, F., Grosu, D., Mohr, C., Purdy, D., Salem, K., Scott, K.T., Stoeckel, B., 2004. [3 Tesla MRI: successful results with higher field strengths]. Radiologe 44, 31-47.
Schols, J.M., De Groot, C.P., van der Cammen, T.J., Olde Rikkert, M.G., 2009. Preventing and treating dehydration in the elderly during periods of illness and warm weather. J Nutr Health Aging 13, 150-157.
Schott, J.M., Price, S.L., Frost, C., Whitwell, J.L., Rossor, M.N., Fox, N.C., 2005. Measuring atrophy in Alzheimer disease: a serial MRI study over 6 and 12 months. Neurology 65, 119-124.
Schroeter, M.L., Abdul-Khaliq, H., Diefenbacher, A., Blasig, I.E., 2002. S100B is increased in mood disorders and may be reduced by antidepressive treatment. Neuroreport 13, 1675-1678.
Schroeter, M.L., Abdul-Khaliq, H., Fruhauf, S., Hohne, R., Schick, G., Diefenbacher, A., Blasig, I.E., 2003. Serum S100B is increased during early treatment with antipsychotics and in deficit schizophrenia. Schizophr Res 62, 231-236.
Schroeter, M.L., Abdul-Khaliq, H., Krebs, M., Diefenbacher, A., Blasig, I.E., 2008. Serum markers support disease-specific glial pathology in major depression. J Affect Disord 111, 271-280.
Schroeter, M.L., Abdul-Khaliq, H., Krebs, M., Dieferibacher, A., Blasig, I.E., 2009a. Neuron-specific enolase is unaltered whereas S100B is elevated in serum of patients with schizophrenia - Original research and meta-analysis. Psychiatry Research 167, 66-72.

Schroeter, M.L., Abdul-Khaliq, H., Sacher, J., Steiner, J., Blasig, I.E., Mueller, K., 2010. Mood disorders are glial disorders: evidence from in vivo studies. Cardiovasc Psychiatry Neurol 2010, 780645.
Schroeter, M.L., Stein, T., Maslowski, N., Neumann, J., 2009b. Neural correlates of Alzheimer's disease and mild cognitive impairment: a systematic and quantitative meta-analysis involving 1351 patients. Neuroimage 47, 1196-1206.
Schroeter, M.L., Steiner, J., 2009. Elevated serum levels of the glial marker protein S100B are not specific for schizophrenia or mood disorders. Mol Psychiatry 14, 235-237.
Schroeter, M.L., Steiner, J., Mueller, K., 2011. Glial pathology is modified by age in mood disorders--a systematic meta-analysis of serum S100B in vivo studies. J Affect Disord 134, 32-38.
Shimazaki, H., Shinomoto, S., 2007. A method for selecting the bin size of a time histogram. Neural Comput 19, 1503-1527.
Shuter, B., Yeh, I.B., Graham, S., Au, C., Wang, S.C., 2008. Reproducibility of brain tissue volumes in longitudinal studies: effects of changes in signal-to-noise ratio and scanner software. Neuroimage 41, 371-379.
Simard, M., Nedergaard, M., 2004. The neurobiology of glia in the context of water and ion homeostasis. Neuroscience 129, 877-896.
Smith, C.D., Chebrolu, H., Wekstein, D.R., Schmitt, F.A., Markesbery, W.R., 2007. Age and gender effects on human brain anatomy: A voxel-based morphometric study in healthy elderly. Neurobiology of Aging 28, 1075-1087.
Smith, S.M., Jenkinson, M., Johansen-Berg, H., Rueckert, D., Nichols, T.E., Mackay, C.E., Watkins, K.E., Ciccarelli, O., Cader, M.Z., Matthews, P.M., Behrens, T.E., 2006. Tract-based spatial statistics: voxelwise analysis of multi-subject diffusion data. Neuroimage 31, 1487-1505.
Smith, S.M., Nichols, T.E., 2009. Threshold-free cluster enhancement: addressing problems of smoothing, threshold dependence and localisation in cluster inference. Neuroimage 44, 83-98.
Smith, S.M., Zhang, Y., Jenkinson, M., Chen, J., Matthews, P.M., Federico, A., De Stefano, N., 2002. Accurate, robust, and automated longitudinal and cross-sectional brain change analysis. Neuroimage 17, 479-489.
Song, S.K., Sun, S.W., Ju, W.K., Lin, S.J., Cross, A.H., Neufeld, A.H., 2003. Diffusion tensor imaging detects and differentiates axon and myelin degeneration in mouse optic nerve after retinal ischemia. Neuroimage 20, 1714-1722.
Statistisches Bundesamt, 2012. Einwohnerzahl Deutschlands im Jahr 2011 erstmals seit 2002 wieder gestiegen. Statistisches Bundesamt Statistisches Bundesamt
Steiner, J., Bernstein, H.G., Bielau, H., Berndt, A., Brisch, R., Mawrin, C., Keilhoff, G., Bogerts, B., 2007. Evidence for a wide extra-astrocytic distribution of S100B in human brain. BMC Neurosci 8, 2.
Steiner, J., Bogerts, B., Schroeter, M.L., Bernstein, H.G., 2011. S100B protein in neurodegenerative disorders. Clin Chem Lab Med 49, 409-424.
Steiner, J., Schiltz, K., Walter, M., Wunderlich, M.T., Keilhoff, G., Brisch, R., Bielau, H., Bernstein, H.G., Bogerts, B., Schroeter, M.L., Westphal, S., 2010a. S100B serum levels are closely correlated with body mass index: an important caveat in neuropsychiatric research. Psychoneuroendocrinology 35, 321-324.

Steiner, J., Schroeter, M.L., Schiltz, K., Bernstein, H.G., Muller, U.J., Richter-Landsberg, C., Muller, W.E., Walter, M., Gos, T., Bogerts, B., Keilhoff, G., 2010b. Haloperidol and clozapine decrease S100B release from glial cells. Neuroscience 167, 1025-1031.
Steiner, J., Walter, M., Guest, P., Myint, A.M., Schiltz, K., Panteli, B., Brauner, M., Bernstein, H.G., Gos, T., Herberth, M., Schroeter, M.L., Schwarz, M.J., Westphal, S., Bahn, S., Bogerts, B., 2010c. Elevated S100B levels in schizophrenia are associated with insulin resistance. Mol Psychiatry 15, 3-4.
Stonnington, C.M., Tan, G., Kloppel, S., Chu, C., Draganski, B., Jack, C.R., Jr., Chen, K., Ashburner, J., Frackowiak, R.S., 2008. Interpreting scan data acquired from multiple scanners: a study with Alzheimer's disease. Neuroimage 39, 1180-1185.
Streitbürger, D.P., Möller, H.E., Tittgemeyer, M., Hund-Georgiadis, M., Schroeter, M.L., Mueller, K., 2012. Investigating structural brain changes of dehydration using voxel-based morphometry. PLoS One 7, e44195.
Stroick, M., Fatar, M., Ragoschke-Schumm, A., Fassbender, K., Bertsch, T., Hennerici, M.G., 2006. Protein S-100B - A prognostic marker for cerebral damage. Curr Med Chem 13, 3053-3060.
Sütterlin, S., Hoßmann, I., Klingholz, R., 2011. Demenz-Report - Wie sich die Regionen in Deutschland, Österreich und der Schweiz auf die Alteurng der Gesellschaft vorbereiten können. Berlin-Institut für Bevölkerung und Entwicklung.
Tanenbaum, L.N., 2006. Clinical 3T MR imaging: mastering the challenges. Magn Reson Imaging Clin N Am 14, 1-15.
Tardif, C.L., Collins, D.L., Pike, G.B., 2009. Sensitivity of voxel-based morphometry analysis to choice of imaging protocol at 3 T. Neuroimage 44, 827-838.
Tardif, C.L., Collins, D.L., Pike, G.B., 2010. Regional impact of field strength on voxel-based morphometry results. Human Brain Mapping 31, 943-957.
Taubert, M., Draganski, B., Anwander, A., Muller, K., Horstmann, A., Villringer, A., Ragert, P., 2010. Dynamic properties of human brain structure: learning-related changes in cortical areas and associated fiber connections. J Neurosci 30, 11670-11677.
Tessitore, A., Amboni, M., Cirillo, G., Corbo, D., Picillo, M., Russo, A., Vitale, C., Santangelo, G., Erro, R., Cirillo, M., Esposito, F., Barone, P., Tedeschi, G., 2012. Regional Gray Matter Atrophy in Patients with Parkinson Disease and Freezing of Gait. AJNR Am J Neuroradiol.
Turner, B., Ramli, N., Blumhardt, L.D., Jaspan, T., 2001. Ventricular enlargement in multiple sclerosis: a comparison of three-dimensional and linear MRI estimates. Neuroradiology 43, 608-614.
van Engelen, B.G., Lamers, K.J., Gabreels, F.J., Wevers, R.A., van Geel, W.J., Borm, G.F., 1992. Age-related changes of neuron-specific enolase, S-100 protein, and myelin basic protein concentrations in cerebrospinal fluid. Clin Chem 38, 813-816.
Wakana, S., Caprihan, A., Panzenboeck, M.M., Fallon, J.H., Perry, M., Gollub, R.L., Hua, K.G., Zhang, J.Y., Jiang, H.Y., Dubey, P., Blitz, A., van Zijl, P., Mori, S., 2007. Reproducibility of quantitative tractography methods applied to cerebral white matter. Neuroimage 36, 630-644.
Whitford, T.J., Savadjiev, P., Kubicki, M., O'Donnell, L.J., Terry, D.P., Bouix, S., Westin, C.F., Schneiderman, J.S., Bobrow, L., Rausch, A.C., Niznikiewicz, M., Nestor, P.G., Pantelis, C., Wood, S.J., McCarley, R.W., Shenton, M.E., 2011. Fiber geometry in the

corpus callosum in schizophrenia: evidence for transcallosal misconnection. Schizophr Res 132, 69-74.
Wiggins, G.C., Triantafyllou, C., Potthast, A., Reykowski, A., Nittka, M., Wald, L.L., 2006. 32-channel 3 Tesla receive-only phased-array head coil with soccer-ball element geometry. Magn Reson Med 56, 216-223.
Winninghammajor, F., Staecker, J.L., Barger, S.W., Coats, S., Vaneldik, L.J., 1989. Neurite extension and neuronal survival activities of recombinant S100-Beta proteins that differ in the content and position of cysteine residues. Journal of Cell Biology 109, 3063-3071.
World Health Organization, 2012. Dementia - A Public Health Priority. World Health Organisation, United Kingdom.
Worsley, K.J., Andermann, M., Koulis, T., MacDonald, D., Evans, A.C., 1999. Detecting changes in nonisotropic images. Human Brain Mapping 8, 98-101.
Worsley, K.J., Taylor, J.E., Carbonell, F., Chung, M.K., Duerden, E., Bernhardt, B., Lyttelton, O., Boucher, M., Evans, A.C., 2009. SurfStat: A Matlab toolbox for the statistical analysis of univariate and multivariate surface and volumetric data using linear mixed effects models and random field theory. OHBM poster.
Wright, I.C., Rabe-Hesketh, S., Woodruff, P.W., David, A.S., Murray, R.M., Bullmore, E.T., 2000. Meta-analysis of regional brain volumes in schizophrenia. Am J Psychiatry 157, 16-25.
Yeh, P.H., Simpson, K., Durazzo, T.C., Gazdzinski, S., Meyerhoff, D.J., 2009. Tract-Based Spatial Statistics (TBSS) of diffusion tensor imaging data in alcohol dependence: abnormalities of the motivational neurocircuitry. Psychiatry Res 173, 22-30.
Zimmer, D.B., Cornwall, E.H., Landar, A., Song, W., 1995. The S100 protein family: history, function, and expression. Brain Res Bull 37, 417-429.

Erklärung über die eigenständige Abfassung der Arbeit

Hiermit erkläre ich, dass ich die vorliegende Arbeit selbständig und ohne unzulässige Hilfe oder Benutzung anderer als der angegebenen Hilfsmittel angefertigt habe. Ich versichere, dass Dritte von mir weder unmittelbar noch mittelbar geldwerte Leistungen für Arbeiten erhalten haben, die im Zusammenhang mit dem Inhalt der vorgelegten Dissertation stehen, und dass die vorgelegte Arbeit weder im Inland noch im Ausland in gleicher oder ähnlicher Form einer anderen Prüfungsbehörde zum Zweck einer Promotion oder eines anderen Prüfungsverfahrens vorgelegt wurde. Alles aus anderen Quellen und von anderen Personen übernommene Material, das in der Arbeit verwendet wurde oder auf das direkt Bezug genommen wird, wurde als solches kenntlich gemacht. Insbesondere wurden alle Personen genannt, die direkt an der Entstehung der vorliegenden Arbeit beteiligt waren.

12. April 2013

Datum Unterschrift

Lebenslauf

Vorname Name	Daniel-Paolo Streitbürger
Anschrift	Brandvorwerkstraße 53 04275 Leipzig
E-Mail Adresse	paolo@cbs.mpg.de
Staatsangehörigkeit	Deutsch
Geburtsdatum	17.05.1985
Geburtsort	Braunschweig

Wissenschaftlicher Werdegang

seit April 2010	Promotionsstudent am Max-Planck-Institut für Kognitions- und Neurowissenschaften, Leipzig „Investigating Brain Structure Using Voxel-Based Methods with Magnetic Resonance Imaging“
Jan. 2009 – Feb. 2010	Wissenschaftlicher Mitarbeiter am Innovation Center Computer Assisted Surgery (ICCAS), Leipzig

Schule und Studium

Okt. 2004 – Sep. 2008	Diplom Studium der Informatik an der Technischen Universität Braunschweig Diplomarbeit am Institut für medizinische Informatik: „Typisierung, Identifikation und qualitative Analyse von Aufstehbewegungen durch Beschleunigungsdaten“
Sommer 2004	Schulabschluss Abitur
2001 – 2004	Lessinggymnasium, Braunschweig

Wissenschaftliche Veröffentlichungen

Publikationen

Streitbürger D-P, Möller HE, Tittgemeyer M, Hund-Georgiadis M, Schroeter ML, et al. (2012) Investigating Structural Brain Changes of Dehydration Using Voxel-Based Morphometry. PLoS ONE 7(8): e44195. doi:10.1371/journal.pone.0044195

Streitbürger D-P, Arelin K, Kratzsch J, Thiery J, Steiner J, et al. (2012) Validating Serum S100B and Neuron-Specific Enolase as Biomarkers for the Human Brain – A Combined Serum, Gene Expression and MRI Study. PLoS ONE 7(8): e43284. doi:10.1371/journal.pone.0043284

Streitbürger, D-P, André Pampel, Jöran Lepsien, Matthias L. Schroeter, Karsten Mueller, Harald E. Möller, Impact of Image Acquisition on Voxel-Based Morphometry Investigations of Age-Related Structural Brain Changes, (submitted)

Quinque EM, Arélin K, Dukart J, Roggenhofer E, **Streitbuerger DP**, Villringer A, Frisch S, Mueller K, Schroeter ML. Identifying the neural correlates of executive functions in early cerebral microangiopathy: a combined VBM and DTI study., J Cereb Blood Flow Metab. 2012 Oct; 32(10):1869-78. doi: 10.1038/jcbfm.2012.96

Vorträge

Impact of Imaging Sequence and RF Coil on Voxel Based Morphometry: Investigation of Age-Related Structural Brain Changes, ESMRMB 2012, 132: p. 103-104

Extension of the human ventricular system after hyperhydration followed by long-term dehydration, ESMRMB 2011, 339: p. 244

Ein modulares Assistenzsystem zur intraoperativen Lokalisation des Sulcus Centralis bei Tumorresektionen nahe des Motorkortex. GI Jahrestagung 2009: 1070-1084

Poster

Validating S100B as biomarker for the human brain – A combined serum, gene expression and MRI study, Organization for Human Brain Mapping 2012, 174

Intraoperative Mapping of the Central Sulcus using Surgical Navigation and Somatosensory Evoked Potentials, 6th Annual World Congress for Brain Mapping and Image Guided Therapy, 2009

Impact of Image Acquisition on Voxel-Based Morphometry for Investigating Age-Related Structural Brain Changes, International Society for Magnetic Resonance in Medicine, 2013

Danksagung

Mein Dank gilt meinen Betreuern Prof. Dr. Dr. Matthias Schroeter und PD. Dr. Karsten Müller, die mir die Möglichkeit gaben diese Arbeit erfolgreich durchzuführen und mich mit vielseitigen Anregungen und fachgerechten Ratschlägen unterstützten. Weiter möchte ich auch Prof. Dr. Harald Möller für seine intensive und tatkräftige Unterstützung bei der Anfertigung und Korrektur meiner Manuskripte danken.

Ebenfalls möchte ich meiner Familie, Freunden und Kollegen und im speziellen Štefan Holiga danken, dass sie mich im Wissenschaftlichen und nicht Wissenschaftlichen während der gesamten Zeit unterstützt haben.